Rudolf Gati

Interaction of Ultracold Atoms in Periodical Potentials

Diploma Thesis

Jan 2004

University of Stuttgart
5th Institute of Physics
Chair of Professor Dr. Tilman Pfau

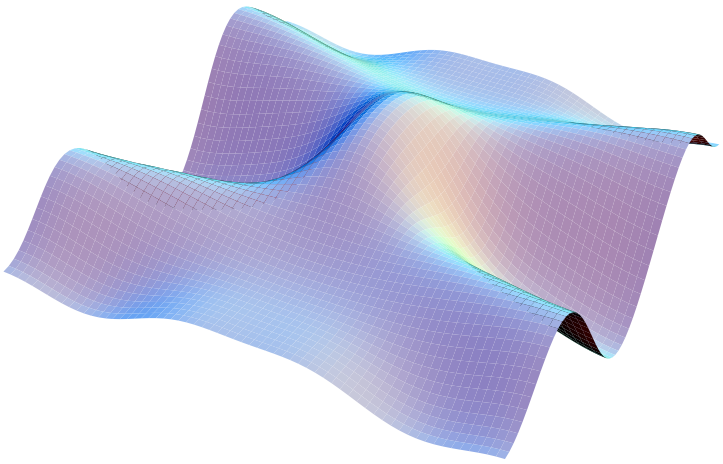

Light Induced Dipole-Dipole Interaction Potential

Rudolf Gati · Interaction of Ultracold Atoms in Periodical Potentials · Diploma thesis · 5th Institute of Physics · Chair of Professor Tilman Pfau · University of Stuttgart · Second edition · Jan 2004

Rudolf Gati · Wechselwirkung ultrakalter Atome in periodischen Potentialen · Diplomarbeit · Fünftes Physikalisches Institut · Lehrstuhl Prof. Dr. Tilman Pfau · Universität Stuttgart · Zweitabgabe · Jan 2004

Contents

1. Introduction

During the last century scientists attempt to reach lower and lower temperatures to generate new physical states ant to prepare degenerate quantum systems. With each step towards absolute zero new and rich physical phenomena emerged. The most recent milestone during this process was the experimental realization of Bose-Einstein condensation in dilute gases. The Bose-Einstein condensation is based on the wave nature and the indistinguishability of particles with integer spin. It is initiated if the spatial extension of the atomic wave packet, given by the de-Broglie-wavelength $\Lambda_{\mathrm{B}} = h/\sqrt{2\pi m k_B T}$, becomes comparable to the interatomic separation ($\sim n^{-3}$). At a critical phase space density of $D = \frac{n \cdot \Lambda_{\mathrm{B}}^3}{\hbar^3} \approx 2.612\hbar^{-3}$ the atomic wave packets overlap and the ground state of the system becomes macroscopically populated. For dilute alkali gases extremely low temperatures on the order of a few 100nK are necessary to reach this critical phase space density. Therefore, it is not surprising that the lowest temperatures ever observed (below 500pK [1]) were in such systems.

For the first time Bose-Einstein condensation was observed in 1995, 70 years after its proposal by Albert Einstein [2] based on a letter of Satyendra N. Bose [3] about the quantum statistics of particles with integer spin. Eric A. Cornell, Carl E. Wiemann [4] and Wolfgang Ketterle [5] were awarded with the *Nobel Price* in 2001 [6] for the generation and experimental examination of Bose-Einstein condensates (BEC).

The main experimental features of BECs are their low temperature, their global phase-coherence and nonlinearities due to interatomic interactions. These advantageous properties are limited by different quantities: the temperature by the interaction energy and the ground state energy of the trap potential, the coherence length by the confinement and the mean-field energy [7] and the interactions by heating and loss mechanism. Due to its properties completely new applications of BECs are imaginable. At the extremely low temperatures measurements with high momentum resolution may be achieved, the phase-coherence can be used for interference experiments and the most versatile effects in BECs result from interatomic interactions. Elementary properties as the s-wave scattering length or the physical dimensions can be manipulated.

The first experiments with BECs were performed to investigate the interplay of quantum statistic and the mean-field energy. Elementary excitations as phonons and vortices were studied [8]. The next milestones were the realization of atom-lasers [9, 10] and the phase coherent amplification of matter

waves [11]. A recent development was the preparation of BECs in periodic potentials, which opened up the possibility to investigate new phenomena at the border between different areas of physics. Combining a BEC with an optical lattice for example provides an opportunity for exploring a quantum system analogous to electrons in solid state crystals but with unprecedented control over the lattice and the particles. The transition from a superfluid to a Mott-insulator state could be obtained by the variation of the depth of the optical potential [12].

At the moment the tendency is to find new applications for BECs like precision-measurements as Heisenberg-limited interferometry [13] and to study interatomic interactions. The ability of controlling these interactions enables the experimentalists to tune the properties of the condensate and to manufacture quantum states. A promising application would be the realization of a quantum computer [14].

The isotropic short range s-wave interaction was already the subject of early studies. Its strength can be varied over a wide range by Feshbach-resonances [15, 16] and was used for example to create a molecular condensate of fermionic ^{40}K [17]. Recently the interest in static magnetic and induced electric dipole-dipole interactions in degenerate quantum gases rouse. Several proposals about new applications [18–26] and discussions on new phenomena like dipolar relaxations [27] were published. The main features of the dipole-dipole interaction are its anisotropy and its long interaction range. Furthermore, the light induced dipole-dipole interaction has another two advantages: the range of interaction is increased due to retardation effects and the dipole moment can be manipulated by changing the polarization and the intensity of the irradiated light field. Therefore, it is a magnificent tool to control the interatomic interaction. The induced interaction was successfully demonstrated by observing a series of bound states of two 1.43-μm-diam plastic spheres in water [28]. However, so far it was not possible to measure the mechanical effects caused by the retarded interaction on atomic systems, only indirect experimental evidence was found by photoassociation-spectroscopy on ultra-cold atoms [29].

The subject of this thesis is the investigation of the mechanical effects caused by the light induced dipole-dipole interaction. Numerical calculations of the induced potentials within dense BECs were performed for a wide range of different initial conditions and configurations to investigate for example the necessity of optical lattices or the behaviour of the induced potential on the properties of the incident light field. The aim of the calculations was not only to gain a deeper understanding of the interaction of light and atoms and the interatomic interactions but also to find an experimental access to probe the mechanical effects caused by the induced potentials and to set boundary conditions for the experimental parameters. The computations confirmed that with our experimental setup we can reach a regime where the light induced dipole-dipole interaction significantly changes the momentum distribution of the atoms and measurable effects can be observed in time-of-flight measurements.

This thesis is structured in the following way. In chapter 2 the theoretical basics of the light induced dipole-dipole interaction are introduced. The discussion on two-level atoms and the optical Bloch equations necessary for the calculation of the magnitude of the dipole moments and the spatial dependance of the dipole-dipole interaction is followed by the theoretical presentation of Bose-Einstein condensation in the noninteracting and the interacting case. The chapter is completed by a review on optical traps.

Chapter 3 contains a short review of the experimental setup and its different components like the vacuum system and the laser system. The latest progress as the construction of a 1D-optical lattice and the current status of the experiment are discussed at the end of this chapter.

The main subject of chapter 4 is the presentation of the numerical calculations and the considerations on the effects which were taken into account. Calculations for two different sets of typical parameters are shown and the problems encountered during the calculations are discussed. The two cases are the induction of dipole-dipole interaction with resonant and far-detuned light.

Chapter 5 is devoted to the presentation of the results of the numerical calculations. The induced potentials and the momentum distributions and their correlation to different experimental parameters are discussed. An estimation on the expected error is given and the first experimental approach pointed out.

The thesis is closed by chapter 6. The conclusions are presented and an outlook on possible measurements and applications of the light induced dipole-dipole interaction is given.

2. Theoretical Basics

In this chapter we are going to discuss the general theoretical basics needed for the treatment of the mechanical effects caused by the light induced dipole-dipole interaction. We will first introduce the theoretical formalism of the interaction of a single atom and an electromagnetic field. Then we are going to concentrate on static and dynamic dipoles and their interaction. At the end of the chapter a review of Bose-Einstein condensation will be given and the theoretical treatment of optical lattices discussed.

2.1 Interaction of Light and Matter

The internal degrees of freedom of an atom can be described in terms of different energy levels and several possible transitions between them. Transitions can be induced by the interaction of the atom and a coherent light beam. The detuning:

$$\delta_{\mathrm{L}} = \omega_{\mathrm{L}} - \omega_0 \ , \tag{2.1}$$

is the difference between the frequency of the monochromatic light field ω_{L} and one of the transition frequencies ω_0. If this quantity for a transition is small compared to the detuning with respect to all other allowed transitions, the atom may be treated as a two-level system. The two levels are called ground state $|g\rangle$ and excited state $|e\rangle$, and are separated by the energy $\hbar\omega_0$.

2.1.1 Optical Bloch Equations

A quantum mechanical description of the interaction of a single *two-level atom* with a monochromatic coherent light field is given by the optical Bloch equations. A derivation of the Bloch equations and a discussion can be found [30, 31].

The full Hamiltonian for the system is:

$$\hat{H} = \hat{H}_{\mathrm{atom}} + \hat{H}_{\mathrm{rad}} + \hat{H}_{\mathrm{int}} \ , \tag{2.2}$$

where $\hat{H}_{\mathrm{atom}}$ is the Hamiltonian of the atomic system, $\hat{H}_{\mathrm{rad}}$ is the Hamiltonian of the radiation (light) field and $\hat{H}_{\mathrm{int}}$ is the interaction Hamiltonian which takes the coupling of the radiation field and the atom into account. For the derivation of the optical Bloch equations using the *Raman-Nath approximation*, the kinetic energy of the atoms is neglected and the light field is treated classically.

If the wavelength of the monochromatic light field is much larger than the variance of the density distribution of the electron, the interaction Hamiltonian can be reduced. In the reduced interaction Hamiltonian the atom interacts with the light field only due to its electric dipole moment $\vec{d}$:

$$\hat{H}_{\text{int}} = -\hat{d} \cdot \vec{E} \,, \tag{2.3}$$

where $\vec{E}$ is the electric field $\vec{E} = E_0 \, \vec{e}_p \cdot \cos(\omega_0 t)$, with E_0 being the amplitude and $\vec{e}_p$ the unit vector in the direction of the polarization.

Having applied this approximation, the density matrix elements can be calculated by using the Hamilton equation:

$$i\hbar \frac{d}{dt}\hat{\rho} = [\hat{H}, \hat{\rho}] \quad \text{with} \quad \hat{\rho} = \begin{pmatrix} |g\rangle\langle g| & |g\rangle\langle e| \\ |e\rangle\langle g| & |e\rangle\langle e| \end{pmatrix} \,, \quad \langle \hat{O} \rangle = Tr[\hat{\rho}\hat{O}] \,, \tag{2.4}$$

where $\hat{\rho}$ is the density matrix and $\langle \hat{O} \rangle$ is the expectation value of operator $\hat{O}$.

Because a two-level system is formally equivalent to a fictitious spin $\frac{1}{2}$, the eigenstates may be expressed in terms of spin-vectors:

$$|g\rangle = \begin{pmatrix} 0 \\ 1 \end{pmatrix} \quad \text{and} \quad |e\rangle = \begin{pmatrix} 1 \\ 0 \end{pmatrix} \,, \tag{2.5}$$

and the Hamiltonian of the atomic system and the interaction Hamiltonian in terms of the Pauli spin matrices:

$$\sigma_x = \begin{pmatrix} 0 & 1 \\ 1 & 0 \end{pmatrix} \quad \sigma_y = \begin{pmatrix} 0 & -i \\ i & 0 \end{pmatrix} \quad \sigma_z = \begin{pmatrix} 1 & 0 \\ 0 & -1 \end{pmatrix} \,. \tag{2.6}$$

By calculating the expectation values of the density matrix elements, applying the rotating wave approximation and using the Bloch-vector (u, v, w) the optical Bloch equations can be derived. The components of the Bloch vector are given by:

$$u = \frac{1}{2} < \hat{\rho}_{ge} e^{i\omega_{\text{L}} t} + \hat{\rho}_{eg} e^{-i\omega_{\text{L}} t} > \tag{2.7}$$

$$v = \frac{1}{2i} < \hat{\rho}_{ge} e^{i\omega_{\text{L}} t} - \hat{\rho}_{eg} e^{-i\omega_{\text{L}} t} > \tag{2.8}$$

$$w = \frac{1}{2} < \hat{\rho}_{ee} - \hat{\rho}_{gg} > \,, \tag{2.9}$$

where $\hat{\rho}_{ab} = |a\rangle\langle b|$. By adding damping terms[1] due to spontaneous emission the optical Bloch equations can be written as:

$$\dot{u} = \delta_{\text{L}} v - u\Gamma/2 \tag{2.10}$$

$$\dot{v} = -\delta_{\text{L}} u - v\Gamma/2 - w\Omega \tag{2.11}$$

$$\dot{w} = \Omega v - w\Gamma - \Gamma/2 \,, \tag{2.12}$$

[1] The damping can be derived in terms of a dressed atom approach [30, 32]

where Γ is the natural linewidth of the transition $|g\rangle \leftrightarrow |e\rangle$, δ_{L} is the laser detuning (equation 2.1) and Ω is the so called *Rabi frequency*, which corresponds to the strength of the coupling:

$$\Omega = -\frac{d_{ge} \cdot E_0}{\hbar} \,, \tag{2.13}$$

with d_{ge} the dipole matrix element. w represents half the difference between the populations of the ground and the excited state, and u and v are, respectively, proportional to the components of the dipole moment in phase and in quadrature with the incident beam.

The optical Bloch equations are similar to the equations describing the evolution of a magnetic spin in a homogenous time-dependent magnetic field[2]. Their solution is a damped precession of the Bloch-vector. This damping occurs due to spontaneous emissions, which destroys the phase coherence of the precession. Without damping, the atom would be excited and deexcited coherently.

2.1.2 Steady State

For times longer than the inverse damping rate, the Bloch vector approaches a final position and the system tends towards a *steady state*. The Bloch vector in steady state is given by $(u_{\mathrm{st}}, v_{\mathrm{st}}, w_{\mathrm{st}})$ with

$$u_{\mathrm{st}} = \frac{\delta_{\mathrm{L}}}{\Omega}\frac{s}{s+1} \tag{2.14}$$

$$v_{\mathrm{st}} = \frac{\Gamma}{2\Omega}\frac{s}{s+1} \tag{2.15}$$

$$w_{\mathrm{st}} + \frac{1}{2} = \sigma_{\mathrm{st}} = \frac{1}{2}\frac{s}{s+1} \,, \tag{2.16}$$

where σ_{st} is the population of the upper state and s is the so called saturation parameter:

$$s = \frac{\Omega^2/2}{\delta_{\mathrm{L}}^2 + \Gamma^2/4} \,. \tag{2.17}$$

The rate of spontaneously emitted photons in steady state is proportional to the probability of finding the atom in the excited state σ_{st} and to the rate of decay of the excited state:

$$\Gamma_{\mathrm{sp}} = \frac{\Gamma}{2}\frac{s}{s+1} \,. \tag{2.18}$$

The damping of the Bloch vector due to spontaneous emissions is exponential, the steady state will be reached on the scale of the lifetime of the excited state $\tau = 1/\Gamma$. A more detailed discussion of the timescale will be presented in section 4.1.2 for ^{87}Rb.

[2] There is no damping in the case of a single magnetic spin.

2.1.3 Experimental Parameters

To compare the calculated quantities with the experimental results the dipole matrix element d_{ge}, the Rabi frequency Ω and the saturation parameter s have to be expressed in terms of the frequency ω_0 and the natural linewidth Γ of the transition $|g\rangle \leftrightarrow |e\rangle$ and the detuning δ_{L} and the intensity I_0 of the incident light beam. ω_0 and Γ are constants and are listed in section 3.1. δ_{L} and I_0 are the parameters which can be varied in the experimental setup.

The dipole matrix element can be expressed in terms of the natural linewidth as derived in [33]:

$$d_{ge} = \sqrt{\frac{3\varepsilon_0 h c^3}{2\omega_0^3}\,\Gamma} \quad . \tag{2.19}$$

The Rabi frequency (equation 2.13) may be rewritten in terms of the incident intensity as:

$$\Omega = \Gamma\sqrt{\frac{I_0}{2I_{\mathrm{sat}}}}\,, \tag{2.20}$$

where we have used that:

$$E_0 = \sqrt{\frac{2I_0}{\varepsilon_0 c}}\,, \tag{2.21}$$

and I_{sat} is the so called *saturation intensity* given by:

$$I_{\mathrm{sat}} = \frac{\hbar\Gamma\omega_0^3}{12\pi c^2}\,. \tag{2.22}$$

The saturation parameter s is:

$$s = \frac{I_0}{I_{\mathrm{sat}}}\left(\frac{1}{1+4\frac{\delta_{\mathrm{L}}^2}{\Gamma^2}}\right) \quad . \tag{2.23}$$

2.1.4 Dipole Moment

A dipole consists of two equivalent charges q of different sign separated by $\vec{l}$. The dipole moment is defined as:

$$\vec{d} = q \cdot \vec{l}\,. \tag{2.24}$$

For low light intensities, the classical picture of the driven harmonic oscillator may be considered to calculate the dipole moment. In the center-of-mass system, the atom can be described as an electron bound to the nucleus by a harmonic potential with the resonance frequency equal to the transition frequency ω_0. The driving force is the electric field of the electromagnetic wave and the damping is due to spontaneously emitted photons. The deflection of the electron multiplied by the charge is the corresponding dipole moment.

In the quantum mechanical calculation, which is also valid for high intensities, the optical Bloch equations have to be used in order to find the expectation value of the dipole moment operator.

The dipole moment operator is defined as $\hat{d} = q \cdot \hat{l}$, where $\hat{l}$ is the position operator of the electron with respect to the nucleus. Because $\hat{l}$ is antisymmetric, the dipole moment of atomic eigenstates $\langle a \rangle$ vanishes:

$$\langle \hat{d} \rangle = \langle a|\hat{d}|a\rangle = 0 \; . \tag{2.25}$$

Superpositions of eigenstates like $c_1 \cdot |g\rangle + c_2 \cdot |e\rangle$, may have a non vanishing dipole moment:

$$\begin{aligned} \langle \hat{d} \rangle &= c_1^* c_1 \langle g|\hat{d}|g\rangle + c_2^* c_2 \langle e|\hat{d}|e\rangle + c_1^* c_2 \langle e|\hat{d}|g\rangle + c_2^* c_1 \langle g|\hat{d}|e\rangle \\ &= c_1^* c_2 \langle e|\hat{d}|g\rangle + c_2^* c_1 \langle g|\hat{d}|e\rangle \; . \end{aligned} \tag{2.26}$$

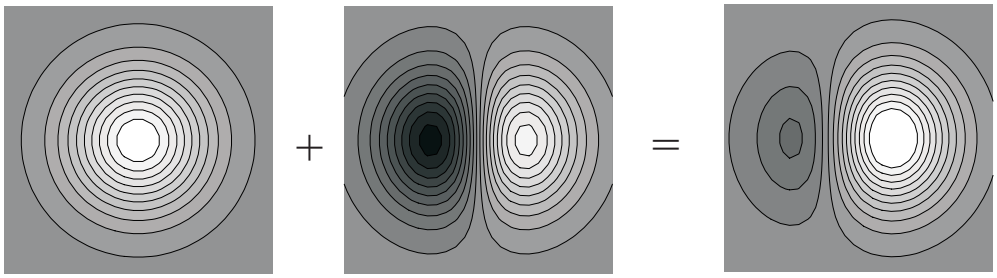

Fig. 2.1: Qualitative graph of the superposition of an s-orbital (left-hand side) and a p-orbital (middle) to a superposition state (right hand side).

Such a superposition of states as shown in figure 2.1 exists for example during the transition between different eigenstates. As long as the Bloch vector has nonzero components in the uv-plane there is always an effective dipole moment induced.

The dipole moment operator may be expressed as:

$$\hat{d} \; = \; d_{ge}|g\rangle\langle e| + d_{eg}|e\rangle\langle g| \; = \; d_{ge}(|g\rangle\langle e| + |e\rangle\langle g|) \; . \tag{2.27}$$

Using equation 2.4-2.6, the expectation value of the dipole moment operator for a single atom driven by a monochromatic electromagnetic field is given by:

$$\langle \hat{d} \rangle = d = 2d_{ge}(u \cdot cos(\omega_{\mathrm{L}} t) - v \cdot sin(\omega_{\mathrm{L}} t)) \; . \tag{2.28}$$

The steady state expectation value of the dipole moment is (equation 2.14-2.16):

$$d_{\mathrm{st}} = \frac{2d_{ge}}{\Omega} \frac{s}{s+1} (\delta_{\mathrm{L}} \cdot cos(\omega_{\mathrm{L}} t) - \frac{\Gamma}{2} \cdot sin(\omega_{\mathrm{L}} t)) \; . \tag{2.29}$$

d oscillates at the laser frequency and there is a phase shift between the dipole moment and the driving electromagnetic field which depends on the detuning. If $\delta_{\mathrm{L}} = 0$ the $cos(\omega_{\mathrm{L}} t)$ term vanishes and the phase shift is $\pi/2$.

The amplitude of the dipole moment is:

$$d_0 = 2d_{ge}\sqrt{u^2 + v^2}\,. \tag{2.30}$$

The amplitude of the expectation value in steady state, expressed in terms of I_0 and δ_L is:

$$d_{0,\mathrm{st}} = \sqrt{\frac{3\Gamma\varepsilon_0 hc^3}{\omega_0^3}} \cdot \frac{\sqrt{\frac{I_0}{I_\mathrm{sat}} \cdot (1 + \frac{4\delta_\mathrm{L}^2}{\Gamma^2})}}{1 + \frac{4\delta_\mathrm{L}^2}{\Gamma^2} + \frac{I_0}{I_\mathrm{sat}}}\,. \tag{2.31}$$

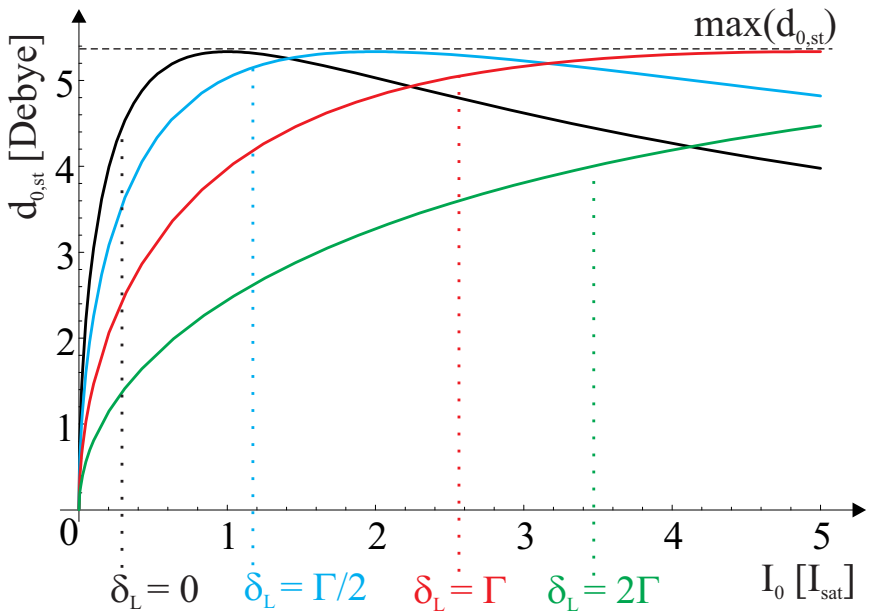

Fig. 2.2: Expectation value of the dipole moment versus I_0 in steady state for different δ_L. $1Debye = 3.336 \cdot 10^{-30}$Cm is the dipole moment of two charges $+e$ and $-e$ separated by a distance of 0.208Å.

Figure 2.2 shows the steady state amplitudes of dipole moment calculated using equation 2.31 versus the intensity of the driving field for different δ_L. Only the intensity at which the dipole moment has its maximum depends on the detuning, but not the value at the maximum itself. The largest possible dipole moment is reached if:

$$I_0 = I_\mathrm{sat}\left(1 + \frac{4\delta_\mathrm{L}^2}{\Gamma^2}\right)\,, \tag{2.32}$$

and its magnitude is given by:

$$\max(d_{0,\mathrm{st}}) = \sqrt{\frac{3\Gamma\varepsilon_0 hc^3}{\omega_0^3}} \cdot \frac{1}{2}\,. \tag{2.33}$$

Note that 2.33 is independent of both parameters δ_L and I_0. Hence, for every detuning the highest possible dipole moment can be obtained by choosing the incident intensity according to equation 2.32.

2.1.5 Scattering Cross Section

The intensity within a medium is described by the one dimensional differential equation [34]:

$$\frac{dI(x)}{dx} = -\sigma_{\text{scat}} n(x) I(x) \ , \tag{2.34}$$

where σ_{scat} is the *scattering cross section* and $n(x)$ the local density. The number of scattered photons is equal to the number of spontaneous emissions, and the scattering cross section can be expressed as:

$$\sigma_{\text{scat}} = \frac{\Gamma \hbar \omega_{\text{L}}}{I_0} \cdot \sigma_{\text{st}} \quad , \tag{2.35}$$

where σ_{st} is the population of the excited state. By expressing σ_{st} in terms of δ_{L} and I_0, equation 2.35 becomes:

$$\sigma_{\text{scat}} = \frac{\Gamma \hbar \omega_{\text{L}}}{2 I_{\text{sat}}} \cdot \frac{1}{1 + \frac{4\delta_{\text{L}}^2}{\Gamma^2} + \frac{I_0}{I_{\text{sat}}}} \quad . \tag{2.36}$$

In the limit $I_0 \ll I_{\text{sat}}$ and $\delta_{\text{L}} = 0$, σ_{scat} is independent of the intensity and equal to the absorption cross section:

$$\sigma_{\text{scat}} = \sigma_0 = \frac{\Gamma \hbar \omega_{\text{L}}}{2 I_{\text{sat}}} = \frac{3\lambda^2}{2\pi} \ , \tag{2.37}$$

where λ is the wavelength of the incident beam. σ_0 is the well known formula for the absorption cross section in the low intensity regime.

2.2 Dipole Potentials

Two equivalent charges q of different sign separated by some distance $\vec{l}$ are called a *dipole* as already mentioned. The dipole moment is defined as $\vec{d} = q \cdot \vec{l}$. A static dipole is the source of an electric field, a dynamic dipole of an electromagnetic field. The classical potential of a static dipole acting on a positive probe charge is given by:

$$V(\vec{r}) = \frac{1}{4\pi\varepsilon_0} \frac{\vec{r} \cdot \vec{d}}{|\vec{r}|^3} \ , \tag{2.38}$$

where $\vec{r}$ is the position of the probe charge with respect to the dipole. Equation 2.38 is only valid for a point-like dipole, but for distances $\vec{r}$ which are large compared to the separation of the charges of the dipole, it is a very good approximation.

The spatial distribution of the interaction potential of a dipole and a positive probe charge is shown in figure 2.3.

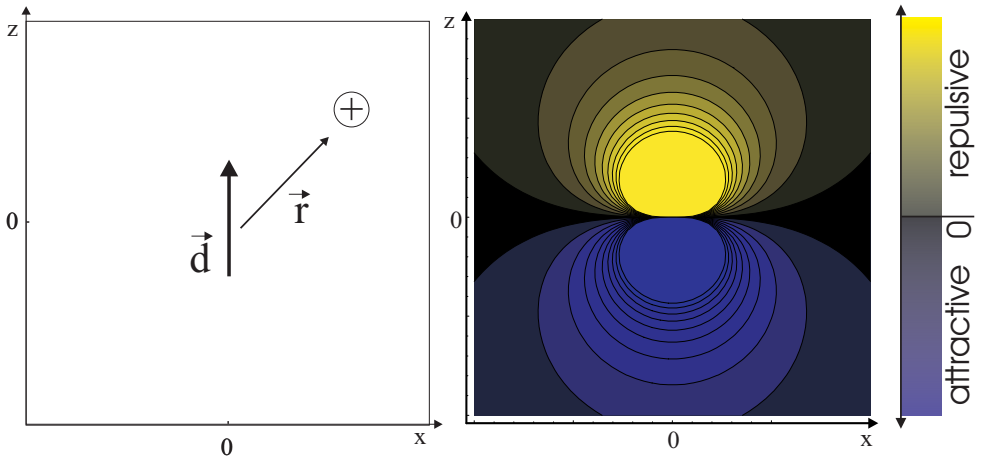

Fig. 2.3: Qualitative graph of the interaction potential of a static dipole and a positive probe charge separated by $\vec{r}$ in the xz-plane (right-hand side). The dipole is located at $x, y, z = 0$ and points into the z-direction (as depicted on the left-hand side). The yellow field corresponds to a repulsive and the blue to an attractive potential felt by the probe charge. The potential is cylindrical symmetric in the z-direction.

2.2.1 Static Dipole-Dipole Interaction

The interaction potential of two static dipoles is given by [32]:

$$V_{\mathrm{AB}}(\vec{r}) = \sum_{i,j} \frac{d_{\mathrm{A},i}\, d_{\mathrm{B},j}}{4\pi\varepsilon_0 r^3} \cdot (\delta_{ij} - 3\frac{r_i\, r_j}{r^2}) \,, \tag{2.39}$$

where A, B are the dipoles, i, j refer to the components of the vectors, $\vec{r}$ is the relative position of the dipoles and $r = |\vec{r}|$. By considering two parallel dipoles pointing into the z-direction and rewriting equation 2.39 in spherical coordinates, the interaction potential becomes:

$$\vec{r} = \begin{pmatrix} r\sin(\theta)\cos(\phi) \\ r\sin(\theta)\sin(\phi) \\ r\cos(\theta) \end{pmatrix} \quad : \quad V_{\mathrm{AB}}(\vec{r}) = \frac{d(\mathrm{A})d(\mathrm{B})}{4\pi\varepsilon_0 r^3} \cdot (1 - 3\cos^2(\theta)) \,. \tag{2.40}$$

As shown in figure 2.4 the potential has attractive and repulsive parts. If the dipoles are separated in the z-direction ($x, y = 0$) the interaction is attractive, if they are separated in the x, y-direction ($z = 0$) it is repulsive. There is an angle of vanishing interaction ($V_{\mathrm{AB}} = 0$), the so called *magic angle* $\theta_{\mathrm{magic}} = 54.74°$, where the attractive and repulsive parts of the potential cancel each other.

2.2.2 Dynamic Dipole-Dipole Interaction

We discussed in section 2.1.4 that the light induced dipoles are oscillating at the optical frequency ω_{L}. Since we are not able to measure any effects

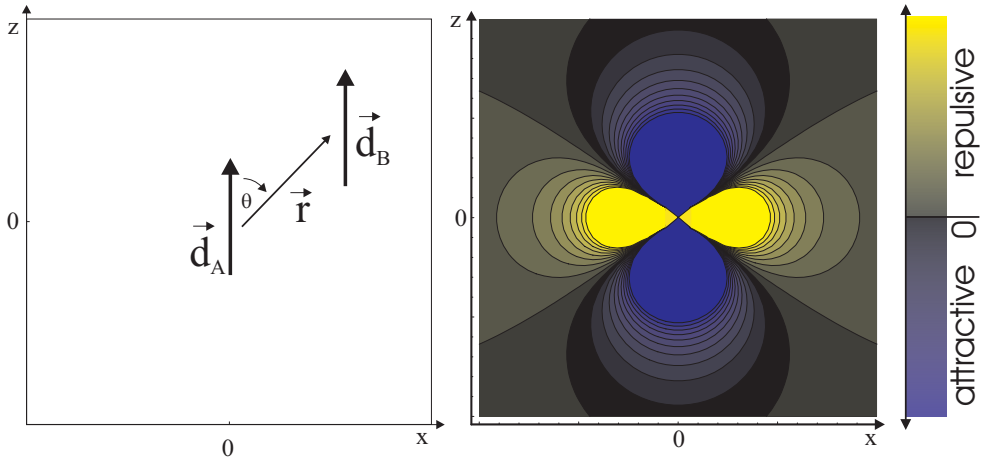

Fig. 2.4: Qualitative graph of the interaction potential of two static dipoles in the xz-plane (right-hand side). One dipole is located at $x, y, z = 0$, the second at $\vec{r}$ and both point into the z-direction (as depicted on the left-hand side). The yellow field corresponds to a repulsive and the blue to an attractive potential felt by the second dipole. The potential is cylindrical symmetric in the z-direction.

at these frequencies, time averages have to be considered. The time average over a period of oscillation of any interaction between the oscillating dipole and a static charge or dipole is zero. The timescale on which the interaction of two oscillating dipoles is averaged out is given by the decoherence time of the dipoles and by their inverse beat frequency. This timescale might become large for long coherence times and similar oscillation frequencies of the dipoles.

In our qualitative picture the dipole A emits an electromagnetic field. The electromagnetic field travels to the position of dipole B and interacts there with the charges of B. In order to derive the potential of the light induced dipole-dipole interaction, the *retardation* has to be taken into account. The electromagnetic field emitted at A needs a time Δt to reach B. During Δt, the phase of both dipoles changes due to the driving field. If the phase shift is small, the interaction is approximately equal to the interaction of static dipoles. If the phase shift is of the order of π the dipoles point into the opposite direction and the interaction changes its sign. Hence, the interaction potential is oscillatory with the separation.

As an example we consider the interaction of two parallel dipoles pointing into the z-direction. The dipoles are separated in the x-direction ($y, z = 0$) while the incident beam, which is the driving electromagnetic field, is travelling into the y-direction. If the separation is much smaller than the wavelength of the electromagnetic field, the interaction is repulsive. If the separation is half a wavelength, the phase difference is π and the second dipole points into the opposite direction when the electromagnetic field arrives. Hence, the interaction is attractive. If the separation is a wavelength, the phase difference is 2π and the interaction is repulsive again.

There are two types of forces that dominate the interaction between the atoms. The first arises from the induced dipole moment of one oscillating dipole acted on by the electric field of the other oscillating dipole. The second, perhaps more interesting force, is a magnetic force that arises from the interaction between the induced currents in the two dipoles. This interaction results from a Lorentz-force involving a cross product of the time derivative of the dipole moment with the magnetic-flux density from the other dipole. When the separation between the two induced currents is perpendicular to the electric field polarization of the incident field this force dominates all others.

The full interaction potential is given by the equation [32]:

$$V_{\mathrm{AB}}(\vec{r}) = \frac{d_{\mathrm{A}} d_{\mathrm{B}} \cos(\vec{k}\cdot\vec{r}+\Delta\phi)}{4\pi\varepsilon_0 r^3} \cdot \sum_{i,j}[(\delta_{ij} - 3\tfrac{r_i\, r_j}{r^2})(\cos(kr) + kr\sin(kr)) - (\delta_{ij} - \tfrac{r_i\, r_j}{r^2})(k^2 r^2\cos(kr))] \,, \tag{2.41}$$

where d_{A} and d_{B} are the amplitudes of the dipole moments of the two atoms, $\vec{r}$ is the separation of the dipoles, $\vec{k}$ the wavevector of the electromagnetic field, $r = |\vec{r}|$ and $k = |\vec{k}|$. The $\cos(\vec{k}\cdot\vec{r})$ term is the phase difference of the dipoles due to the driving field. An additional phase shift $\Delta\phi$ occurs if for example the two levels of the atom are shifted differently by additional potentials.

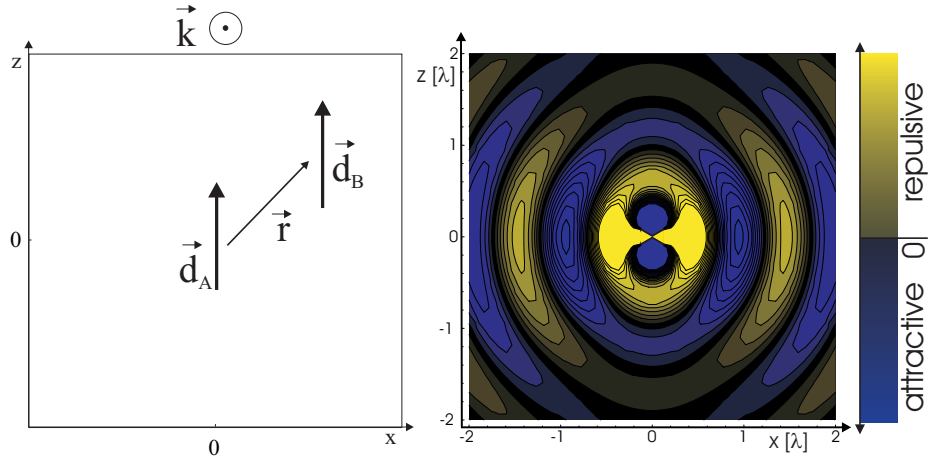

Fig. 2.5: Qualitative graph of the retarded interaction potential of two light induced dipoles in the xz-plane (right-hand side). One dipole is located at $x, y, z = 0$ and the second at $\vec{r}$ (as depicted on the left-hand side). The z-polarized driving field is travelling into the y-direction. The yellow field corresponds to repulsive and the blue to attractive potentials felt by the second dipole.

Figure 2.5 and figure 2.6 show the interaction potential in the xz- and the yz-plane, for an incident light beam linearly in the z-direction polarized that is travelling into the y-direction. The potential is anisotropic and oscillatory on the scale of the wavelength. The maxima and minima of the interaction

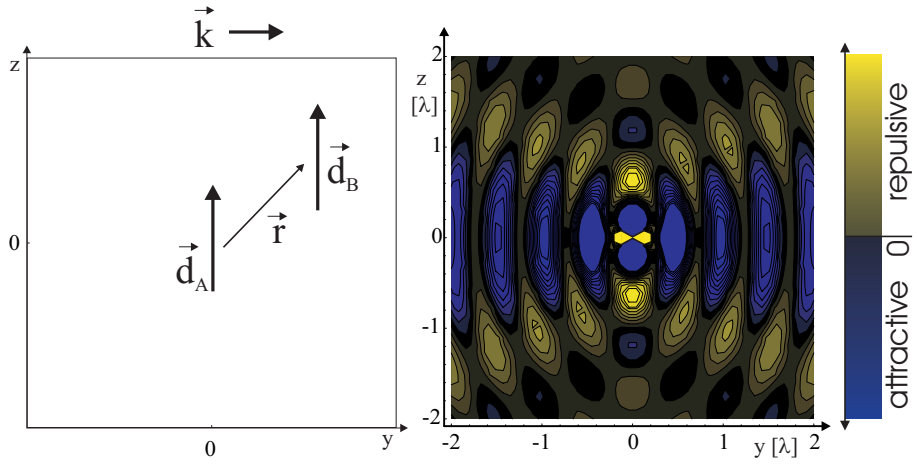

Fig. 2.6: Qualitative graph of the retarded interaction potential of two light induced dipoles in the yz-plane (right-hand side). One dipole is located at $x, y, z = 0$ and the second at $\vec{r}$ (as depicted on the left-hand side). The z-polarized driving field is travelling into the y-direction. The yellow field corresponds to repulsive and the blue to attractive potentials felt by the second dipole.

potential in the x- and z-direction are separated due to the retardation by λ, respectively. In the y-direction, the direction of the wavevector of the driving field the separation of the maxima and of the minima is $\lambda/2$. This results from the additional phase-change of the driving field in this direction.

2.2.3 Many Interacting Dipoles

In the sections above we have discussed the interaction of two localized dipoles, but in the experiment we are investigating the interaction of many atoms. Therefore, we have to extend the picture to more than two dipoles.

The light induced dipole-dipole interaction potential of N dipoles acting on a probe dipole that is driven by the same electromagnetic field is given by:

$$U_{\text{liddi}}(\vec{r_0}) = \sum_{i=1}^{N} V_{i0}(\vec{r_i} - \vec{r_0}) \ , \tag{2.42}$$

where r_i is the position of dipole i, r_0 is the position of the probe dipole and V_{i0} is the interaction potential of dipole i and the probe dipole. By making the transition from localized objects to a density distribution, the sum becomes an integral and the potential can be expressed as:

$$U_{\text{liddi}}(\vec{r_0}) = \int_{-\infty}^{\infty} V_{\text{AB}}(\vec{r_0} - \vec{r}) n(\vec{r}) d^3r \ , \tag{2.43}$$

where $n(\vec{r})$ is the density distribution of the atoms. In general there is no analytic solution of equation 2.43, but as we are interested in the interaction potential of many delocalized dipoles this is exactly what we need to

calculate. The numerical computation of this equation will be presented and discussed in chapter 4.

2.3 Bose-Einstein Condensation

The atom cloud in our experiment is a *BEC* (Bose-Einstein Condensate) in an optical lattice. A general overview is presented in [35–37]. The properties of a BEC are advantageous for the analysis of the light induced dipole-dipole interaction. To a good approximation all atoms are decribed by the same wavefunction. The temperature is lower and the density is higher than in the case of a thermal gas cloud. The optical lattice imprints a structure smaller than the wavelength of the light field inducing the dipole-dipole interaction, which is important, since the static part of the interaction vanishes for clouds with isotropic density distribution on the scale of the wavelength as shown in Appendix A.

2.3.1 Non-Interacting Bosons

We consider an ensemble of cold bosonic atoms in a harmonic trap. Due to the quantum statistics a transition from a thermal cloud to a BEC can be achieved, by cooling the ensemble below a certain threshold temperature which is called the *critical temperature* T_c. The transition is described in the grand canonical ensemble, where the exchange of particles and energy with a reservoir is allowed. The interaction of the atoms will be neglected for the moment. The trap potential is given by:

$$U_\mathrm{trap}(\vec{r}) = \frac{1}{2}m(\omega_x^2 x^2 + \omega_y^2 y^2 + \omega_z^2 z^2) \;, \tag{2.44}$$

where m is the mass of the bosons and $\omega_{x,y,z}$ are the trap frequencies. The eigenenergies of the trap potential are:

$$E_l = \left(l_x + \frac{1}{2}\right)\hbar\omega_x + \left(l_y + \frac{1}{2}\right)\hbar\omega_y + \left(l_z + \frac{1}{2}\right)\hbar\omega_z \;, \tag{2.45}$$

where $l_{x,y,z}$ are natural numbers.

The state of the system may be described by the grand canonical N-particle density matrix:

$$\hat{\rho} = \frac{1}{Z}\exp(-\beta(\hat{H} - \mu\hat{N})) \;, \tag{2.46}$$

where $\hat{H}$ is the Hamilton operator of the system, $\hat{N}$ the particle number operator, Z the partition function, μ the chemical potential and $\beta = 1/k_B T$ the inverse temperature with k_B the Boltzman constant. μ is the energy needed for adding an additional particle to the system.

By using standard quantum statistical methods described in many textbooks (eg. [37]) the number of particles in a given state can be calculated with respect to the density matrix and written in terms of:

$$n_l = \left[\frac{1}{z}\exp(\beta E_l) - 1\right]^{-1} , \tag{2.47}$$

where $z = \exp(\beta\mu)$ is the so called *fugacity*. The fugacity is the tendency of a gas to expand or escape (from one phase to another). Since for bosons $\mu \leq 0$, the fugacity has the limits:

$$0 \leq z \leq 1 . \tag{2.48}$$

The number of particles in the system is given by $N = \sum_l n_l$. We separate this quantity into the number of particles in the ground state of the trap potential N_0 and the number of particles in the excited states of the trap potential N' and find by setting $z = 1$ that there is an upper limit for the number of particles in the excited states:

$$N' = \sum_{l\neq 0}\left[\frac{1}{z}\exp(\beta E_l) - 1\right]^{-1} \quad < \quad \sum_{l\neq 0}\left[\exp(\beta E_l) - 1\right]^{-1} = N'_{\max} . \tag{2.49}$$

In the quantum degenerate regime ($z \to 1$) the number of atoms in the excited states is saturated and the ground state is macroscopically populated, since

$$N_0 = \frac{z}{1-z} \quad \xrightarrow[z\to 1]{} \quad \infty , \tag{2.50}$$

is diverging for ($z \to 1$). The transition occurs, when the phase space density $D(T, n)$ becomes larger than the critical value:

$$D_c(T_c, n_0) := \frac{\rho_0 \cdot \Lambda_B^3(T_c)}{\hbar^3} \approx 2.612\hbar^{-3} , \tag{2.51}$$

where $\Lambda_B(T) = \sqrt{\frac{h^2}{2\pi m k_B T}}$ is the thermal de Broglie wavelength and ρ_0 is the density in the center of the trap. The phase space density multiplied by $\hbar^3$ corresponds to the number of atoms within a unit volume in phase space.

The critical temperature T_c for atoms confined in a harmonic trap is:

$$k_B T_c = \frac{\hbar\overline{\omega}N^{1/3}}{[\zeta(3)]^{1/3}} \approx 0.94\,\hbar\overline{\omega}N^{1/3} , \tag{2.52}$$

where $\zeta(z) = \sum_{l=1}^{\infty} l^{-z}$ is Riemann's Zeta-function and $\overline{\omega} = (\omega_x\omega_y\omega_y)^{1/3}$ is the mean trap frequency.

In order to achieve quantum degeneracy the critical phase space density (equation 2.51) has to be reached by cooling the ensemble below the critical temperature (equation 2.52). For $T = 0$ all atoms are in the ground state of the trap potential.

2.3.2 Interacting Bosons

The short-range interatomic interaction can be described in terms of a mean-field approach with the interaction potential:

$$V(\vec{r}-\vec{r}_0) = g\delta(\vec{r}-\vec{r}_0) \ , \tag{2.53}$$

where $g = \frac{4\pi\hbar^2 a}{m}$ is the coupling constant and a is the s-wave scattering length. The probability wavefunction is described by the Gross-Pitaevskii equation:

$$\left(-\frac{\hbar^2}{2m}\nabla^2 + U_{\rm pot}(\vec{r}) + g|\Phi(\vec{r})|^2\right)\Phi(\vec{r}) = \mu\Phi(\vec{r}) \ . \tag{2.54}$$

It is possible to classify the BEC by comparing the kinetic and the interaction energy: $\frac{E_{\rm int}}{E_{\rm kin}} \propto \frac{N|a|}{\overline{a}_{\rm ho}}$, where $\overline{a}_{\rm ho} = \sqrt{\hbar/(m\overline{w})}$ is the average width of the trap potential. There are two regimes [38]:

- $\sqrt{\frac{2}{\pi}}\frac{N|a|}{\overline{a}_{\rm ho}} \ll 1$, linear regime of the harmonic oscillator
- $\sqrt{\frac{2}{\pi}}\frac{N|a|}{\overline{a}_{\rm ho}} \gg 1$. hydrodynamic regime

We can estimate a characteristic length scale of the BEC by setting the kinetic and the interaction energy to be equal. The *healing length* ξ is the scale on which perturbations of the density distributions are smoothed out.

$$E_{kin} = E_{int} \ \Rightarrow \ \xi = \frac{1}{\sqrt{8\pi\rho_0 a}} \ . \tag{2.55}$$

In the hydrodynamic regime the interaction energy is dominant and the kinetic energy may be neglected, which is called *Thomas-Fermi approximation*. The density distribution becomes:

$$n(\vec{r}) = |\Phi(\vec{r})|^2 = \begin{cases} \frac{\mu - U_{\rm pot}(\vec{r})}{g} & ,\text{if} \quad U_{\rm pot}(\vec{r}) \le \mu \\ 0 & ,\text{if} \quad U_{\rm pot}(\vec{r}) > \mu \ , \end{cases} \tag{2.56}$$

which for a harmonic trap potential is a parabolic function for $U_{\rm pot}(\vec{r}) \le \mu$. The chemical potential is given by:

$$\mu = \frac{15^{2/5}}{2}\left(\frac{Na}{\overline{a}_{\rm ho}}\right)^{2/5}\hbar\overline{\omega} \ , \tag{2.57}$$

and the mean interaction energy per atom by:

$$\frac{E_{\rm int}}{N} = \frac{7}{2}\mu \ . \tag{2.58}$$

The *Thomas-Fermi radius* $R_{\rm TF}$ is the distance from the center of the trap to the edge of the density distribution:

$$R^2_{{\rm TF},i} = \frac{2\mu}{m\omega_i^2} \quad , \quad i = x, y, z \ . \tag{2.59}$$

2.4 Optical Traps / Optical Lattices

In a far detuned light beam, the induced dipole moment of an atom interacts with the electric field. The dispersive interaction between the gradient of the intensity and the dipole moment leads to *dipolar forces* discussed in [30, 39]. Due to these dipolar forces atoms can be trapped in a laser beam.

Optical lattices are optical traps with perfectly periodic potentials and have a wide range of applications in atom optics [40, 41]. In combination with a BEC they are used for example to model crystal structures or as tools for investigating different properties of the atomic clouds as in momentum spectroscopy [42].

An optical lattice may be produced by overlapping two or more at least partially counterpropagating electromagnetic waves with non-orthogonal polarizations. In the case of two laser fields at the same frequency, the optical lattice is a standing electromagnetic wave. The one dimensional potential for a retro reflected 1D lattice along the direction of the standing wave is derived in [43]:

$$U(z) = \left(-\frac{3\pi c^2 \Gamma}{\omega_0^2 - \omega^2} \cdot 4 I_0 \right) \cdot \cos^2(k_{\mathrm{lat}} z) = -U_{\mathrm{lat}} \cdot \cos^2(k_{\mathrm{lat}} z) \; , \tag{2.60}$$

where k_{lat} is the wavevector of the standing wave, z is the position within the lattice and U_{lat} the depth of the potential. Usually, the depth of the lattice potential is expressed in *recoil energies*:

$$E_{\mathrm{rec}} = \frac{\hbar^2 k_{\mathrm{lat}}^2}{2m} \; , \tag{2.61}$$

where m is the mass of the atom.

If the kinetic energy of the atoms is much smaller than the potential energy of the lattice, the trap can be approximated by a harmonic potential. The expansion for small values of z gives:

$$U(z) = -U_{\mathrm{lat}} \cdot \cos^2(k_{\mathrm{lat}} z) \approx U_{\mathrm{lat}}(-1 + k_{\mathrm{lat}}^2 z^2) \; . \tag{2.62}$$

If the BEC has a cigar shape, the optical lattice is directed into the axial direction of the cloud and the confinement in the radial direction is much smaller than the confinement due to the optical lattice, then the density distribution will consist of thin discs separated by half the wavelength of the lattice beams in the axial direction. The density distribution within the discs is given by:

$$\begin{aligned} n(z) &= \tfrac{N}{\pi^{1/2}} \tfrac{1}{z_{\mathrm{lat}}} \exp\left(-\tfrac{z^2}{z_{\mathrm{lat}}^2} \right) \\ \text{with} \quad z_{\mathrm{lat}} &= \tfrac{1}{2} \sqrt{\tfrac{\hbar \lambda_{\mathrm{lat}}}{\pi} \tfrac{1}{(U_{\mathrm{lat}} m)^{1/2}}} \; , \end{aligned} \tag{2.63}$$

where λ_{lat} is the wavelength of the lattice beams and z_{lat} is the full width of a disc measured from $1/e^2$ of the peak density on one side to $1/e^2$ on the other

side. For optical potentials on the order of a few hundred E_{rec}, the width of the discs is an order of magnitude smaller than the wavelength and the density an order of magnitude higher than the density of the BEC without a lattice.

2.5 Summary

In this chapter we introduced all quantities needed for the calculation of the mechanical effects caused by the light induced dipole-dipole interaction. To be able to maximize the effects caused by the interaction the dependency of the potential on the parameters was investigated:

- Dipole moment:
  The interaction potential of two dipoles is proportional to the dipole moment of both atoms. The dipole moment is maximized by choosing the detuning and the intensity of the incident beam with respect to equation 2.32:
  $$I_0 = I_{\mathrm{sat}}\left(1 + \frac{4\delta_{\mathrm{L}}^2}{\Gamma^2}\right) . \tag{2.64}$$

- Density and atom number:
  The effective interaction potential is proportional to the density of the cloud. Since the light induced dipole-dipole interaction is a long range interaction, not only the local density is of importance but also the number of atoms within the range of interaction. The length scale of the interaction is given by the optical wavelength (equation 2.41).

- Size and shape of the gas cloud:
  As described in Appendix A the static part of the interaction vanishes for isotropic distributions of dipoles. Hence, the density distribution should not be isotropic on the scale of the interaction in order to maximize the potential. On the other hand, if the distribution is much larger than the wavelength, the interaction potential is averaged out due to its oscillatory behavior. Therefore, the width of the cloud perpendicular to the optical lattice should be on the order of the wavelength.

- Temperature:
  The interaction potential is oscillating spatially on the scale of the wavelength. If the atoms move significantly on this scale during the interaction, the attractive and repulsive parts of the interaction will partially cancel each other and the effective potential will be decreased. The temperature of the cloud has to be:
  $$T \ll \frac{m\lambda^2}{k_B \Delta t^2} \tag{2.65}$$
  where λ is the wavelength of the incident electromagnetic wave Δt the time of interaction.

Due to their properties Bose-Einstein condensates are an outstanding tool for the investigation of the light induced dipole-dipole interaction. High densities can be produced at low temperatures. With an optical lattice we are able to transform the 3D-cloud into many separate quasi 2D-discs and increase the density by an order of magnitude.

3. Experimental Setup

In this chapter we are going to present the experimental apparatus and the techniques used for the measurements. A short review on the element Rubidium is followed by the discussion of the different parts of the experiment consisting of the vacuum system, the laser system, the trapping and cooling part and the imaging. An the end of this chapter the design of the optical lattice and its properties are presented.

3.1 Rubidium

Alkali atoms are commonly used for laser cooling and magnetic trapping because of their relatively simple hydrogen-like term scheme and advantageous properties. Especially Rubidium has earned itself a reputation as a workhorse because it is relatively easy to handle. Its relevant transitions are located around 780nm, which can be accessed by commercial diode and titanium-sapphire laser systems. Due to its high vapor pressure of $4 \cdot 10^{-7}$mbar at room temperature, gaseous Rubidium may be generated efficiently by heating slightly above room temperature.

The two natural most abundant isotopes of Rubidium are ^{85}Rb with 72% and ^{87}Rb with 28%. In our experiment ^{87}Rb is used because ^{85}Rb has a negative scattering length at magnetic field strengths common for magnetic trapping and ^{87}Rb has favorable collision parameters. ^{87}Rb is radioactive but stable on the usual timescale of the experiment. It decays by a β^--transition into ^{87}Sr, with a lifetime of 4.88 10^{10} years [44]. 32 other isotopes are known [45], the most prominent are ^{83}Rb ($\tau = 86.2$days), ^{84}Rb ($\tau = 32.77$days) and ^{86}Rb ($\tau = 18.631$days).

Some physical properties of ^{87}Rb are [46, 47]:

mass	m	86.909 180 520(15) u 1.443 160 60(11) $\times 10^{-25}$kg
Melting point at 1013mbar	T_{M}	39.31°C
Boiling point at 1013mbar	T_{B}	688°C
vapor pressure at 25°C	P_{V}	4 $\times 10^{-7}$mbar

Figure 3.1 shows the hyperfine levels of ^{87}Rb. For the light induced dipole-dipole interaction the transition $|5^2\mathrm{S}_{1/2}, \mathrm{F}{=}2, \mathrm{m_F} = 2\rangle \rightarrow |5^2\mathrm{P}_{3/2}, \mathrm{F}{=}3, \mathrm{m_F} = 2\rangle$ (indicated by the dotted line) is considered. Its relevant optical properties are:

D_2-line		$5^2S_{1/2} \rightarrow 5^2P_{3/2}$	
Wavelength (vacuum)	λ	780.246 291 692(11)	nm
Wavelength (air)	λ_{air}	780.037 08	nm
Frequency	ω_0	$2\pi \cdot 384.2279818773(55)$	THz
Lifetime $5^2P_{3/2}$	τ	26.24(4)	ns
Linewidth (FWHM)	Γ	$2\pi \cdot 6.065(9)$	MHz
Saturation intensity	I_{sat}	1.67	mW/cm^2
Recoil temperature at 780nm	T_{rec}	$(\hbar k)^2/mk_B = 361.95$	nK
Recoil velocity at 780nm	v_{rec}	$\hbar k/m = 5.8845$	mm/s

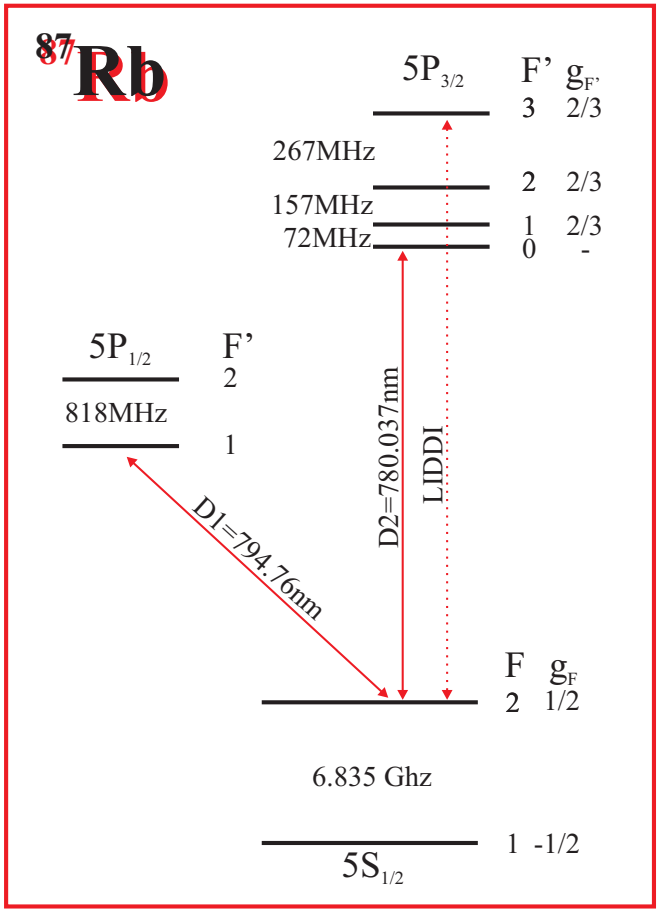

Fig. 3.1: Hyperfine levels of ^{87}Rubidium and the D_1- and D_2-line. The dotted line corresponds to the transition used for the light induced dipole-dipole interaction.

3.2 Setup

The design and the characterization of the experimental setup is described in detail in [43, 48, 49]. Here, we will only present the most important details and the changes made in the scope of this thesis.

The Bose-Einstein condensation and the experiments with ^{87}Rb are performed in a large volume ultra high vacuum chamber. A magneto-optical trap

(3D-MOT) is loaded by a collimated beam of slow atoms produced by transversal optical cooling (2D-MOT) in a Rubidium vapor cell. The cooling light at a wavelength of 780nm is produced by a Titanium-Sapphire laser, which is pumped by a frequency doubled $Nd : YVO_4$ laser system. Additional grating stabilized diode lasers are used for detection, optical pumping and repumping. Subsequent to the MOT the atoms are loaded into a magnetic trap, which is created by a set of water-cooled coils attached to the chamber and capable of carrying more than 1000A. The temperature of the trapped Rubidium cloud is decreased by Radio-frequency induced evaporative cooling until Bose-Einstein condensation is reached. The atomic clouds and condensates are observed with CCD-cameras.

3.2.1 Vacuum System

The vacuum system is divided by a differential pumping tube into two sections as shown in figure 3.2: the high vacuum (HV) section and the ultra high vacuum (UHV) section. The main components of the HV side are the Rb-reservoir and the glass cell of the 2D-MOT. The whole HV section is heated to about 40°C to increase the pressure of the Rubidium vapor in the 2D-MOT. The vacuum is maintained by a turbo pump with a pumping speed of 20 l/s. The pressure is about 10^{-6} to 10^{-7}mbar.

The HV part is connected to the UHV part by the differential pumping tube through which the atomic beam of the 2D-MOT enters the main chamber. The tube is normally blocked by a mechanical shutter and is only opened to load the 3D-MOT. The main vacuum chamber is connected via a five-way-cross to an ion-pump (200 l/s), a cryogenic reservoir and a Titanium-sublimator (ca. 1000 l/s). The main chamber was designed to combine the advantages of glass cells and steel chambers. It has a good optical access and the Ioffe-bars, which are introduced trough the four 'feedthrough' holes, are close to the atomic cloud. The UHV side operates at a pressure below $3 \cdot 10^{-11}$mbar.

3.2.2 Laser System

Four laser systems provide the experiment with light of different frequencies: the MOT laser, the repumper laser, the probe laser and the laser for the optical lattice. The first three systems are actively stabilized by feedback loops using doppler-free spectroscopy on Rb-vapor. Figure 3.3 shows the schematic of the laser setup used in the experiment.

The MOT laser is a Titanium-Sapphire solid state laser system (model *Coherent MBR 110*) and is pumped by a frequency doubled diode-pumped $Nd : YVO_4$ laser system (model *Coherent VERDI V-10*) with a maximal output power of 10.5W at 532nm. It provides the 2D- and 3D-MOT with a total power of 1.4W at 780nm. The laser beam can be redirected into the main

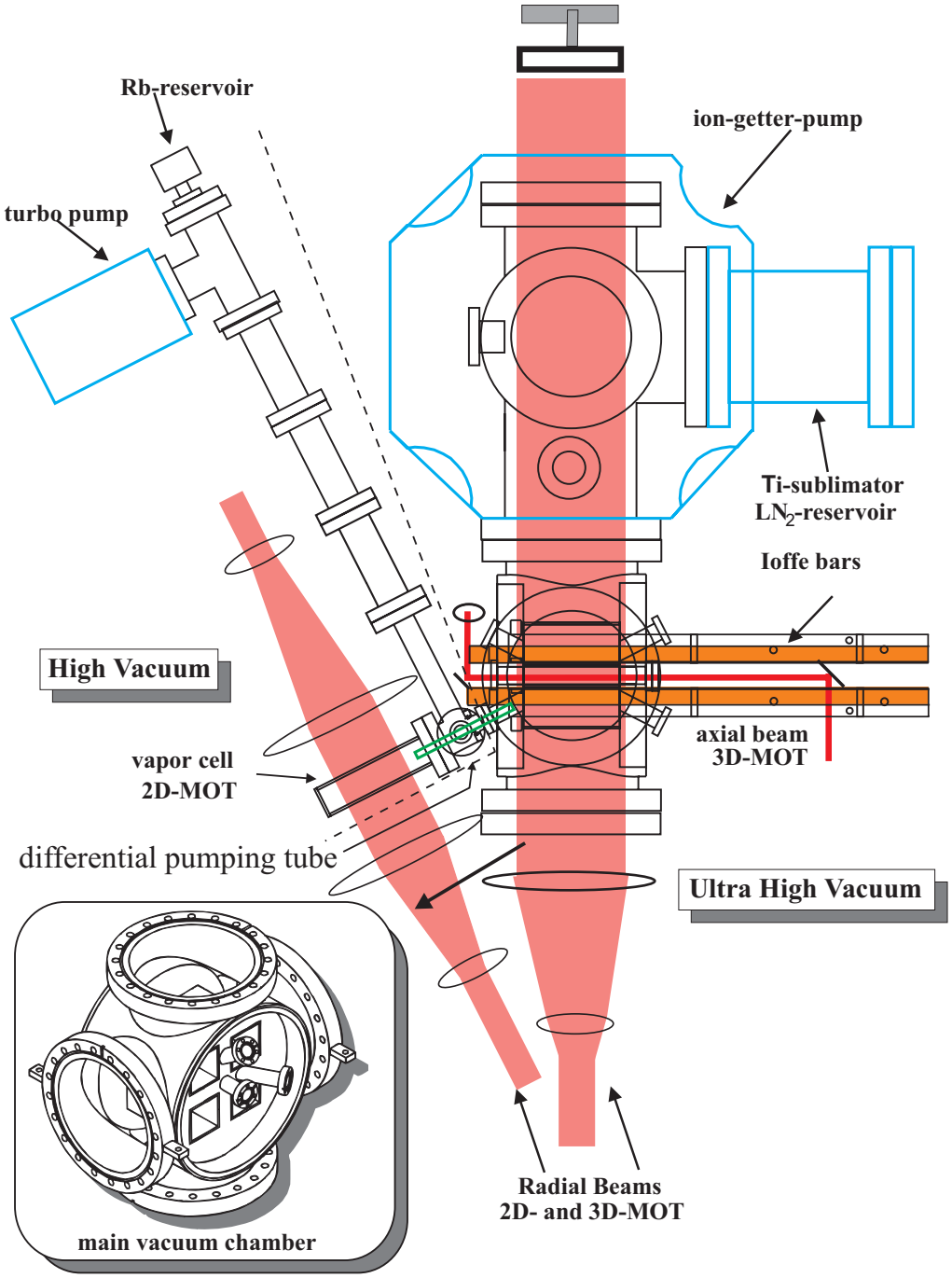

Fig. 3.2: Experimental setup. The dashed line divides the setup into the HV part and the UHV part. The main chamber is located at the center of the setup and is connected to the 2D-MOT by a differential pumping tube.

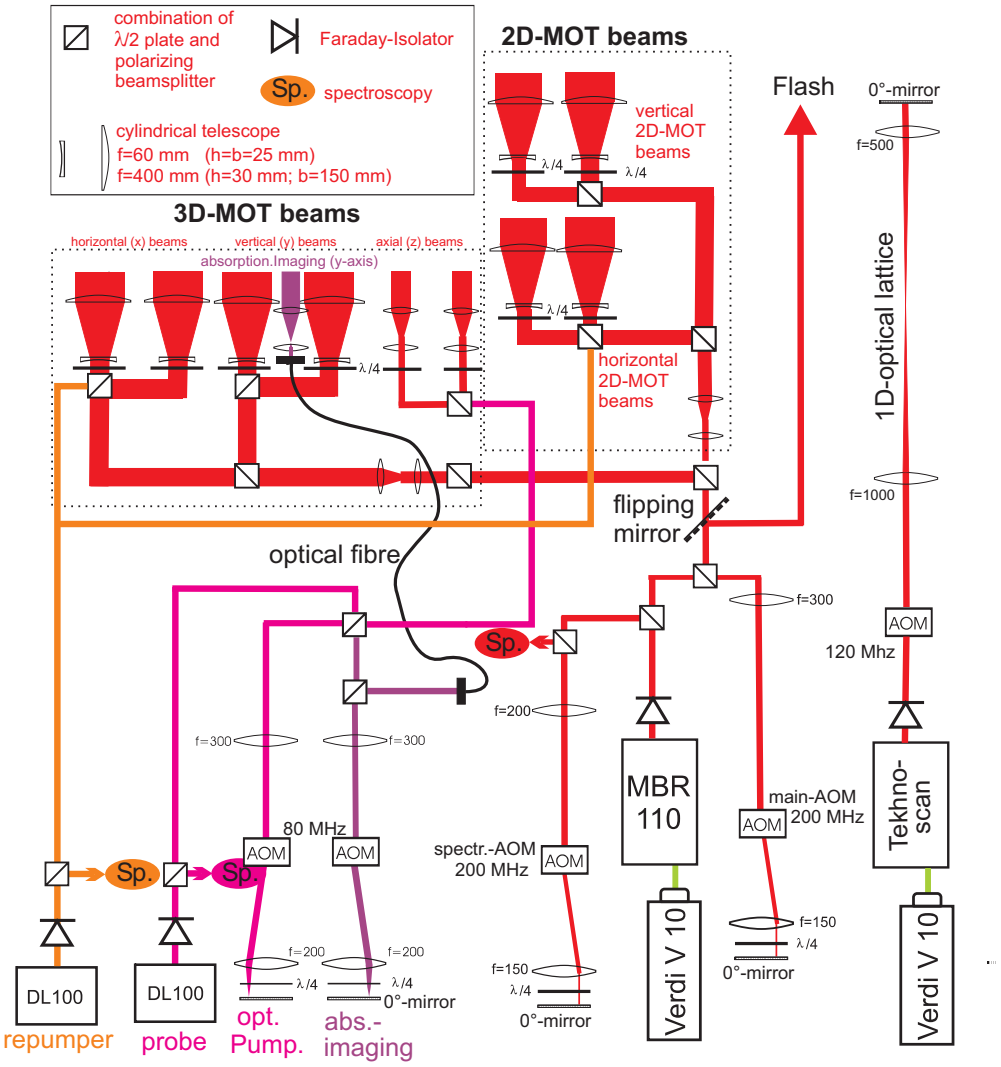

Fig. 3.3: Schematics of the laser setup used in the experiment. The cooling and trapping light is produced by a Titanium-Sapphire laser and passes twice through an AOM before it is split up into the beams for 2D- and 3D-MOT, switched by a flipping mirror it also provides the experiment with the resonant light needed for inducing dipoles. Two diode lasers are producing the light for repumping, optical pumping and detection by absorption imaging. The light for the optical lattice is produced by a second Titanium-Sapphire laser.

chamber by a flipping mirror to induce the dipole-dipole interaction in the cloud.

The repumper and the probe laser are self built grating stabilized diode lasers (using Sharp laser diodes and electronics from Toptica) with an output power of 60mW at 780nm. The repumper is used to transfer atoms back into the MOT cycle, which were removed by spontaneous decay. The light of the probe laser is used for optically pumping the atoms into the $m_F = 2$-state before introducing them into the magnetic trap and for absorption imaging as the probe beam.

The laser system of the optical lattice is a Titanium-Sapphire solid state laser system (model *Tekhnoscan TIS-SF-07*) and is pumped by a frequency doubled diode-pumped Nd : YVO_4 laser system (model *Coherent VERDI V-10*) with a maximal output power of 10W at 532nm. The maximal power output of the Tekhnoscan is 1.2W and the wavelength is tunable over a wide range between 750 and 850nm. A discussion in more detail on the setup of the optical lattice is given in section 3.3.

3.2.3 2D- / 3D-MOT and Magnetic Trap

The 2D-MOT is an intense source of slow atoms, its design and experimental results are described in [50]. It operates by transversally cooling Rb-vapor in two dimensions to create a collimated atomic beam. The 2D-MOT yields a flux of $2 \cdot 10^{10}$atoms/s of which about 50-60% can be captured by the 3D-MOT.

Detailed considerations and measurements concerning the 3D-MOT are presented in [51]. The main purpose of the 3D-MOT is the fast trapping of a large number of cold atoms. The prolate ellipsoid geometry of the 3D-MOT was chosen to improve the cooling capacity and efficiency. The atomic beam from the 2D-MOT is directed horizontally at an angle of 27° with respect to the z-axis (long axis of the MOT) into the trapping volume, hence incoming atoms are cooled by the axial and the radial beams along the whole length of the elongated MOT. The field gradient in the radial direction $dB/dr = 15$G/cm is generated by the quadrupole field of the Ioffe-bars operated at 40A, in the axial direction $dB/dz = 0.7$G/cm by the field of the extra-coils in anti-Helmholtz configuration operated at 17A. At the density reached in the MOT the atomic cloud becomes optically thick for the detuning of -2Γ of the MOT-beams. To increase the density and to decrease the temperature, the detuning of the MOT-beams is linearly ramped to -7Γ within a few ms. The density achieved is $4 \cdot 10^{10}\text{cm}^{-3}$ at $N = 6 \cdot 10^9$atoms and at $T = 40$ - 80μK. Due to the *detuned MOT* the phase-space density is increased to $D \approx 10^{-6}\hbar^{-3}$ (see equation 2.51).

From the detuned MOT the atoms are loaded into a Ioffe-Pritchard-type magnetic trap. The schematics of the trap is shown in figure 3.4. The radial confinement is generated by the quadrupole field of the Ioffe-bars and

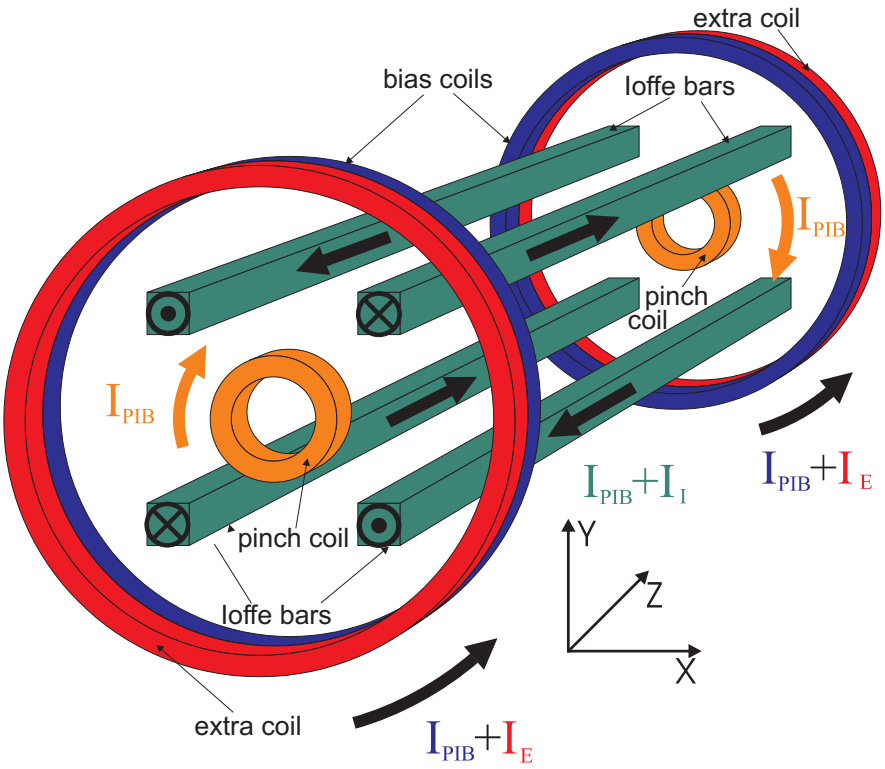

Fig. 3.4: Ioffe-Pritchard configuration of the elements creating the magnetic fields. The radial gradients are produced by the quadrupole field of the Ioffe bars, the axial by the dipole field of the pinch coils. The magnetic field offset generated by the pinch coils is compensated by the bias coils. The extra coils produce an adjustable offset field.

the axial confinement by the dipole field of the pinch-coils. After the atoms are loaded from the MOT into the magnetic trap the atomic cloud is adiabatically compressed. A high offset field is necessary for mode matching of the magnetic trap and the MOT but in order to reach high trap frequencies a compensation of the offset field generated by the pinch-coils is needed. Therefore, two additional coil pairs are integrated: with the extra-coils large offset fields can be added and with the bias-coils small offset fields nearly compensated.

The trapping frequencies for ^{87}Rb of the full compressed trap at $B'' = 4.5\text{G/cm}^2$, $B' = 400\text{G/cm}$ and $B_0 = 3.2 - 0.05\text{G}$ are $\omega_z = 2\pi \cdot 2.7\text{Hz}$ and $\omega_r = 2\pi \cdot 300 - 2300\text{Hz}$, an aspect ratio of up to $\omega_r/\omega_z = 850$ may be achieved. For an offset of $B_0 \approx 0.8\text{G}$ the number of atoms is typically $N = 4 \cdot 10^9$, the density is about $\rho_0 = 5.5 \cdot 10^{11}\text{cm}^{-3}$ and the phase space density $D \approx 1.3 \cdot 10^{-7}\hbar^{-3}$.

3.2.4 RF-Evaporative Cooling and Bose-Einstein Condensation

Evaporative cooling is the final step to reach Bose-Einstein condensation. The radio frequency (RF) is swept down in a sequence of linear ramps from 44.5MHz to a few kHz above the trap bottom.

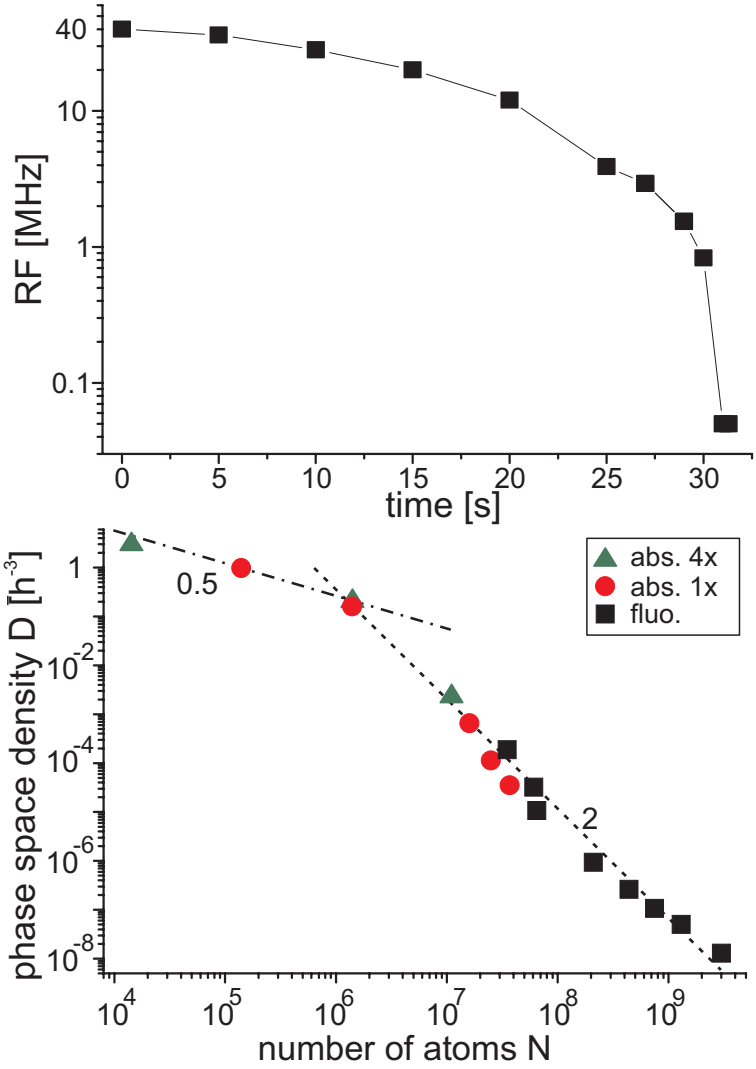

Fig. 3.5: Temporal progression of the RF-ramp (top) and the phase space density versus atom number (bottom) The different symbols correspond to different measurements.

Figure 3.5 shows on the top the temporal progression of the linear RF-ramps. The sequence was experimentally optimized. On the bottom the phase space density versus the atom number is plotted. Above $N = 10^6$ the efficiency of the evaporation is constant, below the efficiency decreases due to a heating rate of 2μK/s in the magnetic trap. At $N = 10^5$ Bose-Einstein condensation is initiated after an overall reduction of the atom number by four orders of magnitude.

3.2.5 Imaging and Time-of-Flight

In our experiment all information about the atomic clouds is extracted from images taken with CCD-cameras. From these images for different times of flight it is possible to determine the total number of atoms N, the density distribution $n(\vec{r})$ and by examining the rate of expansion the momentum distribution $\tilde{n}(\vec{k})$.

Two different imaging techniques are used in our experiment. Large clouds are probed by fluorescence imaging. The cloud is flashed by a highly saturated resonant laser beam and the resulting fluorescence recorded. The other technique is absorption imaging. The absorption of a mode-cleaned resonant laser beam due to the atomic cloud is observed. By comparing the image taken with a second image of the unperturbed beam, the optical density can be calculated. The optical density is proportional to the column density:

$$n'(x,z) = \int n(x,y,z)dy \; . \tag{3.1}$$

For the measurement of the momentum distribution the time-of-flight method is applied. The confinement is turned off at t_0 and the atoms expand freely. Absorption images are taken after different times-of-flight t. By analyzing the temporal evolution of the density distribution the momentum distribution can be calculated. For a thermal ensemble with a gaussian profile which was confined in a harmonic trap and was in steady state, the evolution of the full width of the density distribution σ_i measured from $1/e^2$ to $1/e^2$ is given by:

$$\sigma_i(t) = \sqrt{\sigma_i^2(t_0) + 16\frac{2k_BT}{m}(t-t0)^2} \tag{3.2}$$

where i refers to the x-, y- or z-direction. The expansion of a Bose-Einstein condensate is described in [52]. By introducing a scaling factor for the radial direction λ_r and for the axial direction λ_z, expressing the time in terms of $\tau = \omega_r \cdot t$ and assuming $\epsilon = \omega_r/\omega_z \ll 1$, the expansion of the BEC in first order in ϵ can be expressed as:

$$\begin{aligned} \lambda_r &= \sqrt{1+\tau^2} \\ \lambda_z &= 1 + \epsilon^2\left[\tau \arctan\tau - \ln\sqrt{1+\tau^2}\right] . \end{aligned} \tag{3.3}$$

In the far-field the expansion is linear and the density distribution is proportional to the momentum distribution. The far-field is reached for a thermal cloud if $\sigma_i(t) \gg \sigma_i(t_0)$ or for a BEC if $\lambda_r \gg 1$.

The top-mounted CCD-camera (model *Princton NTE / CCD-512-TK*) is used to observe the BEC. By different lens systems the magnification can be changed to 1×, 4× or 10×magnification. A measured resolution of 7.8μm at 10× and 12μm at 4×magnification may be reached.

3.3 Optical Lattice

Two 1D optical lattices were build up for this experiment. The first was generated by the Coherent VERDI V-10 laser system. Lattice depths on the order of $40E_{\mathrm{rec}}$ were reached. A discussion on the setup can be found in [43, 49].

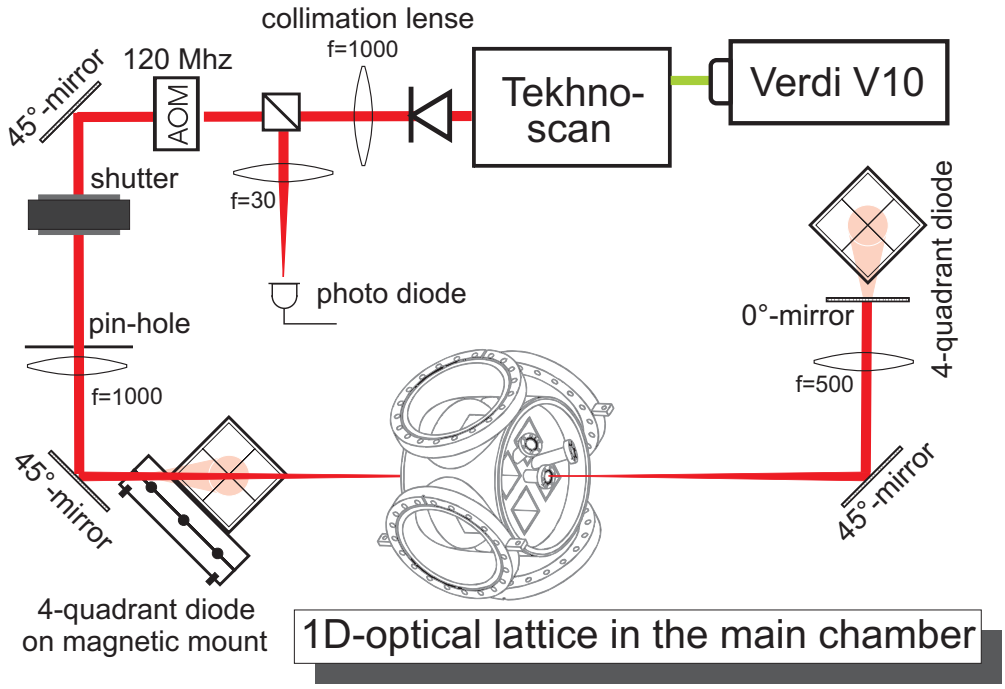

Fig. 3.6: Schematics of the optical lattice. The light produced in the Titanium-Sapphire laser is directed through an optical isolator and collimated. The optical lattice is turned on and off by an AOM and a mechanical shutter. The waist required at the position of the atoms is obtained by a 2:1 telescope. The beam is reflected and overlapped with itself to produce the optical lattice. Two 4-quadrant diodes are used to fix the position of the beam. The reflected beam is adjusted with a photo diode.

After the first lattice was disassembled a second was build up. This optical lattice is generated by the TIS-SF-07 Titanium-Sapphire laser system. The schematic of the optical path is shown in figure 3.6.

The optical lattice is turned on and off by an AOM and a mechanical shutter. With the AOM it is possible to switch the beam within less than 50ns but residual light of 0.1% can still pass. The mechanical shutter turns the beam off completely but it switches on the timescale of a few ms. A pin-hole is adjusted onto the position of the beam which is needed for fine tuning. The required waist at the position of the BEC is obtained by a 2:1 telescope with large focal lengths in order to avoid radial confinement due to dipolar forces. The focal length are $f = 1000$mm and $f = 500$mm. The lattice beam is reflected and overlapped with itself in order to produce the optical lattice.

The adjustment of the optical lattice is done by two 4-quadrant diodes and a pin-hole. The 4-quadrant diodes are used to fix the beam at a given position. The first 4-quadrant diode is placed after the first lens of the telescope. It is attached onto a magnetic mount and can be set into and removed from the beam. The second 4-quadrant diode is fixed after the 0°-mirror for the retro-reflection and is illuminated by the fraction of the beam that is transmitted through the mirror. The reflected beam is fixed by adjusting it onto a photo diode after it passed a second time through the pin-hole.

The optical lattice was designed to create extremely deep potentials with depths on the order of several hundred E_{rec}. This is needed, as will be discussed in chapter 4, to increase the density of the atomic cloud and to imprint a structure into the density distribution which is smaller than the wavelength of the light field driving the dipole-dipole interaction.

3.4 Status of the Experiment

The road-map of Bose-Einstein condensation in our Experiemt is presented in figure 3.7. The plot shows the progression of the phase space density during the different steps towards the BEC. Typically the density of the condensate is $10^{14}\mathrm{cm}^{-3}$ at an atom number of 10^5 and a temperature of 200nK.

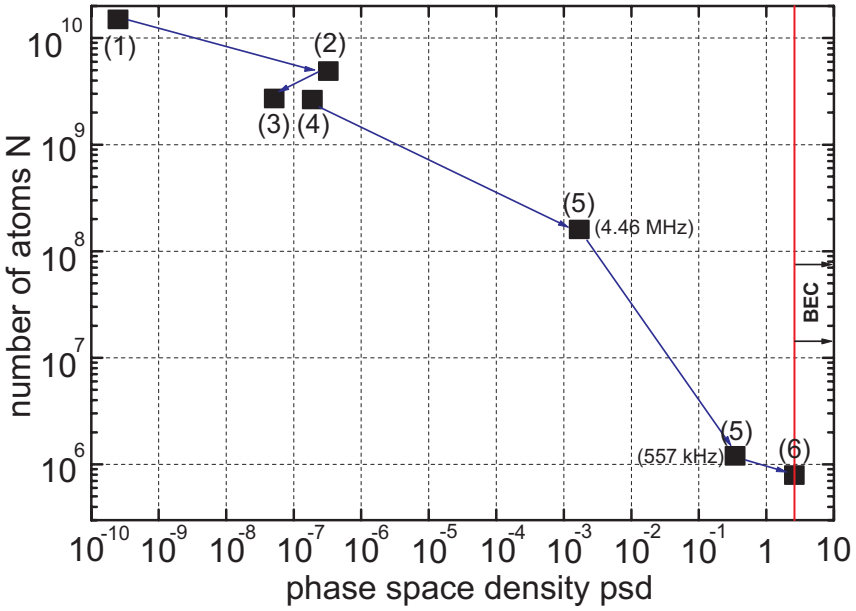

Fig. 3.7: The route to Bose-Einstein condensation. (1) elongated 3D-MOT, (2) detuned MOT, (3) loading into the magnetic trap, (4) full compressed magnetic trap, (5) evaporative cooling, (6) Bose-Einstein condensation.

Figure 3.8 shows on the left-hand side absorption images at different steps of the evaporative cooling, the thermal cloud, the BEC-transition and two images below T_C. On the right-hand side the optical density along the z-axis

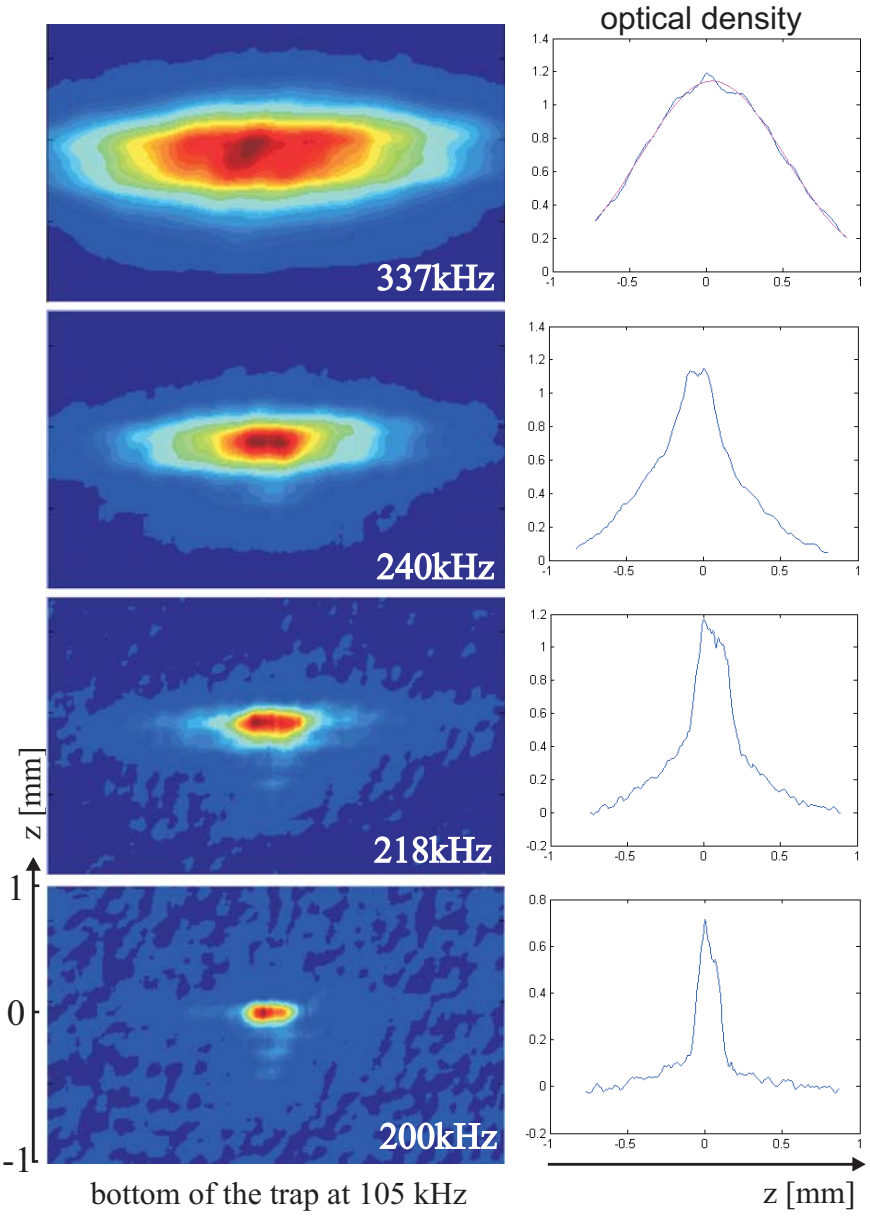

Fig. 3.8: Absorption images at different steps of the evaporative cooling (left-hand side), the thermal cloud above the critical temperature, the transition and two images below T_C. The optical density along the z-axis at $x = y = 0$ is plotted on the right-hand side. The thermal cloud has a gaussian and the condensate a parabolic profile. The parameters are $\omega_r = 2\pi \cdot 1.3\text{kHz}$, $\omega_z = 2\pi \cdot 2.7\text{Hz}$ and the bottom of the trap is at 150mG.

at $x = y = 0$ is plotted. The thermal cloud has a gaussian and the condensate a parabolic profile. The parameters are $\omega_r = 2\pi \cdot 1.3\text{kHz}$, $\omega_z = 2\pi \cdot 2.7\text{Hz}$ and the bottom of the trap is at 150mG.

After Bose-Einstein condensation was accomplished and the far blue-detuned optical lattice successfully characterized, we are currently working on the adjustment and analysis of the second lattice. First experiments with the lattice at $P = 400\text{mW}$, $\lambda_{\text{lat}} = 777\text{nm}$ and $\sigma = 300\mu\text{m}$ were already performed.

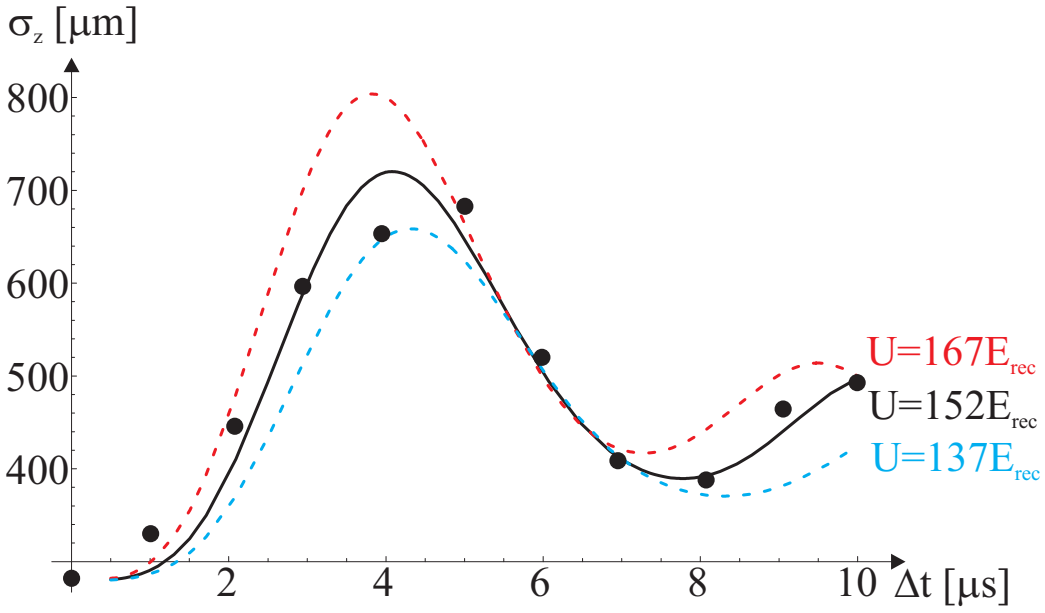

Fig. 3.9: Broadening of the cloud in the axial direction (black dots) due to the optical lattice versus the flash-time of the optical lattice. The three curves correspond to the theoretical width of the cloud for different lattice depths assuming the broadening is caused by the energy deposited in the cloud due to diffraction and distributed by collisions.

Diffraction measurements were done by switching the optical lattice on for Δt and observing the axial broadening of the cloud in time-of-flight. Due to collisions the diffraction orders couldn't be resolved and the resulting shape had a gaussian-profile. Figure 3.9 shows the measured axial width of our atomic cloud (dots) with respect to the flash-time of the optical lattice. The oscillation demonstrates that the experiment was performed in the channeling regime [53]. The black curve corresponds to the theoretical broadening of the cloud for $U_{\text{lat}} = 152E_{\text{rec}}$. The two dashed-curves correspond to the variation of the lattice depth by 10%. For the theoretical curve we assumed that the whole energy deposited in the cloud due to the diffraction results because of collisions in an effective broadening. This broadening can be described in terms of an effective temperature. This temperature is calculated by determining the fraction of atoms in the different diffraction orders and summing their energies $(n_D 2\hbar k)^2/2m$, where n_D is the diffraction order. The revival time (minimum in the broadening) is characteristic for the lattice

depth and independent of the scaling of σ_z. An additional empirical factor of 0.8 in σ_z for the broadening was taken into account which corresponds to the transfer of energy from the z- into the other directions.

Due to the revival at $\Delta t \approx 8\mu s$ the lattice depth can be estimated to $U_{\mathrm{lat}} \approx 150E_{\mathrm{rec}}$. The theoretically expected value of the optical potential of $U_{\mathrm{lat}} = 380E_{\mathrm{rec}}$ was not achieved due to imperfect adjustment of the lattice beams.

3.5 Summary

In the scope of this thesis several modifications of the experimental apparatus were made in order to allow the planned measurements. The more important modifications were:

- The laser-diodes for probing and repumping were exchanged to reach higher intensities. A new spectroscopy [54] was set up to achieve a higher stability of the frequencies.
- An existing blue detuned 1D optical lattice using a Verdi laser system at 532nm and 978W/mm^2 was optimized and characterized. The optical potentials obtained were on the scale of $36E_{\mathrm{rec}}$ and not deep enough for the planned experiments. So we decided to set up a more resonant optical lattice.
- The new 1D optical lattice at 777nm and 4.2W/mm^2 was build up, adjusted and characterized. The optical potentials already achieved on the order of $150E_{\mathrm{rec}}$ are about a factor of 2.5 lower than the theoretically expected value, but sufficiently deep to start with the planned experiments.
- The flash beam was set up making use of the MRB Titanium-Sapphire laser system. The flash can be switched by an acousto-optical modulator triggered by a function generator within 50ns on and within 100ns off.

All the components needed for the experiment are set up and operational, the experimental apparatus is ready to start with the planned measurements.

4. Numerical Calculations

In this chapter we are going to discuss the general structure and the details of the calculation of the light induced dipole-dipole interaction potentials within BECs and the resulting momentum distributions. Two different cases with resonant and far-detuned light will be presented. The general theoretical basis for the light induced dipole-dipole interaction was presented in chapter 2, the parameters and properties of the experimental setup were shown in chapter 3. The results of the calculation will be discussed in chapter 5.

4.1 Outline of the Numerical Calculation

The light induced dipole-dipole interaction is anisotropic and oscillates temporally and spatially. In the regime we are considering, it is not possible to express the induced potential analytically. Therefore, numerical calculations have to be carried out to investigate theoretically the response of the atoms to the interaction. The computational program we developed for the calculations is written in *Mathematica 4.2*. Prior to the detailed discussion of the calculations, a brief outline of the procedure is presented.

The boundary conditions for the atomic cloud we are considering are $T < 1\mu$K, radial widths of the cloud on the order of the wavelength, peak densities on the order of $\rho_0 \approx 10^{14}$ to 10^{15}cm^{-3} and mean-field energies on the order of $E_{mean}/h \approx 10$kHz. We are only considering short flash times $\Delta t \leq 1\mu$s. Hence we do not have to take any changes of the density distribution due to the interaction into account (Raman-Nath regime).

We start the calculation with the discretization of the density distribution and of the spatial part of the dipole-dipole interaction potential. For the magnitude of a single dipole moment embedded in an ensemble and for the relative phase of the dipoles to the driving field we need the spatial distribution of the intensity and the detuning of the incident light. In the case of high absorption, we also have to take the intensity of the spontaneously emitted light into account. The full interaction potential within the BEC is calculated by performing the convolution of the density distribution and the dipole-dipole interaction potential.

If the induced potential $U_{\text{liddi}} \gtrsim \hbar\delta_{\text{L}}$ we have to calculate the potential self-consistently in order to increase the accuracy as the induced potential shifts the resonance frequency of the atoms locally and with it the scattering cross section and the induced dipole moment. Selfconsistency can be achieved by

reinserting the interaction potential computed into the calculation as an additional effective detuning and repeat the procedure until the potential converges.

The final part is the calculation of the resulting momentum distribution. This is done by determining the unperturbed wavefunction and propagating it in time. Due to the induced potential a spatially varying phase is imprinted and the momentum distribution is changed. The broadening due to spontaneous emission is also taken into account.

4.1.1 Initialization

Before starting the calculations we set the values of all constants, fix the numerical parameters and the initial and boundary conditions like the properties of the incident light field, the parameters of the density distribution and the time of interaction, in order to initialize the program. The transition we are considering is the $|5^2S_{1/2}, F = 2\rangle \;\rightarrow\; |5^2S_{3/2}, F = 3\rangle$. This was chosen because laser light at the right frequency is already present at a high intensity (MOT-beams). The transition to the $F = 3$-level has the advantage that for detunings on the order of up to +100MHz the other F-levels are only slightly populated and their influence may be neglected.

Since we are using numerical methods on a discrete space we need to define a three dimensional grid, which is the discretized representation of the volume we are interested in. The physical dimension of the discretized space depends on two length-scales: the first is the size of the volume we are considering, for example a cube with a length of the edges equal to the full width of the cloud in the radial direction σ_r, the second is the length scale of the range of interaction. As the light induced dipole-dipole interaction is a long range interaction, the size of the discretized space may be found by investigating the behaviour of the induced potential for different grid sizes. The full physical dimension of the discretized space is the volume considered enlarged by the range of interaction. The volume we are considering is $4\lambda_{\mathrm{lat}}$ in the radial direction and $8\lambda_{\mathrm{lat}}$ in the axial direction. By doubling the size of the grid the change in the potential is smaller than a few percent.

The *FFT-algorithm* (*FFT*: Fast Fourier Transformation) uses grid sizes of the form $N = 2^{n_x} \times 2^{n_y} \times 2^{n_z}$. For high resolution calculations we choose the grid to be $64 \times 64 \times 128 = 524.288$ grid points and for low resolution calculations $32 \times 32 \times 64 = 65.536$ grid points. To avoid a beat between the grid spacing Δl and the optical lattice spacing $\lambda/2$ in the density distribution of the atoms, we set Δl to:

$$\Delta l = \frac{\lambda_{\mathrm{lat}}}{2j} \quad : \quad j \in \mathbb{N}\,, \tag{4.1}$$

where λ_{lat} is the wavelength of the lattice beams. For the high resolution calculations the grid spacing is $\Delta l = \lambda_{\mathrm{lat}}/16$ and for the low resolution calculations $\Delta l = \lambda_{\mathrm{lat}}/8$.

4.1.2 Reaching the Steady State

For the calculation we assume that the internal degrees of freedom of the atomic systems are in steady state. Therefore, we need to investigate on which timescale the steady state is reached in order to fix the time of interaction. The evolution of the Bloch vector can be calculated by integrating the optical Bloch equations numerically for the given parameters.

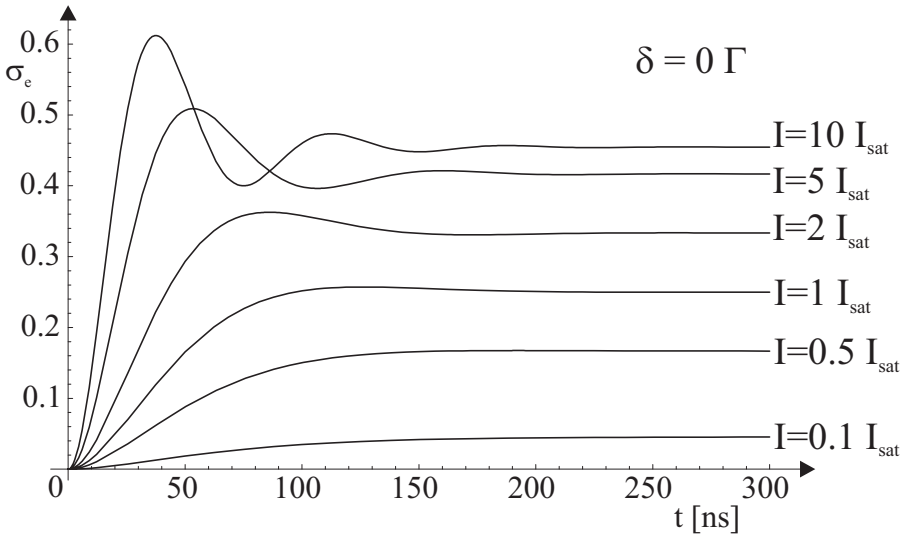

Fig. 4.1: Population of the excited state versus the time of interaction at $\delta_{\mathrm{L}} = 0$ and different incident intensities, from the numerical integration of the optical Bloch equations.

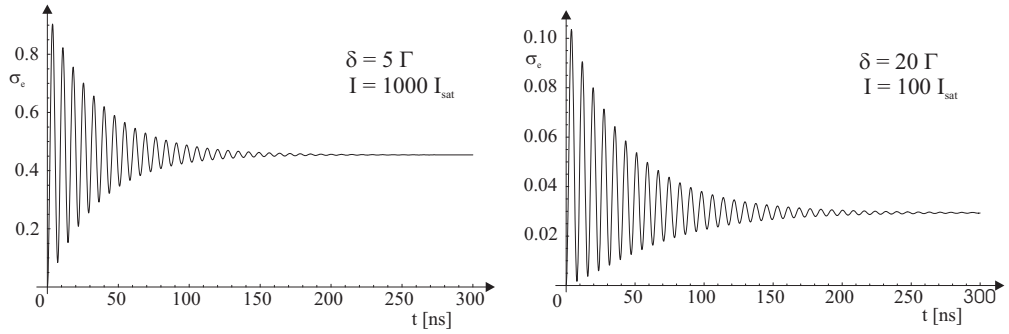

Fig. 4.2: Population of the excited state versus the time of interaction at $\delta_{\mathrm{L}} = 5\Gamma, I_0 = 1000 I_{\mathrm{sat}}$ (left-hand side) and $\delta_{\mathrm{L}} = 20\Gamma, I_0 = 100 I_{\mathrm{sat}}$ (right-hand side), from the numerical integration of the optical Bloch equations.

In figure 4.1 and 4.2 the population of the excited state of a single atom σ_e is plotted versus the time of interaction for different parameters. The initial conditions were $u(0) = v(0) = \sigma_e(0) = 0$. Figure 4.1 shows $\sigma_e(t)$ for $\delta_{\mathrm{L}} = 0$ and different incident intensities. Figure 4.2 shows $\sigma_e(t)$ for large detunings and high intensities. After 150 to 200ns, which corresponds to a few lifetimes of the excited state, the system is in steady state almost independently of the

detuning and the incident intensity. Therefore, we set the time of interaction to at least 300ns to guarantee that the system is in steady state.

4.1.3 Density Distribution

The density distribution of the BEC in our experiment is strongly anisotropic with an aspect ratio of up to 1:850. It has a cigar shape, with a radial width of a few μm and an axial width of a few 100μm as described in section 3.2. In the axial direction the Thomas-Fermi approximation is valid and the shape of the density distribution is a parabola. In the radial direction, $\hbar$ times the trapping frequency is on the order of the mean-field energy and the Thomas-Fermi approximation is not valid. The healing length is comparable to the radial width of the cloud, hence we assume a gaussian density profile like in the case of non-interaction atoms in the trap (section 2.3.2).

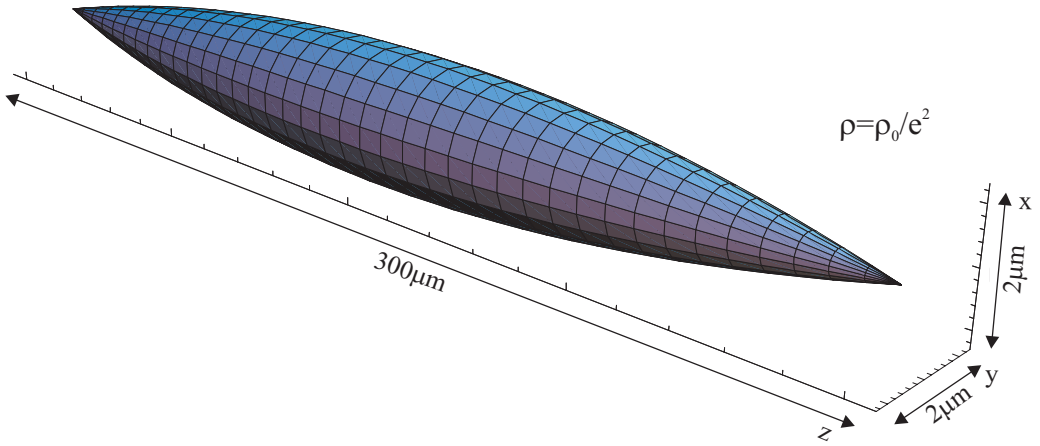

Fig. 4.3: Qualitative graph of the equidensity surface ($\rho = \rho_0/e^2$) of the BEC

The density distribution as shown in fig 4.3 is:

$$n(x,y,z) = \rho_0 \ \exp\left(-8\frac{x^2+y^2}{\sigma_r^2}\right) \cdot \frac{1}{2}\left(1 - \frac{4z^2}{\sigma_z^2} + \left|1 - \frac{4z^2}{\sigma_z^2}\right|\right) \tag{4.2}$$

$$\text{with} \quad \int n(\vec{r}) d^3r = N \ , \tag{4.3}$$

where the distribution is described by the parameters ρ_0, σ_r and σ_z. σ_r is the full width of the cloud in the radial direction, measured from ρ_0/e^2 to ρ_0/e^2 and σ_z is twice the Thomas-Fermi radius (equation 2.59). The modulus in the last term was taken in order to guarantee, that the density is zero outside the Thomas-Fermi radius.

The full density distribution of the BEC in a 1D optical lattice as shown in figure 4.4 is given by:

$$n_{\text{lat}}(x,y,z) = \rho_{\text{lat}} \ \frac{n(x,y,z)}{\rho_0} \cdot \exp\left(-8\frac{(z - \frac{\lambda_{\text{lat}}}{2} \cdot [\frac{z}{\lambda_{\text{lat}}/2}])^2}{\sigma_{\text{lat}^2}}\right) , \tag{4.4}$$

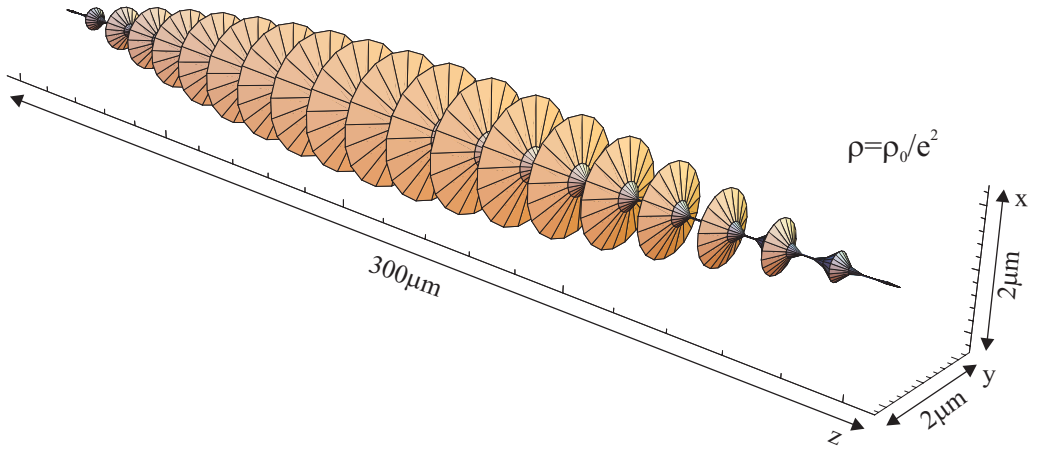

Fig. 4.4: Qualitative graph of the equidensity surface ($\rho = \rho_0/e^2$) of the BEC in the optical lattice

where ρ_{lat} is the peak density in the lattice, σ_{lat} is the width of a lattice site measured from ρ_{lat}/e^2 to ρ_{lat}/e^2 and $[X]$ is the rounded value of X. $[\frac{z}{\lambda_{\mathrm{lat}}/2}]$ is the number of the disc within the optical lattice, where the disc in the center ($z = 0$) is labelled zero.

4.1.4 Discretization

A three dimensional discretization is performed by approximating a function by mean values in a grid. The mean values are taken within unit cubes of the size Δl^3, where Δl is the separation of the grid points:

$$f_{i_1,i_2,i_3} \stackrel{!}{=} \frac{1}{\Delta l^3} \int_{(i_3-1/2)\Delta l}^{(i_3+1/2)\Delta l} \int_{(i_2-1/2)\Delta l}^{(i_2+1/2)\Delta l} \int_{(i_1-1/2)\Delta l}^{(i_1+1/2)\Delta l} f(x,y,z)dxdydz \ , \tag{4.5}$$

where $i_{1,2,3}$ are integers, $f(x,y,z)$ is an analytic function and f_{i_1,i_2,i_3} the discretized function of $f(x,y,z)$.

The discretization of the light induced dipole-dipole interaction potential by numerically integrating equation 4.5 is time-consuming. Therefore, we approximate the potential given by equation 2.41 of two interacting dipoles by:

$$\begin{aligned} V_{i_1,i_2,i_3} = \ & \tfrac{1}{20} \cdot \sum_{\text{corners}} V_{\mathrm{AB}}((i_1 \pm 1/2)\Delta l, (i_2 \pm 1/2)\Delta l, (i_3 \pm 1/2)\Delta l) \\ & + \tfrac{12}{20} \cdot V_{\mathrm{AB}}(i_1\Delta l, i_2\Delta l, i_3\Delta l) \ , \end{aligned} \tag{4.6}$$

where not only the potential at center of the unit cubes but also the magnitudes of the potential at its corners are taken into account. Effectively we are not only evaluating a single point of the potential per unit cube for the discretization but nine. We determined the weights 1/20 and 12/20 by calculating the error for different weights, different grid spacings and one thousand

randomly chosen points within the grid respectively. The error is minimal for the weights as presented above and is on the order of a few percent.

The interaction potential diverges for $\vec{r} \to \vec{0}$, hence the central grid point has to be treated separately. For two dipoles, with dipole one at $(0,0,0)$ and dipole two at (x,y,z) and both pointing into the z-direction the divergence is:

$$V_{\mathrm{AB}}(x,y,z) \to \begin{cases} +\infty & \text{, for} \quad x \to 0, y = 0, z = 0 \\ +\infty & \text{, for} \quad x = 0, y \to 0, z = 0 \\ -\infty & \text{, for} \quad x = 0, y = 0, z \to 0\ . \end{cases} \tag{4.7}$$

To fix the divergence we introduce a cutoff on the order of the s-wave scattering length[1]. For $|\vec{r}| \ll \lambda_{\mathrm{lat}}$, the interaction potential is given by the static dipole-dipole potential (section 2.2.2). The density distribution can be assumed to be isotropic as the cut off is much smaller than all length-scales involved: $|a| \ll \sigma_{\mathrm{lat}} \approx 100\mathrm{nm} \ll \sigma_r \approx 1\mu\mathrm{m}$. Due to the cutoff a spherical symmetric part is cut out of the potential. In Appendix A is shown that the static interaction potential vanishes for isotropic distributions of dipoles, therefore we may neglect the potential in the center and take only the potential at the corners of the unit cube into account:

$$V_{0,0,0} = \frac{1}{20} \cdot \sum_{\text{corners}} V_{\mathrm{AB}}(\pm\Delta l/2, \pm\Delta l/2, \pm\Delta l/2)\ . \tag{4.8}$$

For the discretization of the density distribution it is already sufficient to evaluate the value of the density at the position of the grid points:

$$n_{i_1,i_2,i_3} = n(i_1\Delta l, i_2\Delta l, i_3\Delta l)\ , \tag{4.9}$$

where n_{i_1,i_2,i_3} is the discretized density distribution. The error is $< 1\%$.

4.1.5 Electromagnetic Field Intensity and Detuning

In order to calculate the interaction potential of two dipoles, we have to calculate the spatial distribution of the dipole moments within the atomic cloud. As we discussed in section 2.1.4, by knowing the detuning and the intensity of the incident beam and the properties of the atoms (section 3.1), the expectation value of the dipole moment is given by equation 2.31.

The effective detuning of the light field can vary in space due to either a potential that shifts the ground and the excited state differently or due to potentials acting only on superpositions of the two states. The dipole-dipole interaction potential is such a potential as it only acts on atoms with induced dipole moments. During the transition the potential energy of the atom is changed and with it the energy needed to excite the atom. The effective detuning at the position $\vec{r}$ is given by:

$$\delta_{\mathrm{eff}}(\vec{r}) = \delta_L - \frac{U_{\mathrm{liddi}}(\vec{r})}{\hbar}\ . \tag{4.10}$$

[1] S-wave scattering length for $|\mathrm{F}{=}2,\mathrm{m_F}{=}{+}2\rangle$ is 109(10) $a_0 = 5.77$ nm [55]

The calculation of the intensity profile is more involved. The differential equation 4.11 describes the intensity of the coherent light along a line of absorbers. As the intensity profile is changed only in one direction, deflection, refraction and other more dimensional effects are neglected. The error made by this approximation depends strongly on the density, the detuning and the intensity and will be discussed in section 4.2.1 for typical parameters. By choosing the incident beam to propagate into the y-direction the differential equations can be written as:

$$\vec{k} = k \cdot \vec{e}_y \quad : \quad dI = -I(\vec{r})n(\vec{r})\sigma_{\text{scat}}(I(\vec{r}), \delta(\vec{r}))dy \; , \tag{4.11}$$

where $\vec{e}_y$ is the unit vector into the y-direction, I is the intensity, n the density distribution and σ_{scat} the scattering cross section as given by equation 2.36. In general there is no analytic solution for this differential equation[2]. We are interested in different regimes, for resonant incident light the absorption and the saturation are high, for far-detuned incident light the absorption is low and $s \approx 1$. Therefore we solve equation 4.11 numerically:

$$\Delta I_i = -I_{i-1} \; n_i \; \sigma_{\text{scat}}(I_{i-1}, \delta_{i-1}) \; \Delta y \; , \tag{4.12}$$

where x and z are fixed, the index i is refereing to the position in the y-direction and Δy is the step size. For higher accuracy we set the step size to $\Delta y = \Delta l/2 = \lambda_{\text{lat}}/32$. To compute the full intensity distribution within the BEC equation 4.12 is solved for every grid line along the y-direction separately.

Due to the one-dimensionality of equation 4.11 special care has to be taken when performing calculations involving BECs in optical lattices or using selfconsistent methods. In these cases unphysical structures much smaller than the wavelength emerge in the spatial distribution of the coherent light intensity.

4.1.6 Spontaneous Emissions

Spontaneous emissions create an incoherent background intensity in the BEC. If the background intensity is on the order of the coherent light intensity within the cloud we have to take the spontaneously emitted light into account, as it partially saturates the atomic transition.

In order to estimate the intensity of the background, we consider a region with homogeneous distribution of atoms and a homogeneous distribution of the incident intensity and neglect reabsorption. In steady state the power absorbed is equal to the power emitted. Therefore, we approximate the intensity of the spontaneous background at any point to be the absorbed intensity at this point. In an optically thin medium the spontaneous background decays

[2] Analytic solutions may be found in special cases, for example for low saturation $s \ll 1$ and $n = const$ the well known Beer's law.

with $1/r^2$, hence a more accurate approximation is to convolve the calculated background intensity with a normalized $1/r^2$-function. This dependance is modified due to reabsorption. In the following we are going to neglect this convolution as we are only interested in the order of magnitude of the background intensity.

By applying this approximation to our calculation and assuming the density and the intensity distribution around the grid points to be homogeneous, the background intensity at every point is approximately equal to the absorbed intensity at this grid point:

$$I_{\mathrm{sp},i} = I_{\mathrm{coh},i-1} - I_{\mathrm{coh},i} \ , \tag{4.13}$$

where I_{sp} is the intensity of the background and I_{coh} is the intensity of the coherent incident light field. This method of calculating the intensity of the spontaneous background is the first approach and neglects the contribution of the intensity emitted at all other grid points.

The local electric field is given by the sum of the electric fields, hence the local intensity I_{loc} can be expressed as:

$$I_{\mathrm{loc}} = \left(\sqrt{I_{\mathrm{coh}}} + e^{-i\phi}\sqrt{I_{\mathrm{sp}}}\right)^2 = I_{\mathrm{coh}} + I_{\mathrm{sp}} + 2\cos\phi\sqrt{I_{\mathrm{coh}} I_{\mathrm{sp}}} \ , \tag{4.14}$$

where ϕ is the relative phase of the two fields. ϕ is arbitrary and all phases have the same probability. For background intensities on the order of the incident light intensity we can estimate the amplitude of the effective dipole moment d_{eff} by inserting equation 4.14 into equation 2.31 and averaging over the phase:

$$d_{\mathrm{eff}} = \frac{1}{2\pi}\int_{-\pi}^{\pi} d_0(\phi) d\phi \tag{4.15}$$

However, no analytic solution could be found for this equation. Therefore, we approximate equation 4.14 by

$$I_{\mathrm{loc}} = \left(\sqrt{I_{\mathrm{coh}}} + \cos(\phi)\sqrt{I_{\mathrm{sp}}}\right)^2 = I_{\mathrm{coh}} + \cos^2\phi I_{\mathrm{sp}} + 2\cos\phi\sqrt{I_{\mathrm{coh}} I_{\mathrm{sp}}} \ , \tag{4.16}$$

The error made due to this approximation is up to 15% for $I_{\mathrm{coh}} = I_{\mathrm{sp}}$. The analytic solution of equation 4.16 is given by:

$$d_{\mathrm{eff}} = \sqrt{\tfrac{3\Gamma^3\varepsilon_0 hc^3}{\omega_0^3}}\ \mathrm{Re}\frac{\left[S^+\left(\log - \frac{\sqrt{S_{\mathrm{sp}}}}{S^-} - \log\frac{\sqrt{S_{\mathrm{sp}}}}{S^-}\right) + S^-\left(\log - \frac{\sqrt{S_{\mathrm{sp}}}}{S^+} - \log\frac{\sqrt{S_{\mathrm{sp}}}}{S^+}\right)\right]}{S^-\ S^+}$$

$$\text{with} \quad S^{\pm} = \sqrt{1 \pm 2\imath\sqrt{S_{coh}} - S_{coh} + S_{sp}} \ ,$$

$$S_{\mathrm{coh}} = \tfrac{\Gamma^2}{(\Gamma^2+4\delta_L^2)}\ \tfrac{I_{\mathrm{coh}}}{I_{\mathrm{sat}}} \quad , \quad S_{\mathrm{sp}} = \tfrac{\Gamma^2}{(\Gamma^2+4\delta_L^2)}\ \tfrac{I_{\mathrm{sp}}}{I_{\mathrm{sat}}} \ . \tag{4.17}$$

The derivation of equation 4.17 is shown in Appendix C. The results of this approximation are shown in section 4.2.1 and section 4.2.2 for typical parameters.

4.1.7 Phase Shift of the Dipole Moment

The relative phase of two oscillating dipoles can change the magnitude and the sign of the interaction, as the interaction potential is scaled by the scalar product of the two dipoles:

$$V_{\mathrm{AB}}(\vec{s}) \;\rightarrow\; [\vec{d}_{\mathrm{A}} \cdot \vec{d}_{\mathrm{B}}]\tilde{V}_{\mathrm{AB}}(\vec{s}) \;=\; [d_{\mathrm{A}}(\vec{r})d_{\mathrm{B}}(\vec{r}_0)\cos(\vec{k}\cdot\vec{s}+\Delta\phi)]\tilde{V}_{\mathrm{AB}}(\vec{s}) \;, \quad (4.18)$$

where $\vec{s} = \vec{r} - \vec{r}_0$, $\Delta\phi$ is the relative phase and $\tilde{V}_{\mathrm{AB}}$ is the spatial part of the light induced dipole-dipole interaction potential.

The $\cos(\vec{k}\cdot\vec{s})$ term corresponds to the spatial dependence of the phase of the driving field. If the effective detuning varies in space, the relative phase of the dipoles will be affected. The relative phase ϕ' of a dipole to the driving field expressed in terms of δ_{L} and I_0 in steady state is given by (from equation 2.28):

$$\phi'(\vec{r}) = \arctan(-v(\vec{r})/u(\vec{r}_0)) = \arctan\left(-\frac{\Gamma}{2\delta_{\mathrm{L}}(\vec{r})}\right) . \quad (4.19)$$

Analytically for $\delta_{\mathrm{L}} \rightarrow 0 \;:\; \phi \rightarrow \pi/2$ but numerically we can not handle $1/0$ infinities. As we are only interested in the relative phase of the dipoles, we shift all phases by $\pi/2$:

$$\phi(\vec{r}) = \arctan\left(\frac{2\delta_{\mathrm{L}}(\vec{r})}{\Gamma}\right) . \quad (4.20)$$

The relative phase of the dipoles $\Delta\phi$ is:

$$\Delta\phi(\vec{r},\vec{r}_0) = \phi'_{\mathrm{A}}(\vec{r}) - \phi'_{\mathrm{B}}(\vec{r}_0) = \phi_{\mathrm{A}}(\vec{r}) - \phi_{\mathrm{B}}(\vec{r}_0) \;, \quad (4.21)$$

where ϕ_{A} is the relative phase of dipole A and ϕ_{B} the relative phase of dipole B to the driving field shifted by $\pi/2$.

4.1.8 Full Interaction Potential

Due to the spatial dependance of the dipole moments and the phase shift, the convolution of the interaction potential and the density distribution (equation 2.43) becomes the integral:

$$U_{\mathrm{liddi}}(\vec{r}_0) = \int_{-\infty}^{\infty} V_{\mathrm{AB}}(\vec{r}_0,\vec{r})n(\vec{r})d^3r \;, \quad (4.22)$$

where V_{AB} not only depends on $\vec{s} = \vec{r} - \vec{r}_0$ but on $\vec{r}_0$ and $\vec{r}$ separately.

It is only possible to integrate two functions f, g by the method described in Appendix B, if the integral can be expressed as a convolution:

$$\int_{-\infty}^{\infty} f(\vec{r},\vec{r}_0)g(\vec{r},\vec{r}_0)d^3r \quad\rightarrow\quad h'(\vec{r}_0)\int_{-\infty}^{\infty} f'(\vec{s})g'(\vec{r})d^3r \quad (4.23)$$

where f', g', h' are some new functions depending only on $\vec{r}, \vec{r}_0$ and $\vec{s}$ respectively. Therefore, we separate the terms of the interaction potential:

$$\begin{aligned} U_{\text{liddi}}(\vec{r}_0) &= \int_{-\infty}^{\infty} V_{\text{AB}}(\vec{r}_0, \vec{r}) n(\vec{r}) d^3r \\ &= \int_{-\infty}^{\infty} d_{\text{A}}(\vec{r}) d_{\text{B}}(\vec{r}_0) \cos(\vec{k} \cdot \vec{s} + \Delta\phi) \tilde{V}_{\text{AB}}(\vec{s}) n(\vec{r}) d^3r \ . \end{aligned} \quad (4.24)$$

In order to detach all terms, the phase has to be expanded:

$$\begin{aligned} \cos(\vec{k} \cdot \vec{s} + \phi_{\text{A}}(\vec{r}) - \phi_{\text{B}}(\vec{r}_0)) = &\ \cos(\vec{k} \cdot \vec{s}) \cdot \cos\phi_{\text{A}}(\vec{r}) \cdot \cos\phi_{\text{B}}(\vec{r}_0) \\ + &\ \cos(\vec{k} \cdot \vec{s}) \cdot \sin\phi_{\text{A}}(\vec{r}) \cdot \sin\phi_{\text{B}}(\vec{r}_0) \\ - &\ \sin(\vec{k} \cdot \vec{s}) \cdot \sin\phi_{\text{A}}(\vec{r}) \cdot \cos\phi_{\text{B}}(\vec{r}_0) \\ + &\ \sin(\vec{k} \cdot \vec{s}) \cdot \cos\phi_{\text{A}}(\vec{r}) \cdot \sin\phi_{\text{B}}(\vec{r}_0) \quad .(4.25) \end{aligned}$$

In order to calculate the full induced potential and take the phase shift of the dipoles into account we insert equation 4.25 into equation 4.24 and have to evaluate four convolutions instead of only one as there are four independent terms. The first term is rewritten as:

$$\begin{aligned} &\int_{-\infty}^{\infty} d_{\text{A}}(\vec{r}) d_{\text{B}}(\vec{r}_0) \cdot \cos(\vec{k}_{\text{lat}} \cdot \vec{s}) \cdot \cos\phi_{\text{A}}(\vec{r}) \cdot \cos\phi_{\text{B}}(\vec{r}_0) \cdot \tilde{V}_{\text{AB}}(\vec{s}) n(\vec{r}) d^3r \\ = &\ \left(d_{\text{B}}(\vec{r}_0) \cos\phi_{\text{B}}(\vec{r}_0) \right) \int_{-\infty}^{\infty} \left(\cos(\vec{k}_{\text{lat}} \cdot \vec{s}) \tilde{V}_{\text{AB}}(\vec{s}) \right) \left(d_{\text{A}}(\vec{r}) \cos\phi_{\text{A}}(\vec{r}) n(\vec{r}) \right) d^3r \\ = &\ h'(\vec{r}_0) \int_{-\infty}^{\infty} f'(\vec{r} - \vec{r}_0) g'(\vec{r}) d^3r \ , \end{aligned} \quad (4.26)$$

the other three terms can be rewritten in the same way. The full interaction potential of the light induced dipoles in the BEC can be computed by evaluating equation 4.26 and the other three integrals using the method described in Appendix B.

4.1.9 Selfconsistency

If $U_{\text{liddi}} \gtrsim \hbar\delta_{\text{L}}$, the calculation has to be done selfconsistently. The induced potential changes the resonance frequency of the atomic transition and can be treated as an effective detuning. Due to the change of the detuning the dipole moment distribution is altered and with it the induced potential itself. The new potential corresponds to a new effective detuning. Hence, we have to take the effective detuning into account and repeat the calculation until the potential converges. If the potential reproduces itself, it is called *selfconsistent*. The effective detuning is given by equation 4.10.

4.1.10 Momentum Distribution and Broadening

During the interaction of the dipoles the induced potential acts onto the atoms and the momentum distribution is changed. Information about the interaction potential can be extracted from the analysis of the momentum distribution and to suggest a promising set of parameters for the experiment, we calculate the evolution of the momentum distribution during the interaction. The optical lattice is present for the time the interaction is induced and the atoms stay confined in the axial direction. Therefore, we will restrict the calculations to the xy-plane at $z = 0$ which is a radial cut though the center of a disk within the density distribution and ignore all effects in the axial direction.

We will calculate the momentum distribution by propagating the unperturbed spatial wavefunction in time. We are assuming that the experiment is performed in the Raman-Nath regime[3] and the unperturbed density distribution is preserved. The effect of the interaction potential on the wavefunction is the imprint of a spatially varying phase. The momentum distribution is calculated by Fourier-transforming the propagated wavefunction and taking the modulus squared.

During the interaction a number of photons per atom n_{ph} is absorbed and the mean momentum $\bar{p}$ of the cloud changed from zero to $\bar{p} = n_{\mathrm{ph}}\,\hbar k$. For our calculations we will consider the momentum distribution of the atoms in the center-of-mass frame.

In order to calculate the momentum distribution, we need the unperturbed wavefunction $\Phi_0(\vec{r})$ of the atoms in the trap. The initial probability wavefunction in our harmonic trap can be expressed in terms of the density distribution:

$$\Phi_0(\vec{r}) = e^{i\phi_0(t)}\sqrt{n_0(\vec{r})}\ . \tag{4.27}$$

where n_0 is the unperturbed density distribution and $\phi_0(t)$ a global phase factor. This phase factor may be different for all atoms. Fluctuations of the phase are neglected. As this global phase factor can be pulled out of an integral over spatial coordinates and we are only considering the modulus squared of the wavefunction, we are going to neglect $e^{i\phi_0(t)}$.

If the interaction is turned on at $t = t_0$, the wavefunction is propagated in time by:

$$\Phi(\vec{r}, t) = \hat{U}(\vec{r}, t - t_0)\Phi(\vec{r}, t_0)\ , \tag{4.28}$$

where $\hat{U}(\vec{r}, t - t_0)$ is the time evolution operator:

$$\hat{U}(\vec{r}, t - t_0) = \exp\left(\frac{-i\hat{H}(\vec{r})(t - t_0)}{\hbar}\right)\ , \tag{4.29}$$

[3] Raman-Nath regime in this context means that the atoms are not moving significantly on the smallest scale of the system (axial width of a disc $\sigma_z/2$) during the interaction. This is valid if $T \ll \frac{m(\sigma_z/2)^2}{k_B\,\Delta t^2} \approx 120\mu\mathrm{K}$ for $\Delta t = 500\mathrm{ns}$. The temperature of the BEC is increased during the interaction by up to $20\mu\mathrm{K}$.

with $\hat{H} = \hat{H}_{\text{kin}} + \hat{H}_{\text{trap}} + \hat{H}_{\text{lat}} + \hat{H}_{\text{mean}} + \hat{H}_{\text{int}}$ is the full Hamilton operator of the system. The energy of the system consists of five independent terms, the kinetic energy of the atoms E_{kin}, their potential energy in the trap E_{trap}, their potential energy in the optical lattice E_{lat}, the mean-field energy E_{mean} and the dipole-dipole interaction energy E_{int}.

E_{kin}/h is on the order a few 10kHz after the interaction, E_{trap}/h is on the order of a few kHz, E_{lat}/h is on the order of 100kHz, E_{mean}/h is on the order of 30kHz and E_{int}/h is on the order of 10MHz. Therefore, we take only the interaction energy into account as it is one to two orders of magnitude larger than all other energies involved[4]:

$$\Phi(\vec{r}, t) = \exp\left(\frac{-iU_{\text{liddi}}(\vec{r})\,\Delta t}{\hbar}\right)\Phi(\vec{r}, t_0)\ , \tag{4.30}$$

where $\Delta t = t - t_0$.

The momentum distribution of the atoms $\tilde{n}(\vec{k}, t)$ after the interaction is given by the Fourier transformation of the in time propagated wavefunction:

$$\begin{aligned}\tilde{n}(\vec{k}, t) &= \left|\tfrac{1}{\sqrt{2\pi}^3}\int_{-\infty}^{\infty} e^{(-i\vec{k}\cdot\vec{r})}\Phi(\vec{r}, t)d^3r\right|^2 \\ &= \left|\tfrac{1}{\sqrt{2\pi}^3}\int_{-\infty}^{\infty} e^{(-i\vec{k}\cdot\vec{r})}\exp\left(\tfrac{-iU_{\text{liddi}}(\vec{r})\Delta t}{\hbar}\right)\sqrt{n(\vec{r}, t_0)}d^3r\right|^2 .\end{aligned} \tag{4.31}$$

During the interaction, the momentum distribution is broadened by spontaneous emissions [56, 57]. We assume that the broadening is isotropic as there are different transitions allowed in our experiment: The quantization axis due to the magnetic trap points into the z-direction and the transition is $5S_{1/2} \rightarrow 5P_{3/2}$. If the incident light field is polarized in the z-direction the atoms are excited $F = 2, m_F = 2 \rightarrow F = 3, m_F = 2$. If the polarization is in the x-direction the atoms are excited $F = 2, m_F = 2 \rightarrow F = 3, m_F = 1$ or $F = 2, m_F = 2 \rightarrow F = 3, m_F = 3$. The deexcitation may take place to all allowed m_F-levels. The different transitions have different probabilities and different emission patterns, hence to a good approximation the broadening is considered to be isotropic.

The momentum of a single atom after the emission of a photon is changed by $\hbar|\vec{k}|$. For isotropic broadening in three dimensions the probability of the emission is equal for all directions. We describe the change of momentum in the frame in which the atom was at rest before the emission took place. The projection of the probability of the momentum transfer into the x-direction for a single emission is given by:

$$p_1(k_x) = \begin{cases}(2\hbar|\vec{k}|)^{-1} & |k_x| \leq |\vec{k}| \\ 0 & |k_x| > |\vec{k}|\end{cases}\ , \tag{4.32}$$

where k_x is the momentum transfered into the x-direction.

[4] Note that $\text{Im}(U_{\text{liddi}}) = 0 \rightarrow |\Phi(\vec{r}, t_0)|^2 = |\Phi(\vec{r}, t)|^2$, the density distribution is not changed during the interaction.

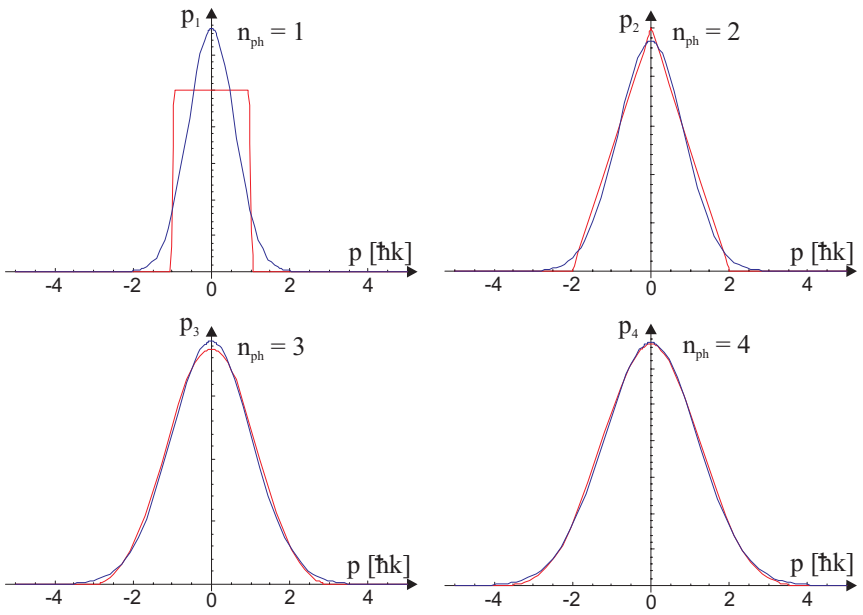

Fig. 4.5: Qualitative graph of the broadening of the momentum distribution due to 1,2,3 and 4 spontaneously emitted photons. The red curves correspond to the momentum distribution in $\hbar k$ in the frame of reference of the atom and the blue curves are gaussian fits.

The red curves in figure 4.5 show the relative probability of momentum transfer after n_{ph} emissions. The blue curves are gaussian fits. The gaussian approximation is already very good for only a few spontaneous emissions, for $n_{\mathrm{ph}} = 4$ the standard deviation is $< 0.3\%$. Therefore the broadening will be described in terms of a convolution of the original momentum distribution and a two dimensional gaussian function:

$$\tilde{n}_{\mathrm{eff}}(k_{0x}, k_{0y}, n_{\mathrm{ph}}) = \int_{-\infty}^{\infty} \tilde{n}(k_x, k_y)\, \tilde{B}(k_{0x} - k_x, k_{0y} - k_y, n_{\mathrm{ph}}) dk_x dk_y \ , \quad (4.33)$$

where $\tilde{B}$ is the broadening of a single atom in momentum space, given by equation 4.34. As a convolution in real space can be calculated as a product in momentum space (Appendix B), a convolution in momentum space can be carried out as a product in real space. Therefore, we Fourier-transform the momentum distribution, which is done numerically, and the broadening function, which is done analytically:

$$\tilde{B}(k_{0x}, k_{0y}, n_{\mathrm{ph}}) = \frac{\sqrt{2}}{n_{\mathrm{ph}}\, k_{\mathrm{ph}}^2 \pi} \exp\left(-\frac{\sqrt{2}\, ((k_{0x}-k_x)^2 + (k_{0y}-k_y)^2)}{n_{\mathrm{ph}}\, k_{\mathrm{ph}}^2} \right) \quad (4.34)$$

$$\Rightarrow B(x, y, n_{\mathrm{ph}}) = \frac{n_{\mathrm{ph}}\, k_{\mathrm{ph}}^2}{4\pi\sqrt{2}} \exp\left(-\frac{n_{\mathrm{ph}}\, k_{\mathrm{ph}}^2 (x^2+y^2)}{4\sqrt{2}} \right) , \quad (4.35)$$

where k_{ph} is the wavevector of the emitted photon. The broadened momentum distribution is calculated by multiplying the numerically transformed unbroadened momentum distribution by $B(x, y, n_{\mathrm{ph}})$ in real space and transforming back into momentum space.

The results of the measurement are projections of the momentum distribution onto the x- or onto the y-axis. Therefore, the results are integrated momentum distributions $\tilde{n}'$ in the xy-plane along the direction of observation:

$$\tilde{n}'(x) = \int_{-\infty}^{\infty} \tilde{n}(x,y)dy \quad \Rightarrow \quad \tilde{n}'_i = \sum_{j=-N_y/2}^{N_y/2} \tilde{n}_{i,j} \tag{4.36}$$

$$\tilde{n}'(y) = \int_{-\infty}^{\infty} \tilde{n}(x,y)dx \quad \Rightarrow \quad \tilde{n}'_j = \sum_{i=-N_x/2}^{N_x/2} \tilde{n}_{i,j} \quad , \tag{4.37}$$

where $\tilde{n}_{i,j}$ is the discretized momentum distribution and N_x, N_y the number of grid points in the x- and y-direction.

4.2 Calculations for Possible Realizations of the Experiments

In this section we are going to discuss two approaches for possible realizations of the measurement. The two cases we are interested in are:

- resonant flash beams : $|\delta_\mathrm{L}| < \Gamma/2$
- far-detuned flash beams : $|\delta_\mathrm{L}| > 10\Gamma$

We refer to the incident light beam as the *flash beam*, as it is turned on for short times only. To induce the largest possible dipole moments we have to adjust the detuning and the intensity with respect to equation 2.32.

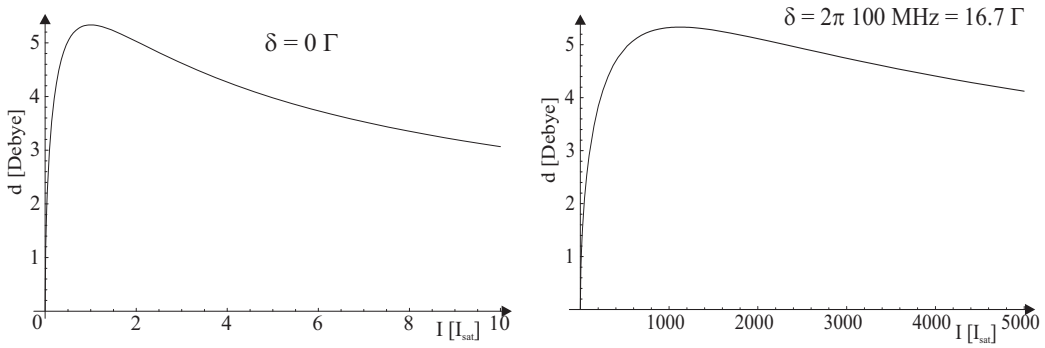

Fig. 4.6: Amplitude of the steady state expectation value of the dipole moment versus the incident intensity. Left-hand side: $\delta_\mathrm{L} = 0\Gamma$, right-hand side: $\delta_\mathrm{L} = 2\pi \cdot 100$ MHz.

The left-hand side of figure 4.6 shows the dependence of the amplitude of the dipole moment on the incident intensity for $\delta_\mathrm{L} = 0$. The maximum is exactly at $I = I_\mathrm{sat}$. On the right-hand side the amplitude of the expectation value of the dipole moment for $\delta_L = 2\pi$ 100MHz $= 16.7\Gamma$ is plotted. The maximum is at $I = 1120 I_\mathrm{sat}$. To reach at least 90% of the highest possible

dipole moment, for $\delta_{\mathrm{L}} = 0\,,\ 0.4I_{\mathrm{sat}} \geq I_0 \geq 2.5I_{\mathrm{sat}}$ and for $\delta_{\mathrm{L}} = 2\pi\,100\mathrm{MHz}$, $440I_{\mathrm{sat}} \geq I_0 \geq 2850I_{\mathrm{sat}}$.

The separation of the different F-levels in Rubidium, as shown in section 3.1, are in the far-detuned case on the order of the detuning, and the two-level approximation is only valid, if the flash light is blue detuned. The influence of the next F-level on the dipole moment and the scattering rate is on the order of a few percent up to ten percent.

4.2.1 Resonant Flash

In this section we present typical intermediate results of the calculations in the case of resonant flash beams and discuss the problems encountered. We consider the density distribution of a BEC without an optical lattice. The parameters of the calculation are:

BEC	Flash Beam
$\sigma_r = 2\mu\mathrm{m}$	$\delta_{\mathrm{L}} = 0$
$\sigma_z = 7\mu\mathrm{m}$	$I_0 = 10\ I_{\mathrm{sat}}$
$\rho_0 = 2 \cdot 10^{14}\mathrm{cm}^{-3}$	z-polarized
	$\vec{k} = k\,\vec{e}_y$

The small axial size of the BEC, which is untypical and hardly producible within our experimental setup was chosen in order to exclude numerical artifacts for selfconsistent calculations arising from density distributions which are larger than the field of view. We further assume that the incident intensity is homogeneous in the region of interest and set it to be higher than I_{sat} in order to reach further into the cloud. σ_r and σ_z are referring to the full width of the cloud in the radial and the axial direction as described in section 4.1.3 and ρ_0 is the peak density of the BEC.

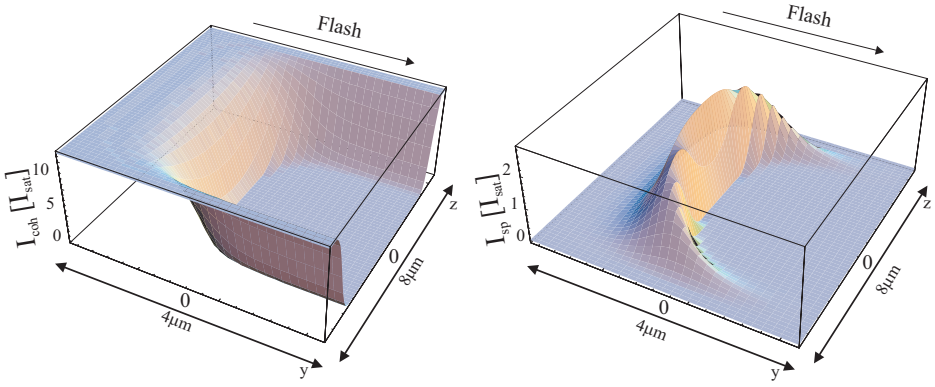

Fig. 4.7: Intensity profile for $\delta_{\mathrm{L}} = 0$ and $I_0 = 10I_{\mathrm{sat}}$ with $\vec{k} = k\,\vec{e}_y$ within the BEC in the yz-plane at $x = 0$. Left-hand side: intensity of the flash beam, right-hand side: intensity of the spontaneous background.

The first quantity calculated is the absorption within the cloud. Figure 4.7 shows on the left-hand side the intensity profile in the yz-plane. Almost no

coherent light reaches the middle of the cloud, but to induce high interaction potentials it is essential to induce large dipole moments in the center of the BEC, where the density is high. As shown in figure 4.6 (left-hand side), the dipole moment is large if the local intensity is on the order of I_{sat}. Due to saturation $35I_{\mathrm{sat}}$ are absorbed in the first half of the BEC. Hence, the intensity of the coherent light field has to be about $36I_{\mathrm{sat}}$ that $1I_{\mathrm{sat}}$ reaches the center. A 3% change in initial value of I_0 leads to a change of 100% in the intensity in the center. We have to know the optical thickness of the cloud precisely to be able to tune the incident intensity to an appropriate value.

In the case of optically thick media and high absorption the Bloch equations are not valid, the *coupled Maxwell-Bloch equations* [31,58–60] should be used instead of the Bloch equations to approximate the system. The Maxwell-Bloch equations describe the quantum mechanical state of many atoms interacting with a classical electromagnetic field. From here on the results of the calculation have to be considered carefully as they are only giving the order of magnitude of the expected effects. However, to get a general idea of the structure of the calculation and the order of magnitude for the quantities we are interested in, we are continuing the calculation.

The intensity of the incoherent background is shown on the right hand side in figure 4.7. It is of the order of the local coherent intensity I_{coh} at the center. For low background intensities compared to I_{coh} the approximations we made in section 4.1.6 in order to derive the effective dipole moment are valid. For high background intensities we also have to take the inhomogeneity of the absorption profile and reabsorption into account. The change of the local intensity corresponds to the modification of the scattering cross section. Hence, to estimate the background intensity a selfconsistent method has to be used.

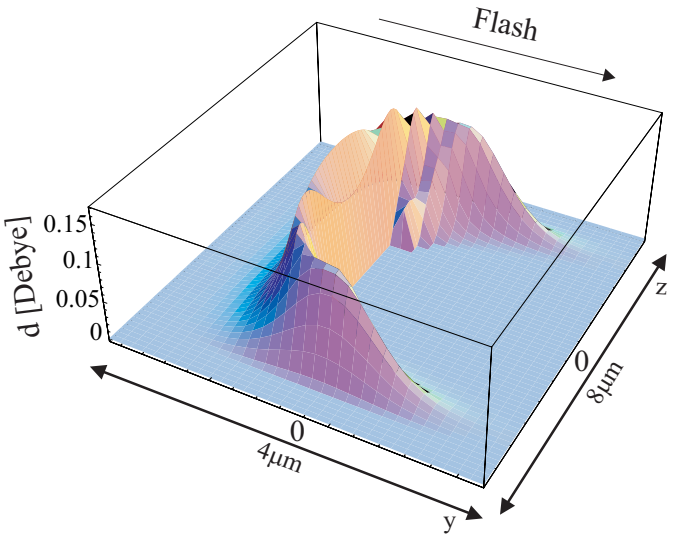

Fig. 4.8: Cut through the distribution of the dipole moments at $x = 0$ in the yz-plane. $\delta_{\mathrm{L}} = 0$, $I_0 = 5I_{\mathrm{sat}}$

The distribution of the induced dipole moments is shown in figure 4.8. The

shape of the distribution is similar to the shape of the background intensity as the induced dipole moments and the intensity of the background are connected to the absorption. The maximum of the induced dipole moment per grid point is about 0.15 Debye (number of atoms per grid point: $\rho_0 \Delta l^3 \approx 0.1$).

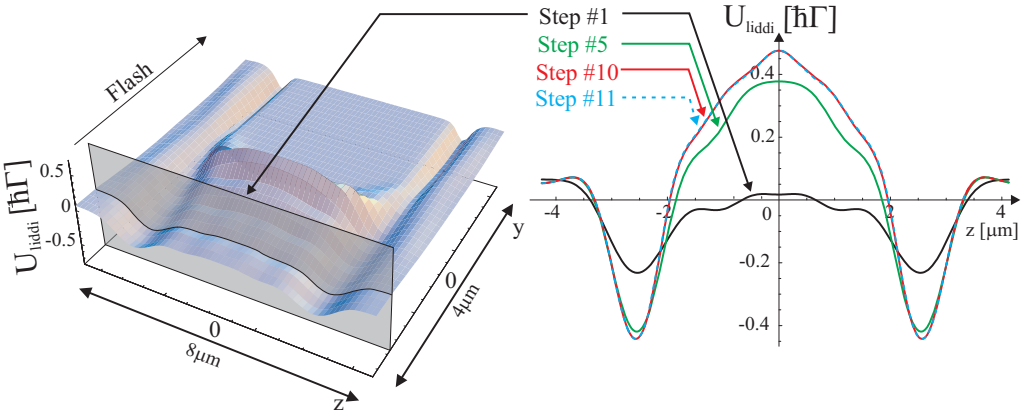

Fig. 4.9: Different stages of the selfconsistent calculation of the induced interaction potential for $\delta_\mathrm{L} = 0$, $I_0 = 10 I_\mathrm{sat}$ and $\rho_0 = 2{\cdot}10^{14}$ cm^{-3}. The calculation converges after 10 iterations to an accuracy of 1.5%. Cut through the unperturbed potential at $x = 0$ in the yz-plane left-hand side) and potential along z at $x = 0$, $y = 532$nm.

A cut at $x = 0$ through the resulting potential in the yz-plane is shown on the left hand side of figure 4.9. As discussed in section 4.1.5 the potential changes the effective detuning and with it the induced dipole moments. Therefore, the calculation is performed selfconsistently. The detuning due to the potential for this parameters is of the order of $\pm 0.5\Gamma$. As figure 4.9 shows on the right hand side, the potential converges after ten iterations to the accuracy of 1.5%, which is the mean variance of the potential at a grid point from step to step.

By using different parameters, the depth of the potential can be increased significantly. If the peak density is increased to $\rho_0 = 6 \cdot 10^{14}\mathrm{cm}^{-3}$ and the incident intensity to $I_0 = 20 I_\mathrm{sat}$ the magnitude of the potential changes to $\pm 2\Gamma$. The convergence of the selfconsistent calculation takes longer, after the fortieth step there are still fluctuations in the center of the potential on the order of 10%.

The index of refraction for $\delta_\mathrm{L} = 0$ $n_\mathrm{ref} = 1$, but for $|\delta_L| \leq \frac{\Gamma}{\sqrt{2}}$ at $I = I_\mathrm{sat}$ it varies over a range of $n_\mathrm{ref} = 0.36 - 1.64$ and the focal length of a cylindrical lens with $d = 2\mu$m is $f = -0.3\mu\mathrm{m} - 1.28\mu\mathrm{m}$. The error due to the negligence of refraction is high as the local intensity is changed significantly.

The induced potential is sensitive to fluctuations of the initial conditions, noise is amplified and fluctuations in the density may result in different shapes and magnitudes of the induced potential. We performed several computations for different grid sizes and parameters and found that the instability is not a result of the numerical calculation but of the system itself, therefore, the

experimental setup has to be more stable and better controllable in the case of resonant light than for experiments with far-detuned light.

As the calculation in the case of resonant light is inaccurate and time-consuming resonant light is not suitable for precision measurements. These problems don't appear in the case of far-detuned flashes and the precision of the expected results can be increased significantly.

4.2.2 Far-Detuned Flash Beam

In this section we present typical intermediate results of the calculation in the case of far-detuned flash beams. We consider the density distribution of a BEC within a 1D optical lattice. The parameters of the calculation are:

BEC	Lattice	Flash Beam
$\sigma_r = 1.4\mu$m	$U_{\text{lat}} = 240 E_{\text{rec}}$	$\delta_{\text{L}} = 2\pi$ 100MHz
$\sigma_z = 300\mu$m	$\sigma_{\text{lat}} = 110$nm	$I_0 = 1120 I_{\text{sat}}$
$\rho_0 = 10^{14}\text{cm}^{-3}$	$\rho_{\text{lat}} = 5.9 \cdot 10^{14}\text{cm}^{-3}$	z-polarized
	$\vec{k}_{\text{lat}} = k_{\text{lat}}\,\vec{e}_z$	$\vec{k} = k\,\vec{e}_y$

where E_{rec} is the recoil energy (equation 2.61) and the density distribution is given by equation 4.4. We consider the incident intensity to be homogeneous in the region. The index of refraction is $n_{\text{ref}} = 1.03$ and the focal length of a cylindrical lens with $d = 1.4\mu$m is $f = 12\mu$m. Therefore, refraction may be neglected without changing the results significantly.

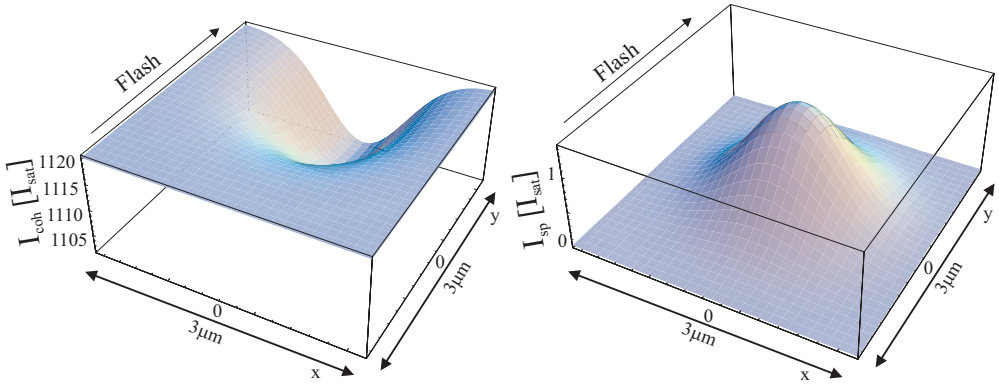

Fig. 4.10: Cut through the intensity profile at $z = 0$ in the xy-plane (left:incident flash beam, right:background) at $\delta_{\text{L}} = 2\pi$ 100MHz detuning

In figure 4.10 on the left-hand side a cut through the intensity distribution of the flash beam at $z = 0$ in the xy-plane is plotted. The maximum of the absorption is about 1.6%, the BEC is optically thin. The intensity of the background is shown on the righthand side in figure 4.10. It is only 0.1% of the coherent intensity and can be neglected.

The distribution of the dipole moment as shown in 4.11 on the left-hand side corresponds directly to the density distribution as the driving intensity is

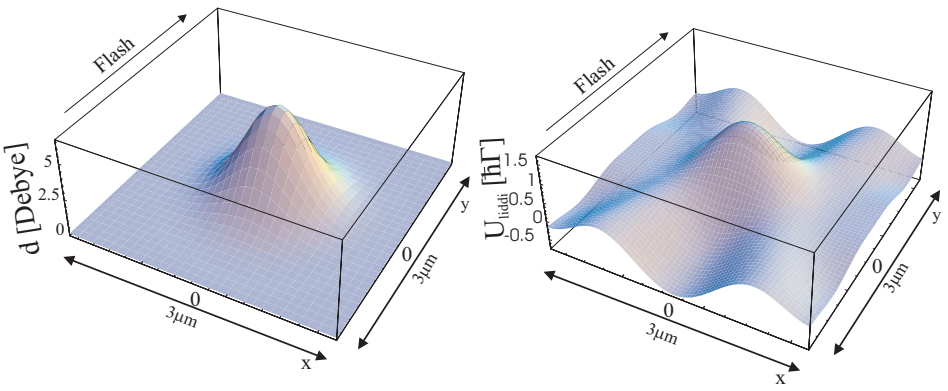

Fig. 4.11: Left-hand side: cut through the distribution of the dipole moments weighted by the normalized density distribution at $x = 0$ in the yz-plane in the case of 2π 100MHz detuning. Right-hand side: cut through the induced potential at $z = 0$ in the xy-plane at 2π 100MHz detuning

almost homogeneous in the region. The resulting potential shown in figure 4.11 on the right-hand side is on the same order of magnitude as in the resonant case. Due to the potential the detuning is changed by about 10% and the effective dipole moment by about 0.4%, hence no selfconsistency is needed.

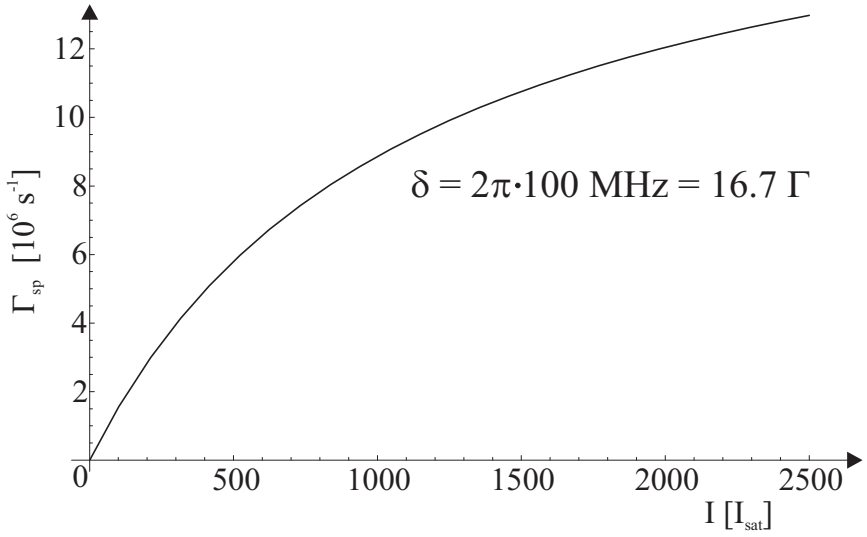

Fig. 4.12: Rate of spontaneous emissions per atom versus the intensity of the $\delta_{\mathrm{L}} = 2\pi \cdot 100$MHz detuned flash beam

For the calculation of the broadened momentum distribution the number of scattered photons is required. Due to the discussion in section 4.1.2 the time of interaction is set to $\Delta t = 500ns$. As shown in figure 4.12 the scattering rate is on the order of 10^7 photons per second per atom, hence during the interaction in average 5 photons are scattered per atom.

The momentum distribution without and with broadening due to sponta-

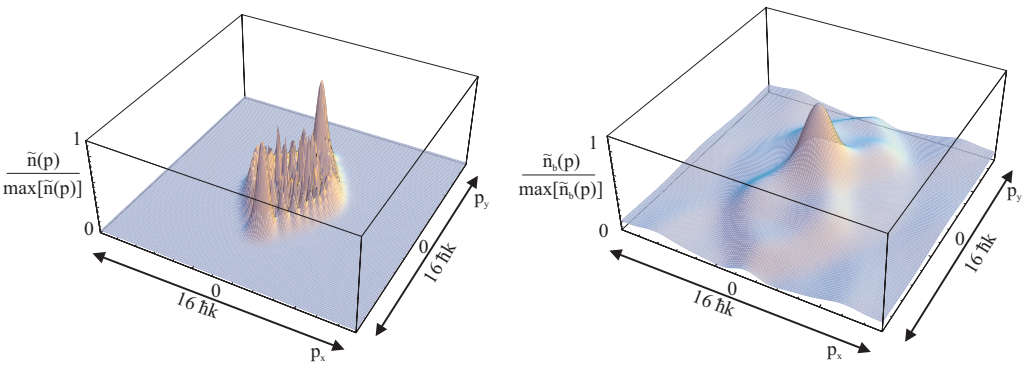

Fig. 4.13: Cut through the momentum distribution at $p_z = 0$ in the $p_x p_y$-plane without (left) and with (right) broadening due to spontaneous emissions

neous emissions is shown in figure 4.13. On the left-hand side the momentum distribution in the $p_x p_y$-plane without broadening is plotted. There are high momentum components of up to $5\hbar k_0$. The broadened momentum distribution in the $p_x p_y$-plane is shown on the right-hand side. The structure of the momentum distribution was smoothed out and the distribution has a gaussian-like profile in the center. For different polarizations of the flash beam the width of the broadened momentum distribution changes, which can be used to analyze the correlation of the induced dipole moments and the interaction potential. We will present a discussion in more detail in the next chapter.

4.3 Ideal Numerical Parameters

Calculations in the far-detuned case are more accurate and much faster than in the resonant case. Therefore, in the following we will restrict the computation to cases with far-detuned light. The dependance of the induced potential on the numerical parameters was investigated in order to find an ideal set.

The parameter we will use for the numerical calculations are a grid size of $64 \times 64 \times 128$ points with a spacing of $\Delta l = 49$nm. The size of the region covered by the grid is 3.14μm$\times 3.14\mu$m$\times 6.28\mu$m. In the radial direction the full width of the condensate is on the order of the region. In the axial direction the condensate is two orders of magnitude longer than the field of view, but we found the influence on the induced potential of the atoms separated more than 3μm to be negligible.

4.4 Summary

In this chapter we discussed the general structure of the calculation and the different quantities needed. We applied the calculations to two cases, the

resonant flash beam and the far-detuned flash beam and discussed the problems encountered. We found that the computation of the resonant case is too time-consuming, as the intensity profile has to be calculated selfconsistently in every step of the selfconsistent calculation of the interaction potential, and the interaction potential depends more strongly on the initial conditions than in the case of the far-detuned flash beam. On the contrary in the case of the far-detuned flash beam no selfconsistency is required and the incoherent background can be neglected. Therefore, in the following we will focus on the case of the far-detuned flash beam. The results and the interpretation of the calculations will be presented in the next chapter.

5. Results of the Numerical Calculations

In this chapter we are going to present the results achieved by applying the methods shown in the last section for different parameters. The parameters we are going to vary are the polarization of the incident beam, the radial width of the cloud, the depth of the optical lattice and the separation of the lattice sites. The polarization of the incident light beam corresponds to the orientation of the dipoles, the radial width of the cloud to the aspect ratio of the cloud and the radial broadening of the interaction potential, the depth of the optical lattice to the peak density and the axial broadening of the interaction potential and the separation of the discs to the next neighbor interaction. Thereafter, we will discuss the resulting momentum distribution of the atoms for different interaction times and present boundary conditions for the first approach for measurements of the mechanical effects caused by the light induced dipole-dipole interaction.

5.1 Light Induced Dipole-Dipole Interaction Potential

In the following we are going to discuss the dependance of the induced potential on different parameters. This is important to set boundary conditions for the experiment and for the estimation of the expected error. After the theoretical examination of the interaction we found that the ideal parameters for the experiment are as listed below. If not mentioned otherwise, these parameters will be used for all following calculations:

BEC	Lattice	Flash Beam
$\sigma_r = 1.4\mu$m	$U_{\text{lat}} = 240 E_{\text{rec}}$	$\delta_{\text{L}} = 2\pi$ 100MHz
$\sigma_z = 300\mu$m	$\sigma_{\text{lat}} = 110$nm	$I_0 = 1120 I_{\text{sat}}$
$\rho_0 = 10^{14}\text{cm}^{-3}$	$\rho_{\text{lat}} = 5.9 \cdot 10^{14}\text{cm}^{-3}$	z-polarized
long axis = z-axis	$\vec{k}_{\text{lat}} = k_{\text{lat}}\,\vec{e}_z$	$\vec{k} = k\,\vec{e}_y$
	$\lambda_{\text{lat}} = 785$nm	

The power and the waist of the lattice beam are $P = 0.58$W and $\sigma = 300\mu$m. We are going to neglect three-body losses, the attenuation and refraction of the flash beam and the spontaneous background intensity. The momentum

distribution will be observed either in the the x- or the y-direction. The density distribution is shown in figure 4.4.

One parameter that can be varied experimentally is the density of the BEC. The interaction potential is scaled linearly by the peak density of the cloud:

$$U_{\text{liddi}}(\vec{r}_0) = \int_{-\infty}^{\infty} V_{\text{AB}}(\vec{r}_0 - \vec{r}) n(\vec{r}) d^3r = \rho_{\text{lat}} \int_{-\infty}^{\infty} V_{\text{AB}}(\vec{r}_0 - \vec{r}) n'(\vec{r}) d^3r \ , \quad (5.1)$$

where $n'(\vec{r})$ is the atomic density distribution $n(\vec{r})$ divided by the peak density ρ_{lat}. For different densities or atom numbers the potentials can be scaled. Further calculations will be done using the same peak density.

5.1.1 Variation of the Polarization

We will start the discussion with the behaviour of the induced potential for different polarizations of the flash beam.

We decompose the induced potentials into a short-range static and long-range dynamic part. The static part corresponds to the interaction with a $1/r^3$ dependance of all dipoles pointing into the same direction, the dynamic part to the retardation with up to $1/r$-terms. The contribution of these two parts to the full interaction potential for different polarizations is shown in figure 5.1. φ is the angle of the polarization with respect to the z-axis ($\varphi = 0° : z$-polarized beam, $\varphi = 90° : x$-polarized beam).

The static part of the potential varies over a range of $2\hbar\Gamma$ and changes its sign at the magic angle $\varphi = 54.7°$, where as discussed in section 2.2.1 the static interaction vanishes. The shape of the static potential is similar to the shape of the density distribution. The dynamic part of the interaction is approximately $1\hbar\Gamma$, is mainly attractive in the direction of the flash beam and tends to zero perpendicular to it. Only the center of the dynamic potential is depending on the polarization.

The resulting potential varies over a range of $4\hbar\Gamma$ and is dominated in the center by the static and at the boarder by the dynamic part. The mechanical effects we are interested in are caused by the gradients of the induced potentials. The direction and the magnitude of the gradients for different polarizations of the flash beam are shown in figure 5.2. For z-polarized light the interaction is repulsive and for x-polarized light it is attractive. The maximum acceleration of the atoms due to the potential is on the order of 50000 $\text{m/s}^2 \approx 0.226 \ \frac{\hbar k \Gamma}{m}$.

By considering the x- and the y-direction separately, we find two characteristic angles where the gradients vanish, namely $\varphi = 36°$ and $\varphi = 54°$ as can be seen in figures 5.1 and 5.2. At these angles the momentum distribution is hardly changed by the potential. At $\varphi = 54°$ the gradient into the y-direction is zero because the static part vanishes and the dynamic part doesn't have a gradient in that direction. At $\varphi = 36°$ the gradient in the x-direction vanishes because the static and dynamic effects cancel each other.

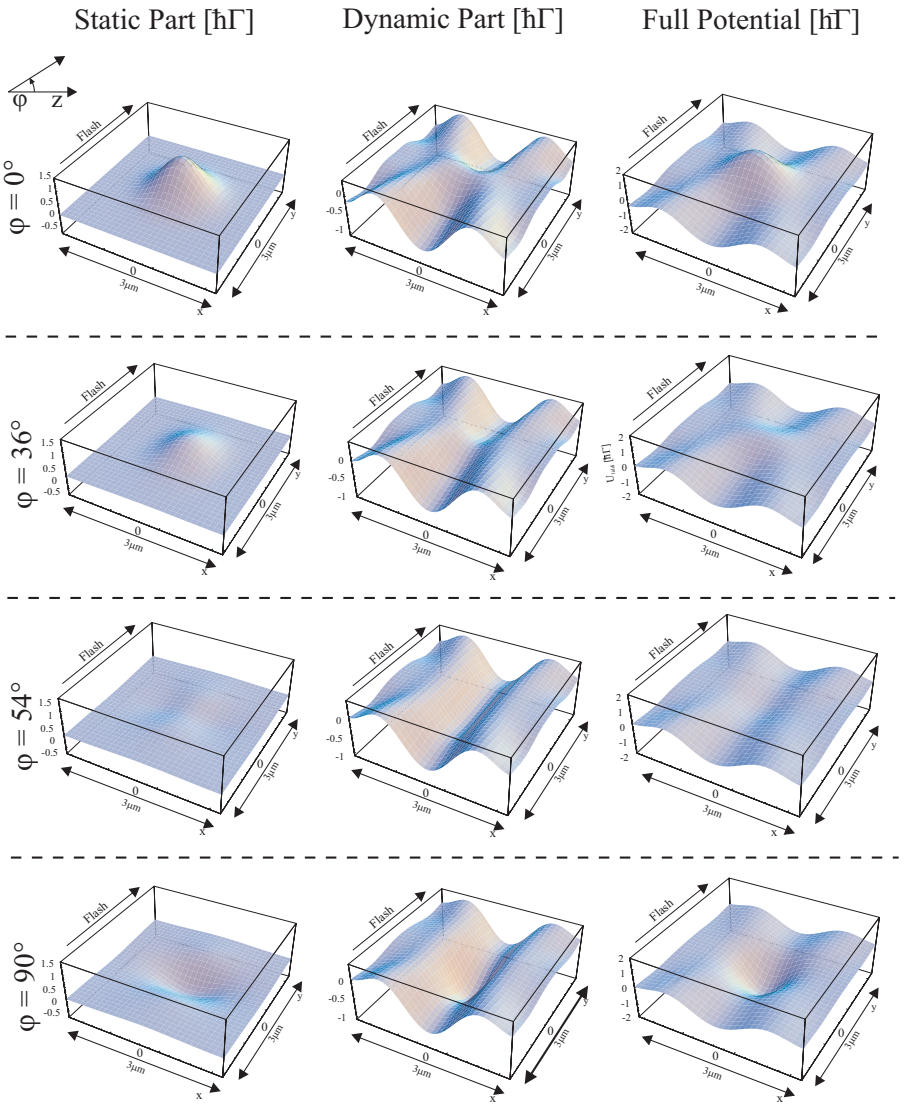

Fig. 5.1: Cut at $z = 0$ through the static and dynamic parts of the light induced dipole-dipole interaction potential and the full potential for different incident polarizations. φ is referring to the angle of the polarization with respect to the z-axis.

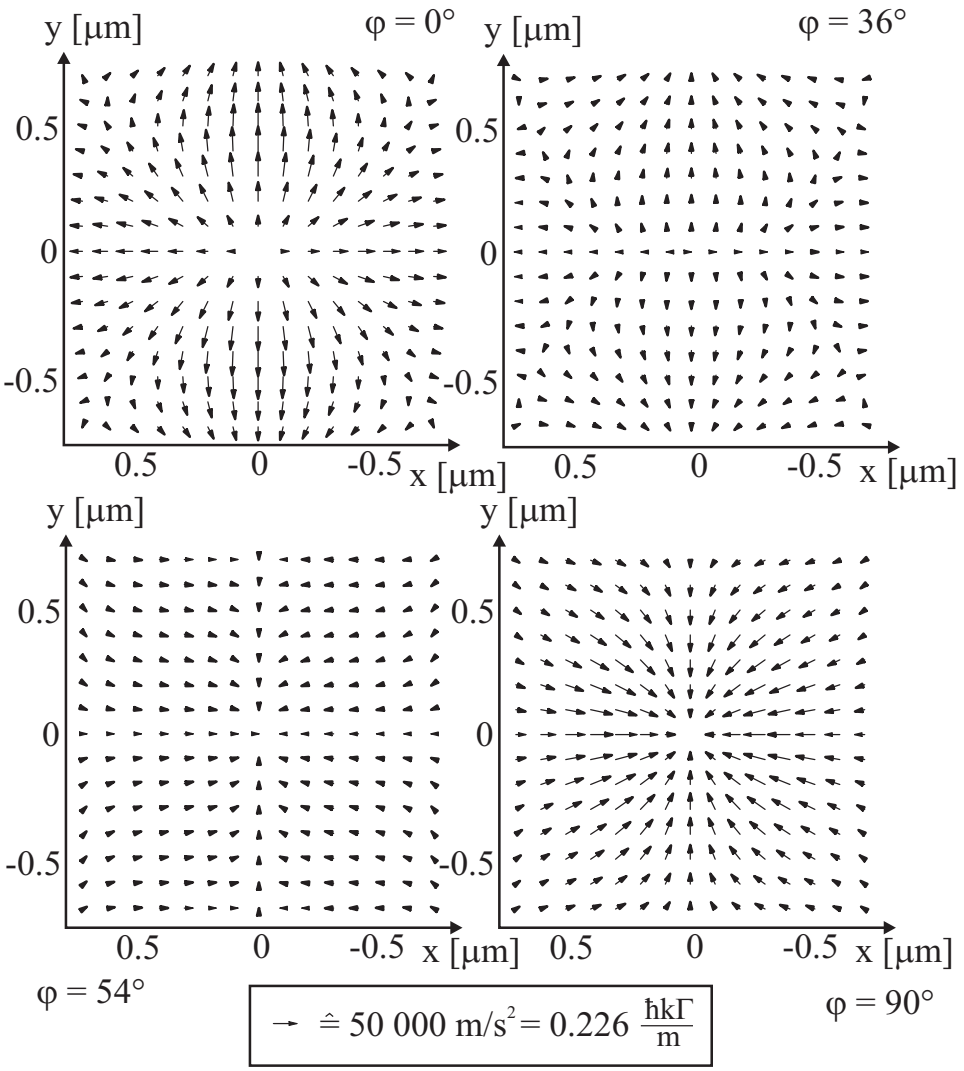

Fig. 5.2: Gradient of the light induced dipole-dipole interaction potential in the xy-plane at $z = 0$ for different polarizations of the flash beam in the center of the cloud.

5.1.2 Variation of the Radial Width of the BEC

The general shape of the interaction potential in the radial direction is strongly correlated to the widths of the dipole moment distribution. The interaction potential along the y-axis for different widths is plotted on the left-hand side in figure 5.3, where the peak density is kept constant at $\rho_{\mathrm{lat}} = 6 \cdot 10^{14} \mathrm{cm}^{-3}$.

On the right-hand side the maximal gradient of the induced potential in the radial direction is shown. As can be seen the gradient increases with decreasing widths of the cloud: $\max(|dU/dr|) \propto \sigma_r^{-1}$. Note that at the same time the number of atoms is decreased and with it the depth of the potential.

The maximum of the curve $\max(|dU/dr|)$ is at $\sigma_r = \lambda/2$,its progression can be explained by considering the convolution of the interaction potential and the density distribution as a broadening of the potential. If the broadening

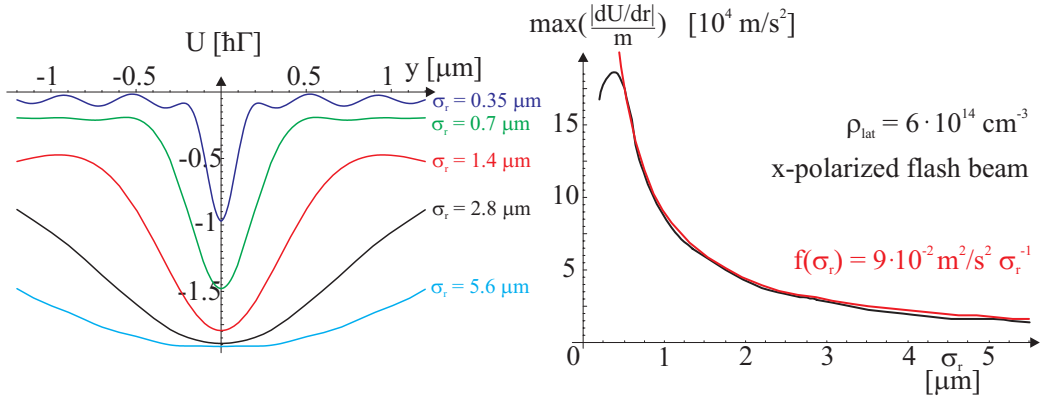

Fig. 5.3: Induced Potential along the y-axis at $x = z = 0$ for an x-polarized flash beam and different width of the BEC (left-hand side) and its maximal gradient in the radial direction (right-hand side, black curve). The red curve (right-hand side) is a σ_r^{-1} fit. The density is kept constant at $\rho_{\text{lat}} = 6 \cdot 10^{14}\text{cm}^{-3}$.

is larger than the scale on which the interaction potential decreases then the change of the gradient is dominated by the broadening, if it is smaller the change is dominated by the loss in atom number. Further analysis showed a similar qualitative behaviour for all polarizations of the flash-beam.

A quadratic fit of the potentials for $\sigma_r = 0.7$, 1.4 and 2.8μm is given by:

$$U = -0.136\,\hbar\Gamma(-5.79\mu\text{m} + \sigma_r)(1.38\mu\text{m} + \sigma_r)\,, \tag{5.2}$$

where σ_r is expressed in μm. This fit will be used for the estimation of possible systematic errors in the planned experiment in section 5.1.5.

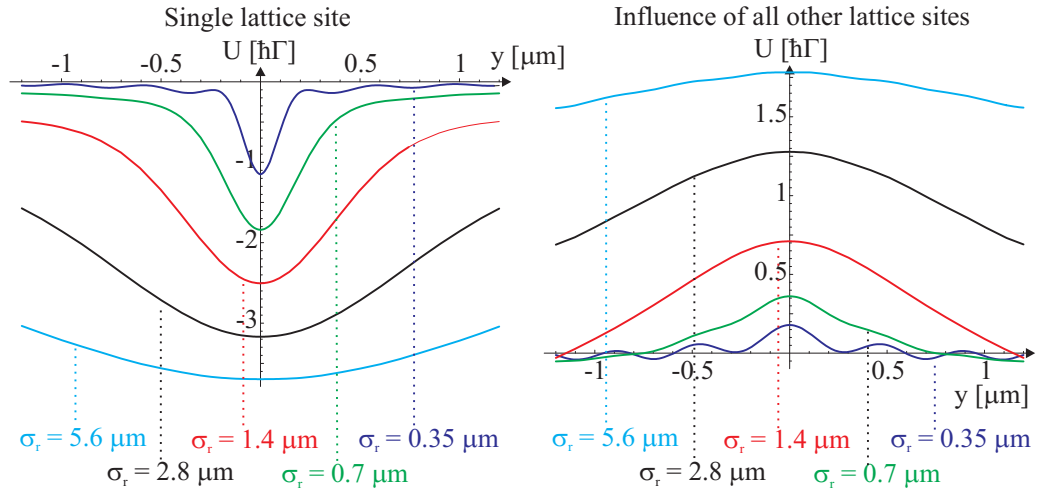

Fig. 5.4: Contribution to the full induced potential of a single lattice site (left-hand side) and of all other lattice sites (right-hand side) along the y-axis at $x = z = 0$ for an x-polarized flash beam, $\rho_{\text{lat}} = 6 \cdot 10^{14}\text{cm}^{-3}$ and different width of the BEC.

Figure 5.4 shows on the left-hand side the contribution of the central lattice site to the full potential and on the right-hand side the contribution of all

other lattice sites for an x-polarized flash beam and the same parameters as for figure 5.3. The attractive potential within the disk is partially cancelled by the repulsive interaction with the other disks. For a z-polarized flash beam the situation is reversed. The contribution of the central lattice site is repulsive and is enlarged due to the interaction with the other lattice sites.

A small radial width is crucial for measurements of the mechanical effects in order to maximize the gradients, even if this is connected to the loss of atoms and a decrease of the potential depth. The main effect results from the dipole-dipole interaction within the discs but due to the next neighbor interaction the depth is changed significantly. For the parameters presented the interaction potential is reduced by the next neighbor interaction induced by x-polarized light and it is increased by the next neighbor interaction induced by z-polarized light.

5.1.3 Variation of the Lattice Spacing

Variations of the lattice spacing on the scale of the radial width of the cloud don't affect the qualitative shape of the potential. The width of the potential and its value at the surface of the cloud remain approximately unchanged, the gradient is scaled by the value of the potential at the center.

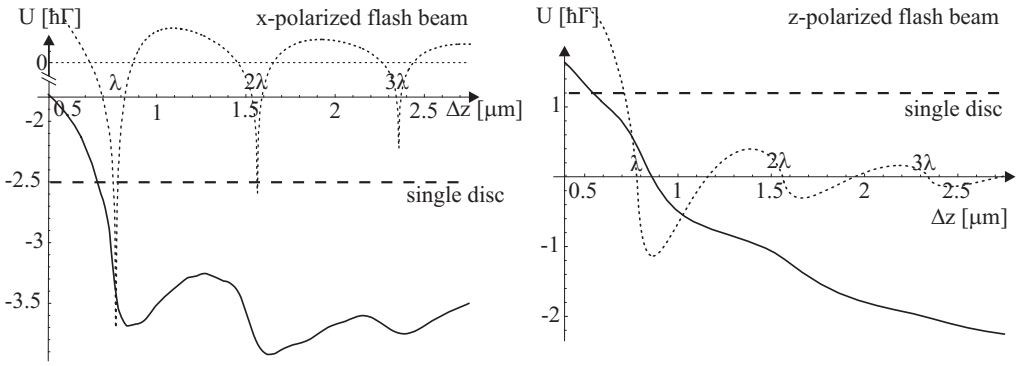

Fig. 5.5: Potential at the center of the BEC versus the separation of the lattice sites for a x-polarized flash beam (left-hand side) and a z-polarized flash beam (right-hand side). The full line corresponds to the interaction potential of 16 discs, the dotted line to the interaction potential of 100 point-like oscillating dipoles separated by $\Delta z = \lambda_{\mathrm{lat}}/2$ and the dashed line to the interaction potential within a single disc. The interaction potential depth approaches this value for large separations of the discs ($\Delta z \to \infty$).

In figure 5.5 the potential at the center of the cloud is plotted versus the lattice spacing for z- and x-polarized flash beams. For comparison the dotted lines correspond to the interaction potential for 100 point-like dipoles separated by Δz for both polarizations. The resonances in the point-like dipole picture result from the λ-periodicity of the interaction potential. For an x-polarized flash beam the resonance structure is broadened and the minima

appear slightly shifted to higher separations compared to the resonances of the point-like picture at $\Delta z = j\,\lambda$ with $j \epsilon \mathbb{N}$. In the case of a z-polarized flash beam, the structure expected due to the point-like picture is smeared out.

The broadening of the resonance structure for x-polarized flash beams appears because the separation of the lattice sites is comparable to the radial width of the cloud and the interaction for different angles and separations is integrated. In contrast the structure for z-polarized flash beams tends to be smeared out much more because the potential in the point-like picture varies slower and doesn't show sharp resonances.

By tuning the separation of the lattice sites and with it the next neighbor interaction not only the depth but also the sign of the interaction potential can be altered. For large separations ($\Delta z \to \infty$) the depth of the interaction potential approaches the single disc potential.

5.1.4 Variation of the Depth of the Optical Lattice

The variation of the lattice depth has two consequences on the atomic density distribution, the axial width of the discs and the peaks density are changed. The qualitative shape of the interaction potentials is not altered by these variations. The potential along the y-axis for different lattice depths is shown on the left-hand side in figure 5.6, where the initial peak density of the BEC was set to $\rho_0 = 10^{14}\mathrm{cm}^{-3}$.

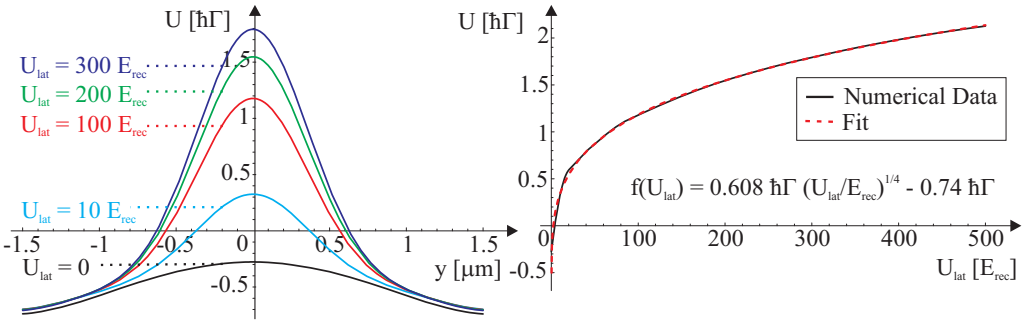

Fig. 5.6: Light induced interaction potential along the y-axis for different lattice depths for a z-polarized flash beam (left-hand side) and the potential at the center of the cloud versus the lattice depth (right hand side). The black curve is representing the numerical data and the red-dashed curve is a $\sqrt[4]{U_{\mathrm{lat}}}$ fit.

The peak density within an optical lattice is given by equation 2.63 and is proportional to $\rho_{\mathrm{lat}} \propto \sqrt[4]{U_{lat}}$. Figure 5.6 shows on the right-hand side the dependance of the induced potential at the center of the cloud on the lattice depth (black curve). The red-dashed curve is a $f(U_{\mathrm{lat}}) = c_0\,\sqrt[4]{U_{lat}} + c_1$ fit which approximates the numerical data for depths larger than $10E_{\mathrm{rec}}$ very

well[1].

Hence, for lattices deeper than $10E_{\mathrm{rec}}$ the changes of the potential are mainly caused by the increase of the atomic density and not by a change of the shape of the atomic cloud. Without an optical lattice the static interaction is averaged out and the potential becomes basically independent of the polarization[2] of the incident beam. Deep lattices are needed to increase the magnitude of the interaction potential and its gradient, to transform a 3D- into a quasi 2D-dipole distribution (with $U_z(0) \neq U_x(0)$) and with that to allow us to reach into a regime where measurable effects can be expected.

5.1.5 Error due to Imperfect Initial Conditions

With the discussion from above we can estimate to which extent variations of the initial conditions modify the interaction potential. This "stability" analysis is very important as its results constrain the experimental setup. We are considering explicitly the influence of the atomic density, the radial width of the cloud, the lattice depth, the flash beam intensity and the angle of the flash beam polarization with respect to the z-axis. All other parameters (like the light frequency, the axial length of the cloud etc.) are not changing the resulting potential significantly as long as they are correct within 10%.

Assuming that the potential induced by x-polarized light and the potential induced by z-polarized light are independent and may be added to get the full interaction potential for imperfectly polarized light, then in first order the interaction potential can be approximated by:

$$U(0) = U_x(0)\frac{d^2|_{I=I_x}}{d^2|_{I=I_0}} + U_z(0)\frac{d^2|_{I=I_z}}{d^2|_{I=I_0}} \,, \tag{5.3}$$

where d is the induced dipole moment, I_x and I_z are the intensities of the x- and z-polarized fraction of the flash beam intensity and $U_x(0)$ and $U_z(0)$ are the interaction potentials at the center of the cloud for x- and z-polarized light respectively. Equation 5.3 approximates the potential at the center of the cloud for a composition of x- and z-polarized light, for $I_z = 0 \rightarrow U(0) = U_x(0)$ and for $I_x = 0 \rightarrow U(0) = U_z(0)$.

The error of the potential can be approximated by:

$$\frac{\Delta U}{U} \approx \frac{1}{U}\left(\left|\frac{\partial U}{\partial \rho_{\mathrm{lat}}}\Delta\rho_{\mathrm{lat}}\right| + \left|\frac{\partial U}{\partial \sigma_r}\Delta\sigma_r\right| + \left|\frac{\partial U}{\partial U_{\mathrm{lat}}}\Delta U_{\mathrm{lat}}\right| + \left|U|_{I=I_0} - U|_{I=I_x}\right|\right) . \tag{5.4}$$

As an example we are considering the potential induced by an x-polarized

[1] For lattice depths larger than $100E_{\mathrm{rec}}$ the error is $< 0.1\%$, for lattice depths between $10E_{\mathrm{rec}}$ and $100E_{\mathrm{rec}}$ the error is $< 5\%$.

[2] $U_z(\vec{0}) = -0.277\hbar\Gamma$ and $U_x(\vec{0}) = -0.250\hbar\Gamma$

flash beam:

$$\frac{\Delta U_x(0)}{U_x(0)} \approx \frac{1}{U_x(0)}\left(\left|U_x(0)\frac{\Delta\rho_{\rm lat}}{\rho_{\rm lat}}\right| + \left|(0.459\hbar\Gamma - 0.204\hbar\Gamma\mu{\rm m}^{-1}\sigma_r)\Delta\sigma_r\right| + \left|0.608\hbar\Gamma\frac{\Delta\, U_{\rm lat}}{4(U_{\rm lat}/E_{\rm rec})^{3/4}}\right| + \left|U_x(0) - \left(U_x(0)\frac{d^2|_{I=I_x}}{d^2|_{I=I_0}} + U_z(0)\frac{d^2|_{I=I_z}}{d^2|_{I=I_0}}\right)\right|\right) .$$

For our standard experimental parameters and assuming high fluctuations $\Delta\rho_{\rm lat}/\rho_{\rm lat} = 0.1$, $\Delta\sigma_r/\sigma_r = 0.1$, $\Delta U_{\rm lat}/U_{\rm lat} = 0.2$ and $(I_0 - I_x)/I_0 = 0.05$ the error is[3]:

$$\frac{\Delta U_x(0)}{U_x(0)} = 0.3 . \tag{5.5}$$

The error of 30% results mainly from the imperfection of the polarization and from density fluctuations. The error of the potential induced by flash beams with different polarizations is on the same order of magnitude.

5.2 Momentum Distribution

The first approach to investigate the light induced dipole-dipole interaction is to measure the resulting atomic momentum distribution for different polarizations of the incident beam. The momentum is broadened due to three effects, the mean-field, the dipole-dipole interaction and the spontaneous emissions $\sigma_k = \sigma_{\rm k,mean} + \sigma_{k,\rm int} + \sigma_{k,\rm sp}$. The dependance of the half-width σ_k of the momentum distribution in the x- and y-direction on the polarization of the incident beam for different interaction times Δt is shown in figure 5.7. The half-width σ_k is found by fitting a gaussian function $\tilde{f}(k) = c_0\exp(-2\frac{k^2}{\sigma_k^2})$ to the distribution. The dotted lines correspond to the broadening due to spontaneous emissions. For $\Delta t = 500$ns the half width of the momentum distribution varies over a range of $\sigma_k = 3$ to 10 $\hbar|\vec{k}|$ which corresponds to $T = 0.27$ to 3.02μK and mean velocities of $\bar{v} = 8.8$ to 29mm/s.

In the Raman-Nath regime $\sigma_{k,\rm int} \propto \Delta t$ and $\sigma_{k,\rm sp} \propto \sqrt{n_{\rm sp}} \propto \sqrt{\Delta t}$. For $\Delta t <$ 100ns the broadening is dominated by spontaneous emissions, for $\Delta t >$ 100ns by the interaction as shown in figure 5.7. The atoms reach the steady state after 150ns to 200ns. With our methods we are not able to estimate the magnitude of the induced potential during the transient period. Therefore, we choose the interaction time for the given parameters to be at least 100ns longer than the transient period $\Delta t > 300ns$ to make sure that the regime in which the broadening is dominated by the interaction is reached.

In both directions there is an angle of minimal broadening. Minimal broadening appears, if the gradient of the full interaction potential vanishes. The gradient of the dynamic part is mainly directed into the x-direction as can be seen in figure 5.1. Hence, the angle of minimal broadening in the y-direction

[3] For $\Delta\rho_{\rm lat}/\rho_{\rm lat} = 0.05$ and $(I_0 - I_x)/I_0 = 0.02$: $\frac{\Delta U_x(0)}{U_x(0)} = 0.15$.

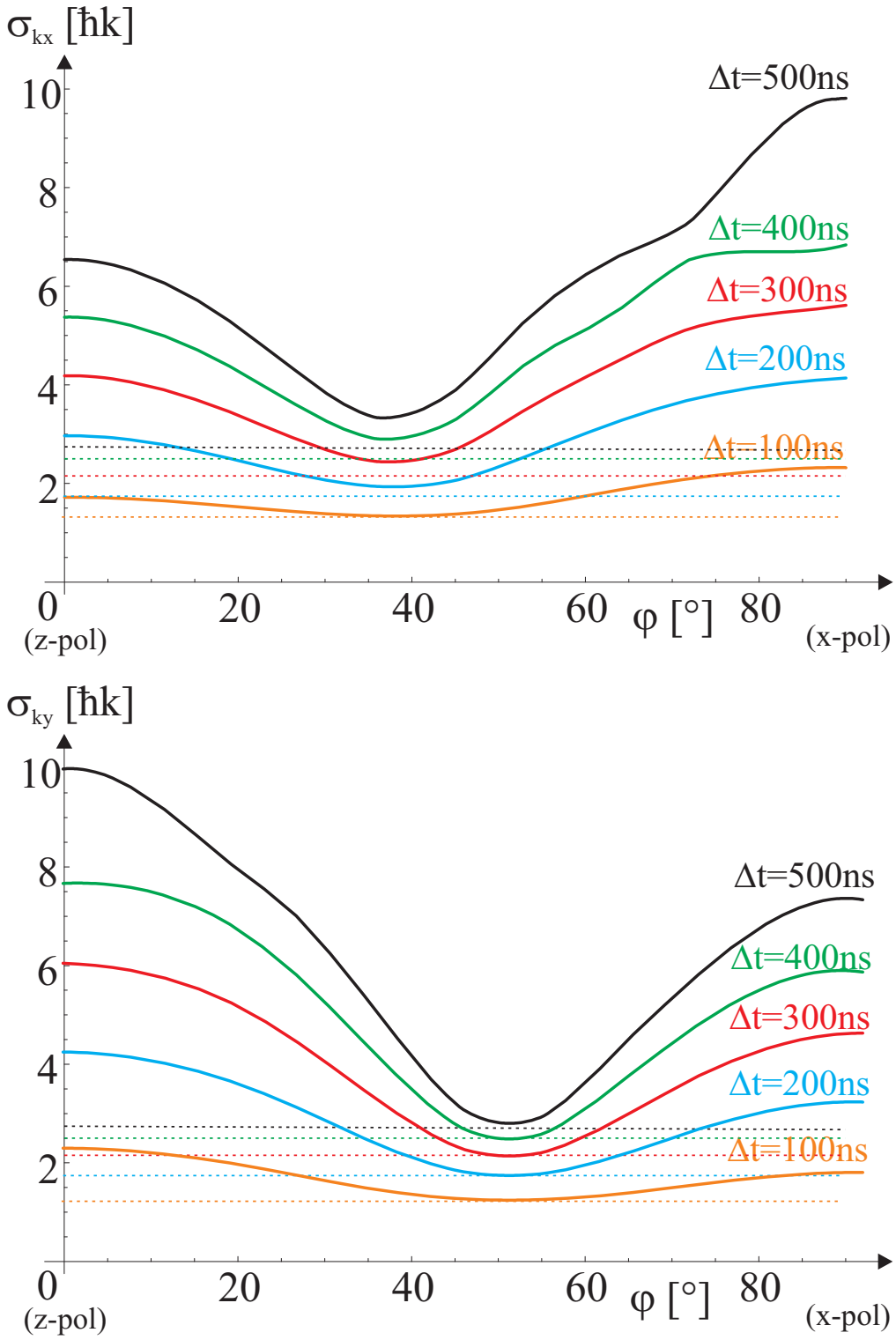

Fig. 5.7: Half-width of the momentum distribution in the x-direction (left-hand side) and y-direction (right-hand side) after the interaction versus the polarization of the incident beam for different interaction times. The dotted lines correspond to the broadening due to spontaneous emissions for the different times.

$\varphi = 52°$ is close to the magic angle for static dipoles $\varphi_{\mathrm{M}} = 55°$. As the gradient of the potential vanishes almost completely the momentum distribution is only broadened by spontaneous emissions $\min(\sigma_k) = \sigma_{k,sp}(\Delta t)$.

Due to the gradient of the dynamic part the angle of minimal broadening in the x-direction is shifted with respect to the magic angle. The gradient of the full interaction potential vanishes at $\varphi = 38°$, but it vanishes only in the center of the cloud, therefore the minimal half-width of the momentum distribution $min(\sigma_k) > \sigma_{k,sp}(\Delta t)$.

The momentum distribution is broadened by the dipole-dipole interaction to a width that is several times larger than $\sigma_{k,sp}(\Delta t)$. Assuming high fluctuations as discussed in section 5.1.5 the error is: $\Delta\sigma_k/\sigma_k(\Delta t = 500\mathrm{ns}) \leq 0.20$ and $\Delta\sigma_k/\sigma_k(\Delta t = 100\mathrm{ns}) \leq 0.15$. For $\Delta t > 100$ns the broadening due to the interaction is still dominant, even if the initial conditions are imperfect.

On the experimental side the flash-time, which corresponds to the mean velocity of the atoms, is constrained by the time in which the magnetic confinement is switched off. The momentum distribution is approximated correctly by the method used in our calculation, if the expansion of the cloud is not perturbed. Therefore, we have to turn the magnetic fields off rapidly. Due to the average velocity of the atoms after the flash we can estimate the timescale by:

$$T_{\mathrm{trap}} \lesssim \frac{\sigma_r/2}{\bar{v}} = \frac{m\,\sigma_r/2}{\hbar|\vec{k}|\,\Gamma_{\mathrm{sp}}\Delta t}\,, \tag{5.6}$$

where $\bar{v}$ is the mean velocity. Equation 5.6 is valid, if the atoms are not moving further than half the radial width of the cloud in average during the time the magnetic trap is turned off. For our standard parameters ($\Gamma_{\mathrm{sp}}\Delta t \approx 5$, $\sigma_r = 2\mu$m) $T_{\mathrm{trap}} \approx 35\mu$s. In the experiment the magnetic fields are switched off in 40μs which corresponds to an additional broadening[4] of about 2%.

As described in this section we plan the measurement to be carried out by irradiating the BEC with far-detuned laser light and measure the momentum distribution for different polarizations of the flash beam. We expect minimal broadening for characteristic angles, which are depending on the initial conditions. More insight into the effects caused by the interaction may be won by varying the initial conditions like density, width of the BEC or the parameters of the optical lattice.

[4] The rapid switching of the magnetic trap is very important. If the magnetic field is ramped down in 300μs the broadening is up to 120%.

6. Conclusions and Outlook

6.1 Conclusions

In this thesis we presented a semiclassical theory describing the light induced dipole-dipole interaction within an atomic cloud in the Raman-Nath regime and applied the methods discussed to the case of light induced dipoles. We investigated theoretically the mechanical effects that the light induced dipole-dipole potential exerts onto atoms of a BEC. The main results of the calculations are the proposal under which experimental conditions and how these mechanical effects can be observed and measured for the first time. The calculation of the induced potential was carried out by determining the dipole moment with the optical Bloch equations and evaluating the convolution of the dipole-dipole interaction potential and the density distribution in Fourier-space. The resulting momentum distribution was obtained by propagating the wavefunction of the atomic cloud in time and taking the broadening due to spontaneous emissions into account. The regime in which we plan to carry out the experiment is characterized by a density on the order of $\rho_0 \approx 6 \cdot 10^{14}$ atoms/cm^3, a radial width of the cloud of $\sigma_r \approx 2\mu$m, an optical lattice depth of $U_{\text{lat}} = 200 E_{\text{rec}}$ and a flash time of $\Delta t \approx 500$ns. A high density is needed as it linearly scales the interaction potential and the small radial width as the interaction potential is broadened by the radial shape of the cloud. Due to the deep optical lattice the dipole distribution becomes two dimensional and the interaction becomes strongly dependant on the polarization of the flash-beam.

The first approach to measure mechanical effects caused by the light induced dipole-dipole interaction will be the measurement of the momentum distribution for different polarizations of the incident flash beam. We expect an angle of minimal broadening which corresponds to a vanishing gradient of the induced potential. By investigating the minima for different initial conditions and different directions of observation the influence of the static and the retarded interaction can be analyzed. By varying the lattice depth and the lattice spacing more information about the dipole-dipole interaction potential is gained.

From the experimental point of view our system is basically ready to perform the measurements. We can produce Bose-Einstein condensates on a daily basis with high radial confinement and the 1D optical lattice is set up and operational as demonstrated. The magnetic trap (~ 1000A) can be switch off within 40μs which is necessary to not to perturb the expansion of the BEC.

6.2 Outlook

After the first measurement of the mechanical effects caused by the light induced dipole-dipole was carried out successfully by demonstrating that the broadening of the momentum distribution is depending on the flash-beam polarization as predicted, we plan to repeat the measurement for different initial conditions and for several configurations of the optical lattice. Measurements without optical lattices are also of interest as the static interaction is averaged out and we are able to investigate the effects caused only by the retardation.

The discussion presented in the last chapter was about the interaction of periodic quasi two-dimensional dipole distributions in 1D optical lattices. 2D-lattices may be considered in order to increase the density even further and to analyze the interaction between periodic quasi one-dimensional dipole distributions. By investigating the interaction in 3D-optical lattices at moderate densities (one atom per lattice site) the long range interaction of single dipoles becomes dominant. By varying the lattice spacing and the polarization of the driving field more insight into the effects caused by retardation may be won.

The light induced dipole-dipole interaction has a wide range of possible applications. It might be used for example as a tool for investigating the population of Mott-insulator states in a 3D-optical lattice [12, 61]. By inducing dipole moments in the atoms, only lattice sites with two (or more) atoms are affected. If the induced potential is deep enough the atoms can gain enough energy to leave the trap and only lattice site with less then two atoms stay populated.

Another effect that is worth being investigated is *superradiance*. Even if superradiance in the Bragg regime [62] is suppressed due to the short pulse times and the deep lattices used for the experiment, superradiance in the Raman-Nath regime [63] may be of interest. It is challenging to find a transition from the regime where the superradiance is dominant to the dipole-dipole interaction regime which can be analyzed by varying the intensity of the flash beam.

The light induced dipole-dipole interaction has also proposed applications in quantum information processing [64], which is accomplished by exciting states with strong interactions. The resulting *dipole blockade* can be used to inhibit transitions into all but singly excited collective states. This can be employed for controlled generation of collective atomic spin states as well as nonclassical photonic states and for scalable quantum logic gates. Other possibilities for the creation of entangled states and the realization of quantum computation in periodic potentials is discussed in [14, 65].

The spin dynamics of BECs confined in 1D optical lattices may be studied as well by controlling the light induced dipole-dipole interaction [66]. The condensates at each lattice sites behave like spin magnets. Their site-to-

site interaction can distort the ground-sate spin orientation and lead to the excitation of spin waves.

Other applications of the light induced dipole-dipole interaction have been proposed in [18–23] like one-dimensional compression, collective excitations or supersolid formation in BECs.

The program for the computation developed in this thesis is not restricted to the light induced dipole-dipole interaction but may be used to compute a wide range of interaction potentials. Potentials may be calculated for any kind of density distribution and any kind of two body interaction which can be described as a classical potential spatially only depending on the separation of the two particles. For example the interaction potential within a magnetic fluid or a spin condensate can be computed but also Coulomb or mean-field interactions may be considered as well.

Appendix A

Dipole-Dipole Interaction in Isotropic Dipole Distributions

The potential of a spherical symmetric distribution of identical dipoles may be calculated using equation 2.43:

$$U_{\text{eff}}(\vec{0}) = \int_0^R \int_0^\pi \int_0^{2\pi} V_{\text{AB}}(r,\theta,\phi)|\sin(\theta)|r^2 d\phi d\theta dr \ , \tag{A.1}$$

where we are using spherical coordinates. In the static case $V_{\text{AB}}(r,\theta,\phi)$ is equation 2.40:

$$U_{\text{eff}}(\vec{0}) = \int_0^R \int_0^\pi \int_0^{2\pi} \frac{d^2}{4\pi\varepsilon_0 r} \cdot (1 - 3\cos^2(\theta))|\sin(\theta)| d\phi d\theta dr \ . \tag{A.2}$$

The θ integral:

$$\int_0^\pi (|\sin(\theta)| - 3|\cos^2(\theta)\sin(\theta)|) d\theta =$$
$$[-\cos[\theta] - \tfrac{3\cos(\theta)+\cos(3\theta)}{12}]_0^\pi = [2 - 3 \cdot \tfrac{2}{3}] = 0 \ , \tag{A.3}$$

vanishes, which means that the potential U_{eff} in the center of a spherical symmetric distribution of dipoles is zero.

For the case of light induced dipoles the static part of the interaction becomes zero as well, but there is still an effective potential left due to dynamical effects. A discussion on this topic in more detail may be found in [18].

Appendix B

Convolution in Fourier Space

A convolution might be calculated by using the *Fourier transformation*, defined in one dimension as:

$$\tilde{F}(k) = \frac{1}{\sqrt{2\pi}} \int_{-\infty}^{\infty} e^{(-ikx)} F(x) dx \tag{B.1}$$

$$F(x) = \frac{1}{\sqrt{2\pi}} \int_{-\infty}^{\infty} e^{(ikx)} \tilde{F}(k) dk \ , \tag{B.2}$$

but can also be extended to three dimensions by performing three separate Fourier transformations for every spacial dimension.

By using equation B.2 a convolution can be rewritten as:

$$h(x_0) = \int_{-\infty}^{\infty} f(x_0 - x) g(x) dx \tag{B.3}$$

$$= \int_{-\infty}^{\infty} \frac{1}{2\pi} \left(\int_{-\infty}^{\infty} e^{ik(x0-x)} \tilde{f}(k) dk \right) \left(\int_{-\infty}^{\infty} e^{ik'x} \tilde{g}(k') dk' \right) dx$$

$$= \int_{-\infty}^{\infty} \int_{-\infty}^{\infty} e^{ikx_0} \tilde{f}(k) \tilde{g}(k') \frac{1}{2\pi} \int_{-\infty}^{\infty} \left(e^{i(k'-k)x} dx \right) dk dk'$$

$$= \int_{-\infty}^{\infty} \int_{-\infty}^{\infty} e^{ikx_0} \tilde{f}(k) \tilde{g}(k') \delta(k' - k) dk dk'$$

$$h(x_0) = \sqrt{2\pi} \frac{1}{\sqrt{2\pi}} \int_{-\infty}^{\infty} e^{ikx_0} \tilde{f}(k) \tilde{g}(k) dk \ . \tag{B.4}$$

To carry out the convolution and calculate $h(x_0)$, we have to Fourier-transform $f(x_0 - x)$ and $g(x)$ separately, multiply the two functions and transform back.

By using algorithms like FFT (fast Fourier transformation) the numerical calculation of convolutions of large arrays becomes possible on acceptable timescales.

Appendix C

Dipole Moment with Spontaneous Background

As described in section 2.1.4, the amplitude of the dipole moment is given by (equation 2.31):

$$d_{0,\mathrm{st}} = d_{\mathrm{M}} = \sqrt{\frac{3\Gamma\varepsilon_0 hc^3}{\omega_0^3}} \cdot \frac{\sqrt{\frac{I_0}{I_{\mathrm{sat}}} \cdot (1 + \frac{4\delta_{\mathrm{L}}^2}{\Gamma^2})}}{1 + \frac{4\delta_{\mathrm{L}}^2}{\Gamma^2} + \frac{I_0}{I_{\mathrm{sat}}}} \,, \tag{C.1}$$

and the local intensity approximated by (equation 4.16):

$$I_{\mathrm{loc}} = \left(\sqrt{I_{\mathrm{coh}}} + \cos(\phi) \sqrt{I_{\mathrm{sp}}} \right)^2 . \tag{C.2}$$

The effective dipole moment in the presence of a coherent electromagnetic field and an incoherent background may be calculated by inserting $I_{\mathrm{loc}} \rightarrow I_0$ in equation C.1 and average over the phase ϕ of the incoherent background:

$$d_{\mathrm{eff}} = \frac{1}{2\pi} \int_{-\pi}^{\pi} d_{\mathrm{M}}(\phi) d\phi \,, \tag{C.3}$$

where

$$d_{\mathrm{M}}(\phi) = d_0 \frac{\sqrt{I_{\mathrm{coh}}} + \sqrt{I_{\mathrm{sp}}} \cos(\phi)}{I_{\mathrm{sat}} + (\sqrt{I_{\mathrm{coh}}} + \sqrt{I_{\mathrm{sp}}} \cos(\phi))^2 + 4 I_{\mathrm{sat}} \delta_L^2 / \Gamma^2} \tag{C.4}$$

$$d_0 = \sqrt{\frac{3\Gamma\varepsilon_0 hc^3}{\omega_0^3}} \sqrt{I_{\mathrm{sat}} \, (1 + \frac{4\delta_{\mathrm{L}}^2}{\Gamma^2})} \,. \tag{C.5}$$

To solve the integral (equation C.3) a substitution has to be made:

$$a \rightarrow \sqrt{I_{\mathrm{coh}}} + \sqrt{I_{\mathrm{sp}}} \cos(\phi) \tag{C.6}$$

$$\frac{da}{d\phi} = -\frac{1}{\sqrt{I_{\mathrm{sat}} - (a - \sqrt{I_{\mathrm{coh}}})^2}} \,. \tag{C.7}$$

The amplitude of the dipole moment becomes:

$$d_{\mathrm{M}}(a) = d_0 \frac{a}{I_{\mathrm{sat}} + a^2 + 4 I_{\mathrm{sat}} \delta_L^2 / \Gamma^2} = \frac{d_0 \, d_1 \, a}{1 + d_1 \, a^2} \tag{C.8}$$

$$d_1 = \left(I_{\mathrm{sat}} + I_{\mathrm{sat}} \frac{4\delta_L^2}{\Gamma^2} \right)^{-1} . \tag{C.9}$$

In order to calculate d_{M}, the integral (equation C.3) has to be solved:

$$d_{\mathrm{eff}} = -\frac{d_0\, d_1}{2\pi} \int_{a(-\pi)}^{a(\pi)} \frac{a}{1+d_1\, a^2}\, \frac{1}{\sqrt{I_{\mathrm{sat}} - (a-\sqrt{I_{\mathrm{coh}}})^2}}\, da \qquad \text{(C.10)}$$

$$= -\frac{d_0\, d_1}{\pi} \int_{a(0)}^{a(\pi)} \frac{a}{1+d_1\, a^2}\, \frac{1}{\sqrt{I_{\mathrm{sat}} - (a-\sqrt{I_{\mathrm{coh}}})^2}}\, da\,, \qquad \text{(C.11)}$$

the integral may be split into two parts from $u(-\pi)$ to $u(0)$ and from $u(0)$ to $u(\pi)$, which are equivalent since $u(\phi) = u(-\phi)$ is symmetric in ϕ. The integration was carried out using *Mathematica 4.2* and the result is:

$$d_{\mathrm{eff}} = \sqrt{\frac{3\Gamma^3 \varepsilon_0 h c^3}{\omega_0^3}}\, \mathrm{Re} \frac{\left[S^+ \left(\log - \frac{\sqrt{S_{\mathrm{sp}}}}{S^-} - \log \frac{\sqrt{S_{\mathrm{sp}}}}{S^-} \right) + S^- \left(\log - \frac{\sqrt{S_{\mathrm{sp}}}}{S^+} - \log \frac{\sqrt{S_{\mathrm{sp}}}}{S^+} \right) \right]}{S^-\, S^+}$$

$$\text{with} \quad S^{\pm} = \sqrt{1 \pm 2\imath\sqrt{S_{coh}} - S_{coh} + S_{sp}}\,,$$

$$S_{\mathrm{coh}} = \frac{\Gamma^2}{(\Gamma^2 + 4\delta_L^2)}\, \frac{I_{\mathrm{coh}}}{I_{\mathrm{sat}}} \quad , \quad S_{\mathrm{sp}} = \frac{\Gamma^2}{(\Gamma^2 + 4\delta_L^2)}\, \frac{I_{\mathrm{sp}}}{I_{\mathrm{sat}}}\,. \qquad \text{(C.12)}$$

Bibliography

[1] A. E. Leanhardt, T. A. Pasquini, M. Saba, A. Schirotzek, Y. Shin, D. Kielpinski, D. E. Pritchard, und W. Ketterle. Cooling Bose-Einstein condensates below 500 Picokelvin. *Science*, **301**:1513, September 2003.

[2] Albert Einstein. Quantentheorie des einatomigen idealen Gases. Zweite Abhandlung. *Sitzungsberichte der Preussischen Akademie der Wissenschaften*, **1**:3, 1925.

[3] N. S. Bose. Plancks Gesetz und Lichtquantenhypothese. *Z. Phys.*, **26**:178, 1924.

[4] M.Anderson, J. Ensher, M. Matthews, C. Wiemann, und E. Cornell. Observation of Bose-Einstein condensation in a dilute atomic vapor. *Science*, **269**:198, 1995.

[5] K. Davis, M.-O. Mewes, M. Andrews, N. van Druten, D. Drufee, D. Kurn, und W. Ketterle. Bose-Einstein condensation in a gas of sodium atoms. *Phys. Rev. Lett.*, **75**:3969, 1995.

[6] The Royal Swedish Academy of Science. Nobel Prize in Physics for 2001. http://www.nobel.se/physics/laureates/2001/press.html, 2001.

[7] S. Dettmer, D. Hellweg, P. Ryytty, J. J. Arlt, W. Ertmer, K. Sengstock, D. S. Petrov, G. V. Schlyapnikov, H. Kreuzmann, L. Santos, und M. Lewenstein. Observation of phase fluctuations in elongated Bose-Einstein condensates. *Phys. Rev. Lett.*, **87**:160406, October 2001.

[8] M.-O. Mewes, A. Andrews, N. van Druten, D. Kurn, D. Durfee, C. Townsend, und W. Ketterle. Collective excitations of a Bose-Einstein condensate in a magnetic trap. *Phys. Rev. Lett.*, **77**:988, 1996.

[9] M.-O. Mewes, M. R. Andrews, D. M. Kurn, D. S. Durfee, C. G. Townsend, und W. Ketterle. Output coupler for Bose-Einstein condensed atoms. *Phys. Rev. Lett.*, **78**:582, October 1997.

[10] B. P. Anderson und M. A. Kasewich. Macroscopic quantum interference from atomic tunnel arrays. *Science*, **282**:1686, November 1998.

[11] S. Inouye, T. Pfau, A. P. Chikkatur, A. Görlitz, D. E. Pritchard, und W. Ketterle. Phase-coherent amplification of atomic matter waves. *Nature*, **402**:641, December 1999.

[12] M. Greiner, O. Mandel, T. Esslinger, T. W. Hänsch, und I. Bloch. Quantum phase transition from a superfluid to a Mott insulator in a gas of ultracold atoms. *Nature*, **415**:39, January 2002.

[13] P. Bouyer und M. A. Kasevich. Heisenberg-limited spectroscopy with degenerate Bose-Einstein gases. *Phys. Rev. A*, **56**:1083, 1997.

[14] D. DeMille. Quantum computation with trapped polar molecules. *Phys. Rev. Lett.*, **88**:067901, 2002.

[15] S. Inouye, M. Andrews, J. Stenger, H.-J. Miesner, D. Stamper-Kurn, und W. Ketterle. Observation of Feshbach-resonances in a Bose-Einstein condensate. *Nature*, **392**:151, 1998.

[16] A. Marte, T. Volz, J. Schuster, S. Dürr, G. Rempe, E. G. M. van Kempen, und B. J. Verhaar. Feshbach-resonances in Rubidium 87: precision measurement and analysis. *Phys. Rev. Lett.*, **89**:283202, 2002.

[17] M. Greiner, C. A. Regal, und D. S. Jin. Emergence of a molecular Bose-Einstein condensate from a Fermi sea. *Nature*, **426**:537, 2003.

[18] D. O'Dell, S. Giovanazzi, G. Kurizki, und V.M. Akulin. Bose-Einstein condensates with 1/r interatomic attraction: electromagnetically induced "gravity". *Phys. Rev. Lett.*, **84**:5687, June 2000.

[19] S. Giovanazzi, G. Kurizki, I. E. Mazets, und S. Stringari. Collective excitations of a "gravitationally" self-bound Bose gas. *Europhys. Lett.*, **56**, October 2001.

[20] S. Giovanazzi, D. O'Dell, und G. Kurizki. One-dimensional compression of Bose-Einstein condenstaes by laser-induced dipole-dipole interactions. *J. Phys. B*, **34**:4757, August 2001.

[21] S. Giovanazzi, D. O'Dell, und G. Kurizki. Self-binding transition in Bose condensates with laser-induced ´´gravitation". *Phys. Rev. A*, **63**:031603, 2001.

[22] M. Kalinski, I. E. Mazets, G. Kurizki, B. A. Malomed, K. Vogel, und W. P. Schleich. Dynamics of laser-induced supersolid formation in Bose-Einstein condensates. *arXiv:cond-mat*, 0310480, October 2003.

[23] I. E. Mazets, D. H. J. O'Dell, G. Kurizki, N. Davidson, und W. P. Schleich. Depletion of Bose-Einstein condensates by laser-induced dipole-dipole interactions. *arXiv:cond-mat*, 0310672, October 2003.

[24] L. Santos, G. Shlyapnikov, P. Zoller, und M. Lewenstein. Bose-Einstein condensation in trapped dipolar gases. *Phys. Rev. Lett.*, **85**:1719, 2000.

[25] K. Góral, K. Rzazewski, und T. Pfau. Bose-Einstein condensation with magnetic dipole-dipole forces. *Phys. Rev. A*, **61**:051601, 2000.

[26] K. Góral und L. Santos. Ground state and elementary excitations of single and binary Bose-Einstein condensates of trapped dipolar gases. *Phys. Rev. A*, **66**:023613, 2002.

[27] S. Hensler, J. Werner, A. Griesmaier, P. O. Shmidt, A. Görlitz, und T. Pfau. Dipolar relaxations in an ultra-cold gas of magnetically trapped Chromium atoms. *App. Phys. B*, **77**:765, 2003.

[28] M. M. Burns, J. M. Fournier, und J. A. Golovchenko. Optical binding. *Phys. Rev. Lett.*, **63**:1233, September 1989.

[29] J. Leonard, M. Walhout, A. P. Mosk, T. Mueller, M. Leduc, und C. Cohen-Tannoudji. Giant helium dimers produced by photoassociation of ultracold metastable atoms. *Phys. Rev. Lett.*, **91**:073203, 2003.

[30] C. Cohen-Tannoudji, J. Dupont-Roc, und G. Grynberg. Atom-photon interactions. John Wiley & Sons, 1992.

[31] M.O. Scully und M. Suhail Zubairy. Quantum optics. Cambridge University Press, 2002.

[32] D.P. Craig und T. Thirunamachandran. Molecular quantum electrodynamics. Dover Publications, Inc., 1998.

[33] H.J. Charmichael. Statistical methods in quantum optics, vol. 1. Springer, New York, 1999.

[34] H. J. Metcalf und P. van der Straten. Laser cooling and trapping. Springer, New York, 1999.

[35] F. Dalfovo, S. Giorgini, L. P. Pitaevskii, und S. Stringari. Theory of Bose-Einstein condensations in trapped gases. *Rev. Mod. Phys.*, **71**:463, April 1999.

[36] Kerson Huang. Statistical mechanics. John Wiley & Sons, 1987.

[37] F. Schwabl. Statistische Mechanik. Springer, New York, 2000.

[38] Y. Castin. Bose-Einstein condensates in atomic gases: simple theoretical results. Springer, New York, 2001.

[39] J. Dalibard und C. Cohen-Tannoudji. Dressed-atom approach to atomic motion in laser light: the dipole force revisited. *J. Opt. Soz. Am. B*, **2**:1707, November 1985.

[40] P. S. Jessen und I. H. Deutsch. Optical lattices. *Adv. At. Mol. Opt. Phys*, **37**:95, 1996.

[41] I. H. Deutsch und P. S. Jessen. Quantum-state control in optical lattices. *Phys. Rev. A*, **57**:1972, 1998.

[42] P. B. Blackie und R. J. Ballagh. Mean-field treatment of Bragg scattering from a Bose-Einstein condensate. *J. Phys. B: At. Mol. Opt. Phys*, **33**:3961, 2000.

[43] Jürgen Schoser. Erzeugung eines Bose-Einstein-Kondensates in einer strak anisotropen Magnetfalle. PHD thesis, Universität Stuttgart, 2003.

[44] D. R. Lide. CRC handbook of chemistry and physics. CRCnetBase, 1999.

[45] Korea Atomic Energy Research Institute. Table of the Nuclids. http://sutekh.nd.rl.ac.uk/CoN/, 2003.

[46] D. A. Steck. Rubidium 87 D line data. http://steck.us/alkalidata, 2002.

[47] A. A. Radzig und B. M. Smirnov. Reference data on atoms, molecules and ions. Springer Verlag, Berlin, 1985.

[48] Rolf Heidemann. Verdampfungskühlung und Bose-Einstein-Kondensation von Rubidiumatomen. Diploma thesis, Universität Stuttgart, 2002.

[49] Jochen Steinamnn. Erzeugung eines entarteten Quantengases aus ^{87}Rb-Atomen. Diploma thesis, Universität Stuttgart, 2003.

[50] J. Schoser, A.Batär, R.Löw, V. Schweikhard, A. Grabovski, Yu. B. Ovchinnikov, und T. Pfau. Intense source of cold Rb atoms from a pure two-dimensional magneto-optical trap. *Phys. Rev. A*, **66**, 2002.

[51] Volker Schweikhard. Ultracold atoms in a far detuned optical lattice. Diploma thesis, Universität Stuttgart, 2001.

[52] Y. Castin und R. Dum. Bose-Einstein condensates in time dependent traps. *Phys. Rev. Lett.*, **77**:5315, December 1996.

[53] C. Keller, J. Schmiedmayer, A. Zeilinger, T. Nonn, S. Dürr, und G. Rempe. Adiabatic following in standing wave diffraction of atoms. *App. Phys. B*, **69**:303, 1999.

[54] T. Petelski, F. Fattori, G. Lamporesi, J. Stuhler, und G. M. Tino. Doppler-free spectroscopy using magnetically induced dichroism of atomic vapor: a new scheme for laser frequency locking. *Eur. Phys. J. D*, **22**:279, 2003.

[55] H. M. J. M. Boesten, C. Tsai, J. Gardener, D. Heinzen, und B. Verhaar. Observation of a shape resonance in the collision of two cold ^{87}Rb atoms. *Phys. Rev. A*, **55**:636, 1997.

[56] S. M. Tan und D. F. Walls. Loss of coherence in interferometry. *Phys. Rev. A*, **47**:4663, June 1993.

[57] Tilman Pfau. Beugung eines metastabilen Heliumstrahls an laserinduzierten Phasengittern. PHD thesis, Universität Konstanz, 1994.

[58] R. H. Picard und C. R. Willis. Coupled Superradiance Master Equations. *Phys. Rev. A*, **8**:1536, September 1973.

[59] D. Polder, M. F. H. Schuurmans, und Q. H. F. Vrehen. Superfluorescence: Quantum-mechanical derivation of the Maxwell-Bloch description with fluctuating field source. *Phys. Rev. A*, **19**:1192, March 1979.

[60] L. Sczaniecki. Effective Hamiltonians, two-level systems, and generalized Maxwell-Bloch equations. *Phys. Rev. A*, **28**:3493, December 1983.

[61] D. Jaksch, C. Bruder, J. I. Cirac, C. W. Gardiner, und P. Zoller. Cold Bosonic atoms in optical lattices. *Phys. Rev. Lett.*, **81**:3108, January 1998.

[62] M. G. Moore und P. Meystre. Self-binding transition in Bose condensates with laser-induced ´´gravitation". *Phys. Rev. Lett.*, **83**:5202, 1999.

[63] D. Schneble, Y. Torii, M. Boyd, E. W. Streed, D. E. Pritchard, und W. Ketterle. Superradiance in the short-pulse regim. *Science*, **300**:475, 2003.

[64] M. D. Lukin, M. Fleischhauer, R. Cote, L. K. Duan, D. Jaksch, J. I. Cirac, und P. Zoller. Dipole blockade and quantum information processing in mesoscopic atomic ensembles. *Phys. Rev. Lett.*, **87**, July 2001.

[65] T. Opatrny, B. Deb, und G. Kurizki. Proposal for translational entanglement of dipole-dipole interacting atoms in optical lattices. *Phys. Rev. Lett.*, **90**:250404, 2003.

[66] W. Zhang, H. Pu, C. Search, und P. Meystre. Spin waves in a Bose-Einstein condensed atomic spin chain. *Phys. Rev. Lett.*, **88**, February 2002.

Acknowledgements

Here I want to thank all the people who contributed their part to this thesis. I would like to thank especially

- Prof. Tilman Pfau for giving me the opportunity to work at his chair in this exciting new field, for being always open for fascinating and enriching discussions and for his support.
- Prof. Axel Görlitz for his supervision and many helpful discussions.
- Jürgen Stuhler for his patience, his time and his energy. With his advices and suggestions he helped very much at the preparation and the writing of this manuscript.
- Prof. Maciej Lewenstein for his help and enriching discussions.
- Luis Santos for his support, advice and very interesting discussions.
- Prof. Günter Mahler for making the joint report.
- Robert Löw, for working with me on the experiment, sharing his knowledge and reading the manuscript.
- Rolf Heidemann, Axel Grabowski and Nils Nemitz for reading the manuscript and giving helpful suggestions.
- all other group members for their help and advice.
- my parents and friends who have been always there for me.